IODP
INTERNATIONAL OCEAN
DISCOVERY PROGRAM

Site U1507[1]

Check for updates

R. Sutherland, G.R. Dickens, P. Blum, C. Agnini, L. Alegret, G. Asatryan,
J. Bhattacharya, A. Bordenave, L. Chang, J. Collot, M.J. Cramwinckel, E. Dallanave,
M.K. Drake, S.J.G. Etienne, M. Giorgioni, M. Gurnis, D.T. Harper, H.-H.M. Huang,
A.L. Keller, A.R. Lam, H. Li, H. Matsui, H.E.G. Morgans, C. Newsam, Y.-H. Park,
K.M. Pascher, S.F. Pekar, D.E. Penman, S. Saito, W.R. Stratford, T. Westerhold, and
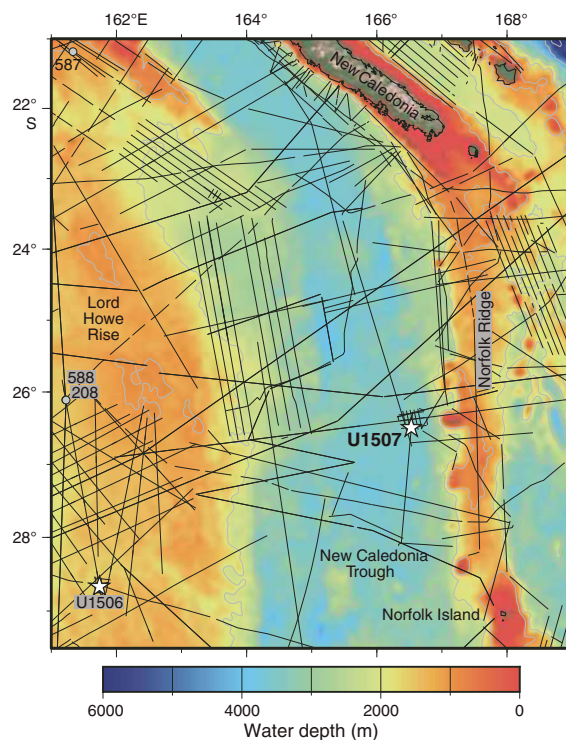X. Zhou[2]

Contents

Background and objectives

International Ocean Discovery Program (IODP) Site U1507 (26°29.316′S, 166°31.716′E; 3568 m water depth) is located on the eastern side of New Caledonia Trough, adjacent to Norfolk Ridge. It is distal from previous scientific drilling sites: ~460 km south of New Caledonia, ~620 km north of Deep Sea Drilling Project (DSDP) Site 206, and ~530 km east of DSDP Sites 208 and 588 (Figure F1). The site was chosen to determine the timing of deformation and uplift of Norfolk Ridge, to constrain the age of trough formation and sediment fill, and to obtain a record of subduction-related volcanism.

Sediment in New Caledonia Trough was drilled in 1971 at Site 206, where deformed Paleocene and Eocene calcareous ooze and chalk lies beneath middle Oligocene to recent ooze that is clay rich in places (Shipboard Scientific Party, 1973). Basement rock was not sampled at Site 206. In Taranaki Basin, which is at the southern end of New Caledonia Trough and ~1500 km from Site U1507, Cretaceous rifted basin fill is overlain by a transgressive shelf and coastal plain sedimentary sequence that has been imaged by seismic reflection data and drilled by petroleum wells (King and Thrasher, 1996).

The existence of sediments as old as the Cretaceous in the basal strata of southern New Caledonia Trough has led most previous authors to suggest that the trough formed as a Cretaceous rift basin that subsequently underwent postrift subsidence (Burns and Andrews, 1973; Collot et al., 2009; Crook and Belbin, 1978; Eade, 1988; King and Thrasher, 1996; Lafoy et al., 2005; Uruski and Wood, 1991; Uruski et al., 2003; Wood, 1993). However, seismic reflection inter-

Figure F1. Regional bathymetry and seismic reflection lines near Site U1507. Stars = Expedition 371 sites, dots = DSDP sites.

pretations of a drowned shelf near Taranaki imply major tectonic subsidence (>2 km) of southern New Caledonia Trough since the Eocene (Baur et al., 2014; Sutherland et al., 2010). This subsidence, combined with structural and stratigraphic observations, has led to an alternate view that Eocene subduction zone initiation may have substantially modified water depth in New Caledonia Trough and been a primary cause of the first-order topography and basin structure observed today (Baur et al., 2014; Collot et al., 2008; Sutherland et al., 2010).

Site U1507 was chosen to fill a knowledge gap in the northern and central New Caledonia Trough. The northern end of the trough is 1700 km from Site 206, and most tectonic models infer that the northern and central segments of New Caledonia Trough (i.e., north of Site 206) were proximal to where Tonga-Kermadec subduction initiated (Herzer et al., 2011; Matthews et al., 2015; Mortimer et al., 2018; Schellart et al., 2006). Seismic reflection profiles reveal the sedimentary sequence to be relatively thin (suitable for drilling) in the central part of the trough and to contain at least three seismic units that can be related to the regional tectonic history.

Site U1507 is located on the basin floor adjacent to Norfolk Ridge (Figure F2). The seabed gently slopes toward the axis of the trough, and swath bathymetry images reveal subtle relief associated with basin floor fans that are derived from incised canyons on the lower part of the Norfolk Ridge slope. Norfolk Ridge has a series of volcanic cones of late Oligocene age lying just west of the ridge crest (Mortimer et al., 2018), and one of them is close to Site U1507.

A grid of seismic reflection lines was collected to locate the best site for drilling (Figure F2). The upper seismic unit comprises continuous or semicontinuous, moderate-amplitude reflections mixed with chaotic layers several kilometers across that are interpreted as debris flows (Figure F3; Reflectors A–C). The middle seismic unit comprises semicontinuous, high-amplitude reflections in its upper part (Reflectors D and E) and moderate-amplitude, discontinuous reflectors in its lower part that downlap onto the lower unit (Reflector F). The lower unit comprises continuous or semicontinuous, moderate-amplitude reflectors that are locally folded and show fanning relationships. Small faults and apparent volcanic intrusions cut through the lower unit (e.g., bottom left of Figure F3). The technical objective at Site U1507 was to sample all three units to sufficient depth to understand the Paleogene evolution of the New Caledonia Trough.

Operations

Hole locations, water depths, and the number of cores recovered are listed in Table T1. All times are local ship time (UTC + 10 h).

Hole U1507A

The 286 nmi transit from Site U1506 concluded with the arrival at Site U1507 at 2200 h on 6 August 2017. After lowering the thrusters and switching to dynamic positioning mode, the rig floor was cleared for operations, beginning Hole U1507A at 2225 h. The rig crew assembled an advanced piston corer (APC)/extended core barrel (XCB) bottom-hole assembly (BHA) by 0130 h on 7 August, picked up drill pipe and the top drive, and deployed the bit just above the seafloor. A wiper "pig" was pumped through the drill string to clean out potential debris. The nonmagnetic APC core barrels were dressed with core liners in preparation for spudding Hole U1507A at 1040 h.

Figure F2. Local site survey data near Site U1507.

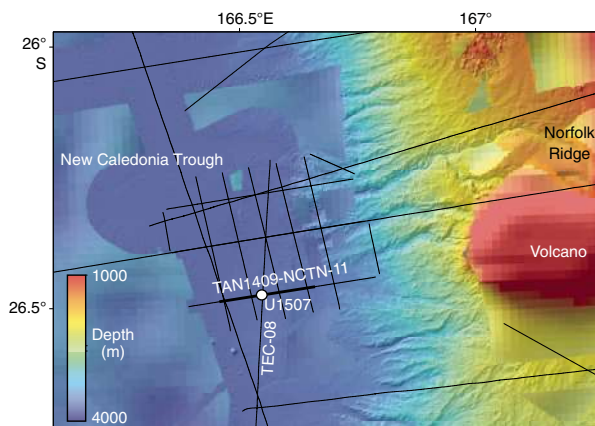Figure F3. Seismic Section TAN1409-NCTN-11 through Site U1507 and perpendicular to Norfolk Ridge. Reflectors A–H are correlated with cores and downhole data (see text). Reflectors A–C are mass transport complexes in a packet of reflectors that onlaps the basin margin. High-amplitude reflector at 5.82 s TWT below Site U1507 is interpreted as the base of sedimentary fill. CDP = common depth point, VE = vertical exaggeration.
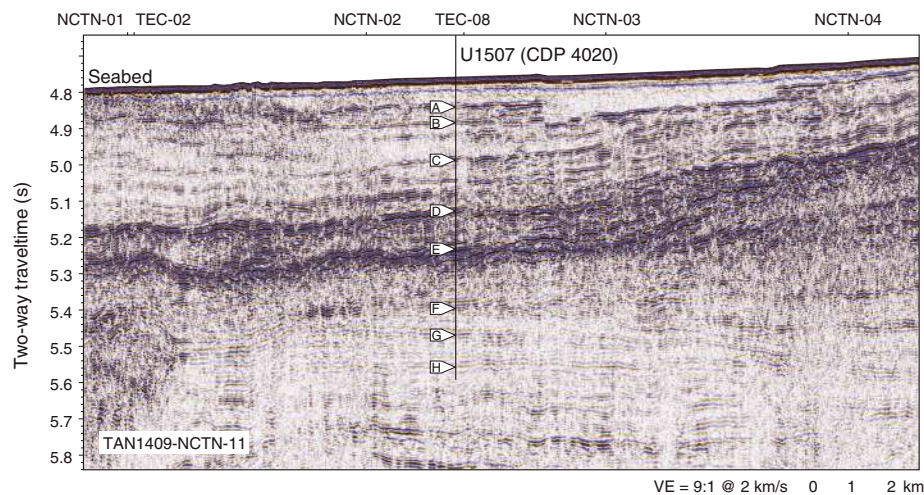
Table T1. Core summary, Site U1507. DRF = drilling depth below rig floor, DSF = drilling depth below seafloor, CSF-A = core depth below seafloor, Method A. Seafloor depth estimate methods: APC_CALC = drill string length from rig floor to the bit, plus the length of the extended advanced piston corer (APC) core barrel, minus the length of core recovered; OFFSET = seafloor depth is adopted from the previous hole. H = APC, X = extended core barrel (XCB), R = rotary core barrel (RCB), numeric core type = drilled interval. (Continued on next page.) **Download table in CSV format.**

Hole U1507A
Latitude: 26°29.3158′S
Longitude: 166°31.7039′E
Water depth (m): 3568
Date started (UTC): 1225 h; 6 August 2017
Date finished (UTC): 2340 h; 9 August 2017
Time on hole (days): 3.5
Seafloor depth DRF (m): 3579.3
Seafloor depth est. method: APC_CALC
Rig floor to sea level (m): 10.9
Penetration DSF (m): 425.4
Cored interval (m): 425.4
Recovered length (m): 352.7
Recovery (%): 83
Total cores (no.): 46
APC cores (no.): 26
XCB cores (no.): 20

Hole U1507B
Latitude: 26°29.3158′S
Longitude: 166°31.7155′E
Water depth (m): 3568
Date started (UTC): 2340 h; 9 August 2017
Date finished (UTC): 0150 h; 18 August 2017
Time on hole (days): 8.1
Seafloor depth DRF (m): 3579.3
Seafloor depth est. method: OFFSET
Rig floor to sea level (m): 11.0
Penetration DSF (m): 864.4
Cored interval (m): 488.4
Recovered length (m): 371.53
Recovery (%): 76
Drilled interval (m): 376
Drilled interval (no.): 1
Total cores (no.): 52
RCB cores (no.): 52

Core	Top depth drilled DSF (m)	Bottom depth drilled DSF (m)	Interval advanced (m)	Recovered length (m)	Curated length (m)	Top depth cored CSF-A (m)	Bottom depth recovered CSF-A (m)	Core recovery (%)	Core on deck date (2017)	Core on deck time UTC (h)	Sections (N)
371-U1507A-											
1H	0.0	6.2	6.2	6.22	6.22	0.0	6.22	100	7 Aug	0120	6
2H	6.2	15.7	9.5	9.88	9.88	6.2	16.08	104	7 Aug	0235	8
3H	15.7	25.2	9.5	9.50	9.50	15.7	25.20	100	7 Aug	0340	8
4H	25.2	34.7	9.5	9.86	9.86	25.2	35.06	104	7 Aug	0500	8
5H	34.7	44.2	9.5	9.70	9.70	34.7	44.40	102	7 Aug	0600	8
6H	44.2	53.7	9.5	9.89	9.89	44.2	54.09	104	7 Aug	0705	8
7H	53.7	63.2	9.5	9.77	9.77	53.7	63.47	103	7 Aug	0840	8
8H	63.2	72.7	9.5	9.84	9.84	63.2	73.04	104	7 Aug	0945	8
9H	72.7	82.2	9.5	9.84	9.84	72.7	82.54	104	7 Aug	1050	8
10H	82.2	91.7	9.5	9.93	9.93	82.2	92.13	105	7 Aug	1210	8
11H	91.7	101.2	9.5	9.88	9.88	91.7	101.58	104	7 Aug	1315	8
12H	101.2	110.7	9.5	10.00	10.00	101.2	111.20	105	7 Aug	1410	8
13H	110.7	120.2	9.5	10.09	10.09	110.7	120.79	106	7 Aug	1535	8
14H	120.2	129.7	9.5	9.99	9.99	120.2	130.19	105	7 Aug	1655	8
15H	129.7	139.2	9.5	9.93	9.93	129.7	139.63	105	7 Aug	1810	8
16H	139.2	148.7	9.5	9.96	9.96	139.2	149.16	105	7 Aug	1935	8
17H	148.7	158.2	9.5	10.00	10.00	148.7	158.70	105	7 Aug	2045	8
18H	158.2	167.7	9.5	10.06	10.06	158.2	168.26	106	7 Aug	2150	8
19H	167.7	177.2	9.5	10.05	10.05	167.7	177.75	106	7 Aug	2325	8
20H	177.2	186.7	9.5	9.93	9.93	177.2	187.13	105	8 Aug	0035	8
21H	186.7	196.2	9.5	9.68	9.68	186.7	196.38	102	8 Aug	0155	8
22H	196.2	205.7	9.5	9.44	9.44	196.2	205.64	99	8 Aug	0255	8
23H	205.7	215.2	9.5	9.90	9.90	205.7	215.60	104	8 Aug	0350	8
24H	215.2	224.7	9.5	9.63	9.63	215.2	224.83	101	8 Aug	0450	8
25H	224.7	234.2	9.5	9.62	9.62	224.7	234.32	101	8 Aug	0550	8
26H	234.2	243.7	9.5	10.06	10.06	234.2	244.26	106	8 Aug	0735	8
27X	243.7	253.0	9.3	5.99	5.99	243.7	249.69	64	8 Aug	0910	5
28X	253.0	262.6	9.6	5.49	5.49	253.0	258.49	57	8 Aug	1020	5
29X	262.6	272.2	9.6	1.11	1.11	262.6	263.71	12	8 Aug	1130	2
30X	272.2	281.8	9.6	7.49	7.49	272.2	279.69	78	8 Aug	1250	6
31X	281.8	291.4	9.6	2.64	2.64	281.8	284.44	28	8 Aug	1400	3
32X	291.4	301.1	9.7	4.87	4.87	291.4	296.27	50	8 Aug	1530	5
33X	301.1	310.6	9.5	9.11	9.11	301.1	310.21	96	8 Aug	1640	7
34X	310.6	320.2	9.6	6.51	6.51	310.6	317.11	68	8 Aug	1820	6
35X	320.2	329.8	9.6	7.47	7.47	320.2	327.67	78	8 Aug	1935	6
36X	329.8	339.4	9.6	6.23	6.23	329.8	336.03	65	8 Aug	2100	5
37X	339.4	349.0	9.6	4.51	4.51	339.4	343.91	47	8 Aug	2235	4
38X	349.0	358.6	9.6	8.11	8.11	349.0	357.11	84	9 Aug	0000	7
39X	358.6	368.2	9.6	9.28	9.28	358.6	367.88	97	9 Aug	0125	7
40X	368.2	377.7	9.5	5.30	5.30	368.2	373.50	56	9 Aug	0245	5
41X	377.7	387.2	9.5	0.53	0.53	377.7	378.23	6	9 Aug	0410	2
42X	387.2	396.8	9.6	2.87	2.87	387.2	390.07	30	9 Aug	0615	3
43X	396.8	401.8	5.0	0.47	0.47	396.8	397.27	9	9 Aug	0755	1
44X	401.8	406.3	4.5	1.15	1.15	401.8	402.95	26	9 Aug	0945	2
45X	406.3	415.9	9.6	6.16	6.16	406.3	412.46	64	9 Aug	1205	5

Table T1 (continued).

Core	Top depth drilled DSF (m)	Bottom depth drilled DSF (m)	Interval advanced (m)	Recovered length (m)	Curated length (m)	Top depth cored CSF-A (m)	Bottom depth recovered CSF-A (m)	Core recovery (%)	Core on deck date (2017)	Core on deck time UTC (h)	Sections (N)
46X	415.9	425.4	9.5	4.76	4.76	415.9	420.66	50	9 Aug	1430	4
	Hole U1507A totals:		425.4	352.70	352.70						296
371-U1507B-											
11	0.0	376.0			*****Drilled from 0.0 to 376.0 m DSF*****				10 Aug	2130	0
2R	376.0	385.5	9.5	4.65	4.65	376.0	380.65	49	10 Aug	2340	5
3R	385.5	395.1	9.6	6.75	6.75	385.5	392.25	70	11 Aug	0145	6
4R	395.1	404.6	9.5	9.67	9.67	395.1	404.77	102	11 Aug	0350	8
5R	404.6	414.2	9.6	9.18	9.18	404.6	413.78	96	11 Aug	0545	8
6R	414.2	423.7	9.5	10.02	10.02	414.2	424.22	105	11 Aug	0800	8
7R	423.7	433.3	9.6	8.92	8.92	423.7	432.62	93	11 Aug	1015	8
8R	433.3	442.9	9.6	9.27	9.27	433.3	442.57	97	11 Aug	1205	8
9R	442.9	452.5	9.6	7.07	7.07	442.9	449.97	74	11 Aug	1405	6
10R	452.5	462.1	9.6	4.78	4.78	452.5	457.28	50	11 Aug	1605	5
11R	462.1	471.7	9.6	4.65	4.65	462.1	466.75	48	11 Aug	1755	5
12R	471.7	481.3	9.6	8.43	8.43	471.7	480.13	88	11 Aug	2010	7
13R	481.3	490.8	9.5	7.74	7.74	481.3	489.04	81	11 Aug	2205	7
14R	490.8	500.4	9.6	8.20	8.20	490.8	499.00	85	12 Aug	0020	7
15R	500.4	510.0	9.6	9.07	9.07	500.4	509.47	94	12 Aug	0230	8
16R	510.0	519.6	9.6	10.04	10.04	510.0	520.04	105	12 Aug	0500	8
17R	519.6	529.2	9.6	3.56	3.56	519.6	523.16	37	12 Aug	0750	4
18R	529.2	538.8	9.6	0.97	0.97	529.2	530.17	10	12 Aug	1030	2
19R	538.8	548.4	9.6	4.67	4.67	538.8	543.47	49	12 Aug	1320	4
20R	548.4	558.0	9.6	6.73	6.73	548.4	555.13	70	12 Aug	1545	6
21R	558.0	567.5	9.5	10.15	10.15	558.0	568.15	107	12 Aug	1815	9
22R	567.5	577.0	9.5	0.11	0.11	567.5	567.61	1	12 Aug	2040	1
23R	577.0	586.6	9.6	5.46	5.36	577.0	582.36	57	13 Aug	0125	5
24R	586.6	596.1	9.5	9.74	9.74	586.6	596.34	103	13 Aug	0335	8
25R	596.1	605.7	9.6	10.06	10.06	596.1	606.16	105	13 Aug	0535	9
26R	605.7	615.3	9.6	4.56	4.56	605.7	610.26	48	13 Aug	0730	5
27R	615.3	624.9	9.6	0.85	0.85	615.3	616.15	9	13 Aug	0945	2
28R	624.9	634.5	9.6	0.64	0.64	624.9	625.54	7	13 Aug	1215	2
29R	634.5	639.2	4.7	4.55	4.55	634.5	639.05	97	13 Aug	1715	5
30R	639.2	644.2	5.0	3.23	3.23	639.2	642.43	65	13 Aug	1950	4
31R	644.2	653.8	9.6	10.02	10.02	644.2	654.22	104	13 Aug	2235	9
32R	653.8	663.3	9.5	8.58	8.58	653.8	662.38	90	14 Aug	0050	8
33R	663.3	672.9	9.6	9.28	9.28	663.3	672.58	97	14 Aug	0325	8
34R	672.9	682.4	9.5	9.99	9.99	672.9	682.89	105	14 Aug	0645	8
35R	682.4	692.0	9.6	7.08	7.08	682.4	689.48	74	14 Aug	0955	7
36R	692.0	701.5	9.5	8.63	8.63	692.0	700.63	91	14 Aug	1245	8
37R	701.5	711.1	9.6	9.59	9.59	701.5	711.09	100	14 Aug	1605	8
38R	711.1	720.7	9.6	9.45	9.45	711.1	720.55	98	14 Aug	2010	8
39R	720.7	730.3	9.6	8.67	8.67	720.7	729.37	90	15 Aug	0000	7
40R	730.3	739.8	9.5	8.78	8.78	730.3	739.08	92	15 Aug	0310	8
41R	739.8	749.4	9.6	10.26	10.26	739.8	750.06	107	15 Aug	0710	9
42R	749.4	759.0	9.6	7.87	7.87	749.4	757.27	82	15 Aug	1120	7
43R	759.0	768.6	9.6	3.69	3.69	759.0	762.69	38	15 Aug	1435	4
44R	768.6	778.2	9.6	9.11	9.11	768.6	777.71	95	15 Aug	1815	8
45R	778.2	787.8	9.6	10.04	10.04	778.2	788.24	105	15 Aug	2155	8
46R	787.8	797.4	9.6	7.99	7.99	787.8	795.79	83	16 Aug	0125	7
47R	797.4	807.0	9.6	8.45	8.45	797.4	805.85	88	16 Aug	0435	7
48R	807.0	816.5	9.5	10.33	10.33	807.0	817.33	109	16 Aug	0730	10
49R	816.5	826.1	9.6	9.14	9.14	816.5	825.64	95	16 Aug	1035	8
50R	826.1	835.7	9.6	9.51	9.51	826.1	835.61	99	16 Aug	1315	8
51R	835.7	845.3	9.6	0.38	0.38	835.7	836.08	4	16 Aug	1640	1
52R	845.3	854.8	9.5	10.03	10.03	845.3	855.33	106	16 Aug	2020	8
53R	854.8	864.4	9.6	0.94	0.94	854.8	855.74	10	17 Aug	0000	2
	Hole U1507B totals:		864.4	371.53	371.43						336
	Site U1507 totals:		1289.8	724.23	724.13						632

The mudline core recovered 6.2 m, establishing a water depth of 3568 m. APC coring continued to Core 26H. Given the increasing force required to retrieve the last few APC cores and the over-drilling required on Core 26H, we switched to XCB coring at 1815 h on 8 August. Given the depth objectives for Site U1507 (>700 m drilling depth below seafloor [DSF]), we decided against using the more time consuming half-length APC coring system. Recovery of Cores 1H through 26H ranged from 99% to 106% and averaged 104% (total of 243.7 m DSF cored and 252.7 m recovered). Temperature measurements were taken with Cores 4H, 7H, 10H, 13H, 16H, and 19H. The deployment of orientation and temperature tools was discontinued after Core 20H.

Coring continued in Hole U1507A with the XCB system. Toward the end of 9 August (at ~425 m DSF), it took ~100–150 min to cut a core. Moreover, the quality of the cores was poor, with prominent biscuiting, slurry, and abundant fracturing. At 0000 h, we decided to terminate Hole U1507A, pull the drill string, and start a rotary core barrel (RCB) hole at the depth where XCB coring became particularly difficult (~375 m DSF). Recovery for the XCB cores varied from 6% to 97% and averaged 55% (total of 181.7 m DSF cored and 100.1 m recovered). The drill string was retrieved from Hole U1507A and cleared the rig floor at 0940 h on 10 August, ending Hole U1507A. The time spent on Hole U1507A was 83.25 h or 3.5 days.

Hole U1507B

The ship was offset 20 m east of Hole U1507A. An RCB BHA was made up with a center bit installed in the core barrel that would allow us to drill without coring for the first 375 m DSF. We included a mechanical bit release (MBR) that would allow us to drop the bit at the bottom of the hole and then wireline log without retrieving the entire drill string. Drill pipe was deployed, and by 1800 h on 10 August 2017 the bit was just above the seafloor. After picking up the top drive, we pulled the core barrel with center bit and pumped a wiper pig through the drill string to clean out debris observed during drill string assembly. The core barrel with center bit was then dropped back in place, and drilling in Hole U1507B commenced at 2045 h on 10 August. Drilling without coring in Hole U1507B reached 376 m DSF by 0630 h on 11 August. The center bit was removed from the core barrel, and coring began at 0730 h and concluded at 1000 h on 17 August. Cores 2R through 53R penetrated from 376.0 to 864.4 m DSF with a total recovery of 371.5 m (76%). Recovery for RCB cores varied between 1% and 109%. Importantly, the quality of RCB cores was superior to those collected by XCB drilling over the 50 m DSF overlap interval. Mud sweeps were pumped for hole cleaning on every third core starting with Core 8R. At the end of coring, Hole U1507B was cleaned with a 25 bbl high-viscosity mud sweep in preparation for logging.

Wireline logging began with a wireline trip for the rotary shifting tool (RST) to activate the MBR and drop the coring bit at the bottom of the hole. The bit was released at 1130 h on 17 August. The RST was recovered, and a second wireline trip was conducted with the reverse RST to reposition the MBR sleeve into the circulating position. The tool was recovered and the sinker bars removed. From 1230 to 1315 h, the hole was displaced with 245 bbl of 11.0 lb/gal mud. The top drive was set back, the end of drill pipe was raised to 75.2 m wireline log depth below seafloor (WSF), and the rig floor was prepared for logging.

Assembly of the modified triple combo logging tool string began at 1700 h. The tool string included magnetic susceptibility, electrical resistivity, sonic, bulk density, and natural gamma radiation (NGR) tools. The neutron porosity tool, often run in the triple combo, and the microresistivity imaging (Formation MicroScanner) tool, often run in a separate string with the sonic tool, were omitted from the logging plan for this hole. The tools were assembled and tested at 1815 h, and the tool string was lowered into Hole U1507B.

The wireline active heave compensator was switched on once the tools reached open hole. A downhole log was performed from just above the seafloor to the bottom of the hole at ~864 m WSF. The hole was then logged uphole for a 124 m calibration pass, run back to the bottom, and logged uphole to just below the end of the pipe where the caliper was closed prior to entering the BHA. The

tools were pulled from the hole and were back at the surface at 0200 h on 18 August. By 0345 h, all logging equipment was rigged down, and the rig crew began retrieving the drill string.

Hole conditions were excellent for logging, with a hole diameter close to the bit diameter (~10 inches) all the way from the bottom of the hole (846.4 m WSF) to ~490 m WSF. Hole conditions were still good up to 234 m WSF, where a bridge with a hole diameter of only ~6 inches was encountered. Additional bridges were indicated in the caliper log farther uphole and just below the base of the drill string. The tool string passed these obstructions successfully and acquired high-quality measurements throughout the open hole. However, several hours of remediation work (washing) would have been required before the Versatile Seismic Imager (VSI) tool could have been run as planned, with limited chance of success, significant daylight time restrictions, and a poor weather forecast. Given the quality of the standard logs, particularly the sonic log, the primary logging scientific objective of tying cores to seismic reflection images had been substantially achieved, so we canceled the VSI run.

While the drill string was recovered, the seafloor positioning beacon was released and recovered. With bad weather expected during the transit to the next site, the drill collars were disassembled and secured in the drill collar rack. At 1130 h on 18 August, the end of the drill string cleared the rig floor. The rig floor was secured for transit at 1150 h, ending Hole U1507B and Site U1507. A total of 194 h or 8.1 days were spent on Hole U1507B.

While raising the thrusters, a hydraulic malfunction occurred and was repaired, and the transit to Site U1508 began at 1330 h on 18 August.

Lithostratigraphy

The sedimentary sequence at Site U1507 consists of ~686 m of Pleistocene to upper Eocene biogenic ooze and chalk with variable clay interbedded with ash layers and volcaniclastic turbidites (lithostratigraphic Unit I) overlying ~170 m of upper to middle Eocene homogeneous clayey nannofossil chalk (lithostratigraphic Unit II; Figure **F4**).

Unit I sediments are divided into three subunits based on differences in lithology and sedimentological features, as identified by macroscopic and microscopic (smear slide, thin section, and scanning electron microscope [SEM]) core description (Table **T2**). Subunit Ia consists predominantly of Pleistocene to lower Miocene nannofossil ooze and chalk in places interbedded with discrete foraminiferal ooze and limestone graded beds. Soft-sediment deformation (i.e., slumps) is widespread and most common in the lowermost part of the subunit. Subunit Ib is primarily composed of lower Miocene to upper Oligocene clayey nannofossil chalk with ash. Some intervals are interbedded with clayey tuffaceous sandstone or disrupted clayey foraminiferal chalk and limestone with volcanic clasts. In general, Subunit Ib differs from Subunit Ia by an overall increase in clay and volcanic content (Figure **F5**). Subunit Ic consists of lower Oligocene to upper Eocene coarse-grained tuffaceous conglomerate and sandstone alternating with clayey nannofossil chalk with ash. Volcaniclastic deposits display a range of sedimentary facies that point to deposition by various gravity flow processes, from debris flows to turbidity currents. It is noteworthy that a wide range of silica saturation in volcanic grains and clasts was observed, suggesting multiple source and complex petrogenesis.

Figure F4. Lithostratigraphic summary, Site U1507. Solid circles = Hole U1507A, open circles = Hole U1507B. cps = counts per second.
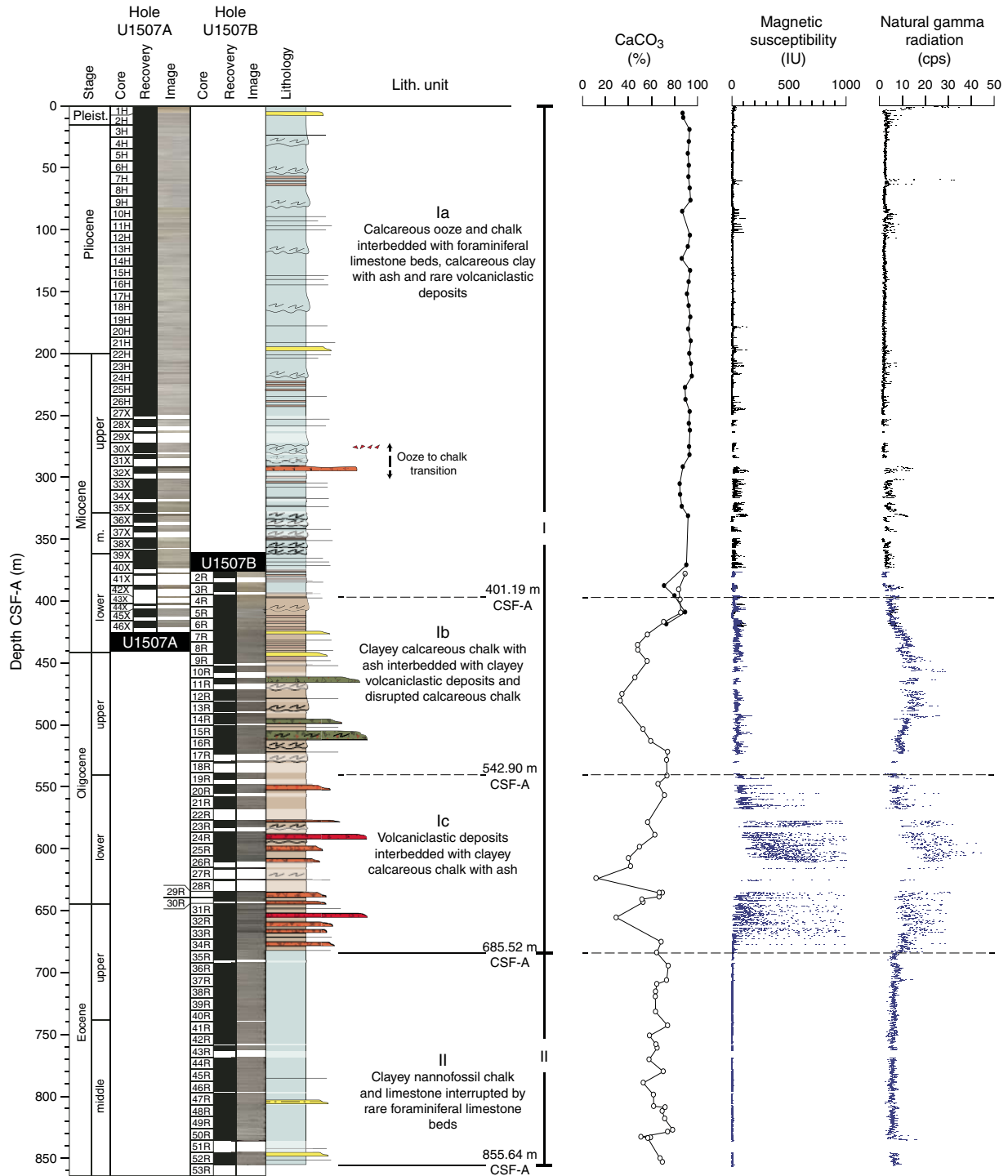
Lithostratigraphic Unit II comprises upper to middle Eocene clayey nannofossil chalk and clayey limestone. Between 835 and 845 m, the lithology changes to a greenish gray nannofossil claystone, probably reflecting decreased carbonate content across the Middle Eocene Climatic Optimum (MECO).

In Hole U1507A, the shift from APC to XCB coring resulted in significant core disturbance, typically substantial fracturing and biscuiting of the sediments. In Hole U1507B, rotary drilling led to common fracturing of sediments and poorer recovery, notably in intervals containing coarse-grained volcaniclastic lithologies.

Unit I

Unit I is a lithologically heterogeneous and sedimentologically complex Pleistocene–upper Eocene succession of biogenic ooze and chalk interbedded with nannofossil-rich clay with ash, foraminiferal ooze/chalk/limestone beds, and coarse-grained volcaniclastic de-

Table T2. Lithostratigraphic units of the sedimentary section, Site U1507. BOH = bottom of hole. **Download table in CSV format.**

Lith. unit	Depth CSF-A (m)	Thickness (m)	Interval	Lithology	Stage
Ia	0.00–401.19	401.19	371-U1507A-1H-1, 0 cm, to 43X-CC, 37 cm (BOH); 371-U1507B-2R-1, 0 cm, to 4R-5, 55 cm	Nannofossil ooze and chalk with varying amounts of clay interbedded with foraminiferal ooze, chalk and limestone, nannofossil-rich clay with ash, and rare volcaniclastic layers	Pleistocene to lower Miocene
Ib	401.19–542.90	141.71	371-U1507B-4R-5, 55 cm, to 19R-3, 110 cm	Clayey nannofossil chalk with varying amounts of foraminifers, volcanic ash, and clasts interbedded with foraminiferal limestone and tuffaceous conglomerate and sandstone	lower Miocene to upper Oligocene
Ic	542.90–685.52	142.62	371-U1507B-19R-3, 110 cm, to 35R-3, 60 cm	Volcaniclastic sandstone and conglomerate alternating with clayey calcareous chalk with ash and foraminiferal limestone	lower Oligocene to upper Eocene
II	685.52–855.64	170.12	371-U1507B-33R-3, 60 cm, to 53R-1, 74 cm (BOH)	Clayey nannofossil chalk and limestone interbedded with rare foraminiferal limestone	upper to middle Eocene

posits. The relative proportion, vertical distribution, and facies variability of these main lithologies are captured by three subunits, presented below (Subunits Ia–Ic; Figure **F4**). Despite the variable lithology and evidence for synsedimentary deformation, no significant hiatuses were documented in the succession (see **Biostratigraphy and paleoenvironment**).

Subunit Ia

Subunit Ia is ~401 m of Pleistocene to upper Miocene white to light gray (N8 to GLEY 1 8/10Y) bioturbated nannofossil ooze or chalk interbedded with common white gray (predominantly GLEY 1 8/N) foraminiferal ooze, chalk, or limestone (Figures **F5**, **F6**). The latter are typically very thin to medium-bedded, normally graded, sharp-based, planar- to ripple-laminated beds dominated by sand-sized planktic foraminifers. Microscopic examination from smear slides, thin sections, and SEM samples revealed common pyritization of individual foraminifers (Figure **F7**).

Soft-sediment deformation, expressed as overturned folds and tilted bedding, is widespread throughout the subunit. It typically affects biogenic ooze and chalk (Figure **F6**) and is common in the lowermost section of the subunit, between Cores 371-U1507A-36X and 371-U1507B-4R (~330–405 m).

Starting downhole from Core 371-U1507A-7H (~54 m), intervals of greenish gray (predominantly 10GY 6/1) clayey nannofossil ooze to nannofossil-rich clay with ash were encountered (Figure **F6**). Such intervals are usually sharp based and faintly laminated to massive, and they progressively grade into nannofossil ooze or chalk through a heavily bioturbated interval with *Chondrites, Planolites, Nereites*, or *Zoophycos* burrows. Microscopic examination from smear slides and thin sections identified silt-sized altered glass together with clay-sized green minerals (Figure **F7**). X-ray diffraction (XRD) examination of a thin green clay-rich layer in Core 10H (90.7 m) revealed a significant amount of serpentine, which was not observed in samples from Subunits Ib and Ic and Unit II (Figure **F8**).

A ~2 m thick interval with very dark greenish gray (GLEY 1 3/10Y) volcaniclastic deposits occurs in Core 371-U1507A-32X. Individual deposits consist of volcanic breccia and tuffaceous sandstone dominated by clasts of variably altered volcanic glass. The matrix is micritic and contains common planktic foraminifers. Subrounded to subangular nannofossil chalk rip-up clasts are also common.

The ooze–chalk transition is gradual and occurs across Cores 371-U1507A-30X through 32X (~272–296 m). The change from APC to XCB coring between Cores 26H and 27X resulted in poorer recovery and significant disturbance of sediment at the lower depths in Hole U1507A.

Subunit Ib

Subunit Ib is ~142 m of lower Miocene to upper Oligocene greenish gray (predominantly GLEY 1 7/5GY) clayey nannofossil chalk with ash interbedded with dark greenish gray (GLEY 1 4/10Y) clayey tuffaceous sandstone and greenish gray (GLEY 1 6/10GY) clayey foraminiferal chalk and limestone with volcanic clasts (Figure **F9**). The boundary with overlying Subunit Ia is marked by an overall increase in clayey and volcaniclastic lithologies (Figures **F5**, **F10**) with a clear color change from pale yellow to greenish gray in Cores 371-U1507B-2R through 4R. Clayey tuffaceous sandstone occurs as sharp-based, normally graded, thin to medium-bedded intervals with common planar to ripple laminations. The clayey foraminiferal chalk and limestone was typically encountered as thick- to very thick bedded, convoluted, internally disrupted beds with scattered volcanic clasts (e.g., Sections 16R-1 through 16R-3).

Subunit Ic

Subunit Ic is ~143 m of lower Oligocene to upper Eocene dark greenish gray (dominantly GLEY 1 4/10GY) tuffaceous conglomerate and sandstone along with very dark greenish gray (GLEY 1 3/N) tuff interbedded with light greenish gray (GLEY 1 7/10GY) clayey nannofossil chalk with ash (Figure **F11**). Lithologies are significantly coarser than those in the rest of lithostratigraphic Unit I and have higher magnetic susceptibility and NGR values (Figure **F4**). The boundary with Subunit Ib is defined by the first occurrence of a thick-bedded tuffaceous conglomerate in Core 371-U1507B-19R.

Bed thickness and grain size increase gradually upward in the lower part of the subunit and then decrease in the upper part, displaying an overall symmetrical trend (Figure **F11**). Volcaniclastic facies vary from very thick bedded, poorly sorted tuffaceous conglomerate to thinly bedded, typically planar- to ripple-laminated, medium- to fine-grained tuffaceous sandstone (Figure **F12**). Typically, beds are sharp based and normally graded but are abruptly overlain by bioturbated nannofossil clay with a clear grain size break. Thin sections and XRD measurements on tuffaceous intervals (Figures **F13**, **F8**) reveal isolated pyroxene, plagioclase, and possible amphibole alongside microcrystalline volcanic clasts with common plagioclase and pyroxene phenocrysts. Large benthic foraminifers and recrystallized bioclasts are also found in tuffaceous sandstone, typically floating in a fine-grained micritic matrix. Notably, quartz is absent from both the green clay and tuffaceous sandstone layers of Subunit Ic.

Unit II

Unit II is ~170 m of upper to middle Eocene homogeneous light greenish gray (dominantly GLEY 1 7/10GY) clayey nannofossil

Figure F5. Major biogenic and lithologic constituent abundances in sediment based on smear slide analysis, Site U1507. + symbols and darker colored lines = Hole U1507A, x symbols and lighter colored lines = Hole U1507B. D = dominant (>50%), A = abundant (25%–50%), C = common (10%–25%), R = rare (1%–10%), T = trace (>0%–1%). For intervals with closely spaced samples, relative abundances overlap due to scale of graphical representation.
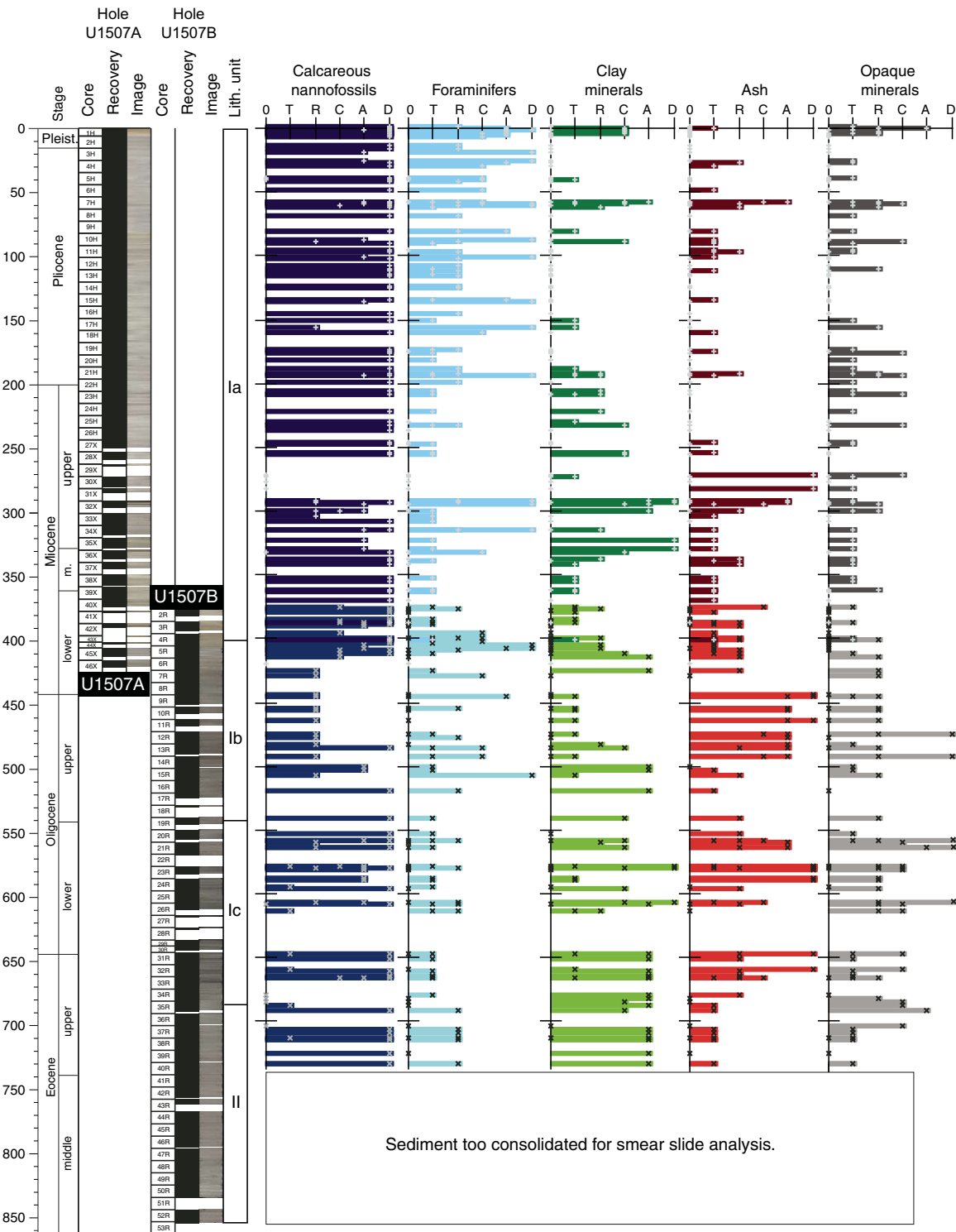
chalk with rare thin beds of planar-laminated, normally graded foraminiferal limestone (Figure F14). Thin section examination of the latter revealed recrystallized bioclasts and extraclasts and possibly volcanic plagioclase (Figure F15). Bioturbation is moderate throughout the unit, with prominent *Zoophycos*, *Nereites*, *Asterosoma*, and *Spirophyton* burrows. In detail, the clayey nannofossil

chalk displays subtle color banding on both the centimeter and multidecimeter scales, from light greenish gray to greenish gray (Figure F16), defining apparent cycles with a period of approximately 2 m. The boundary with Unit I is defined by the lowest occurrence of tuffaceous sandstone.

A change in color and lithology was observed in the lower sections of Core 371-U1507B-50R and in Core 51R, where a greenish gray (GLEY 1 5/5G) nannofossil claystone was encountered. This change in lithology potentially reflects increased carbonate dissolution related to the MECO (see **Biostratigraphy and paleo-** **environment**). Carbonate content is high across this interval (60%–80%; see **Geochemistry**), although wireline logging data are consistent with higher clay content in the sediment that we were not able to collect (see **Petrophysics**). Below this interval, the lithology is pervasively more lithified and classified as clayey limestone.

Figure F6. Common Subunit Ia sedimentary lithologies, Site U1507. A. Pliocene nannofossil ooze with foraminifers. B. Pliocene nannofossil ooze with foraminifers with slumped strata. C. Lower Miocene sharp-based, normally graded, planar-laminated foraminiferal limestone. Note the significant core biscuiting and fracturing due to XCB drilling. D. Upper Miocene nannofossil-rich clay with ash. The lowermost laminated interval with coarser grained ash underlies massive bioturbated clay.
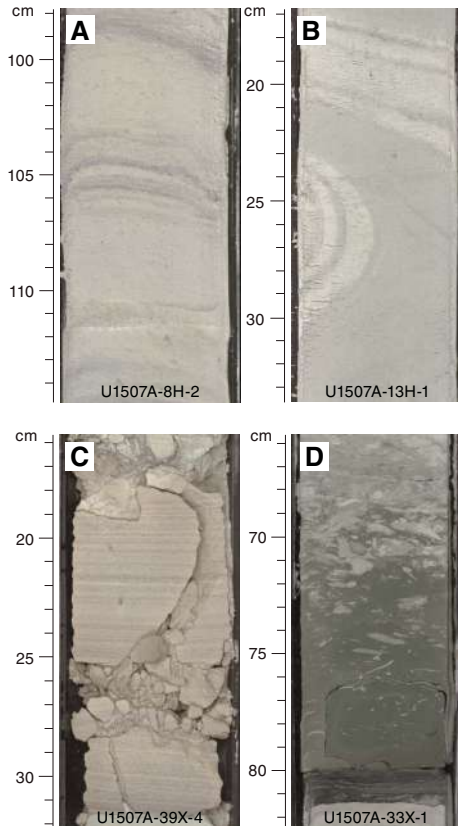
Figure F7. Common Subunit Ia sedimentary lithologies, Site U1507. A, B. Pliocene nannofossil ooze with foraminifers (frm). nanno = calcareous nannofossil. C, D. Pliocene nannofossil-rich clay with ash. Note the green clay minerals (authigenic glauconite? [glc]), Fe oxides (ox), and altered glass (gls). clay = clay minerals, bt = biotite. E. Upper Miocene foraminiferal limestone; lithology is dominated by planktic foraminifers in a micritic (mct) matrix. F. Planktic foraminifer with framboidal pyrite (py) crystals. PPL = plane-polarized light, XPL = cross-polarized light.
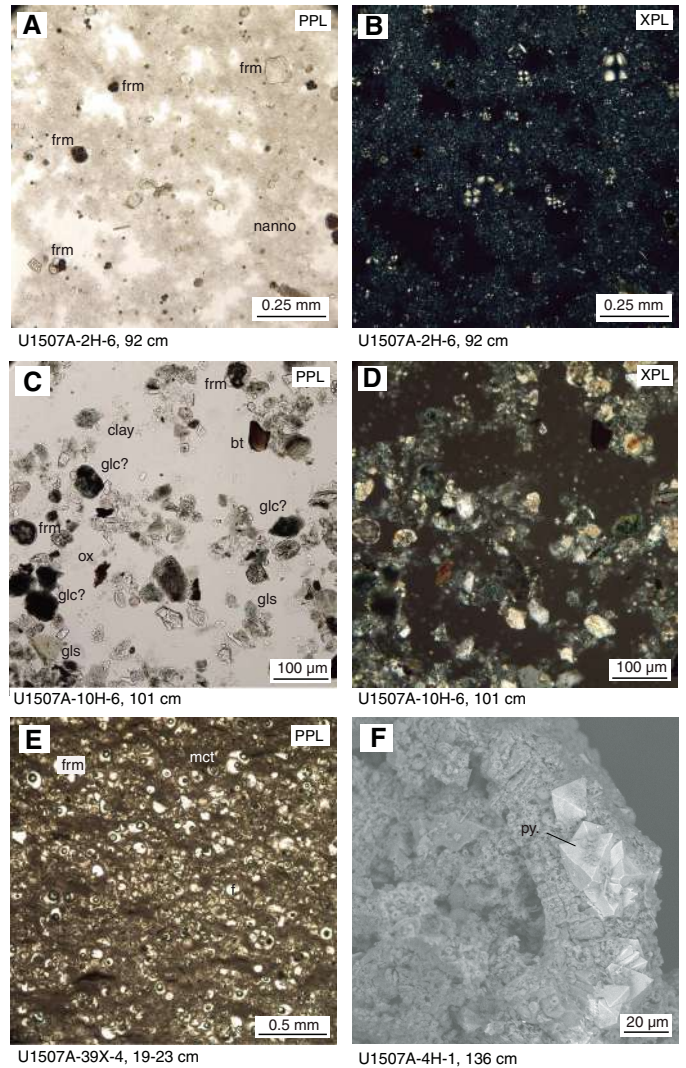
Figure F8. XRD diffractograms of selected powdered sediment samples, Site U1507. A. Four green nannofossil-rich clay intervals. Black = Subunit Ia, red = Subunit Ib, blue and green = Subunit Ic. B. Two tuffaceous sandstone layers, Subunit Ic.
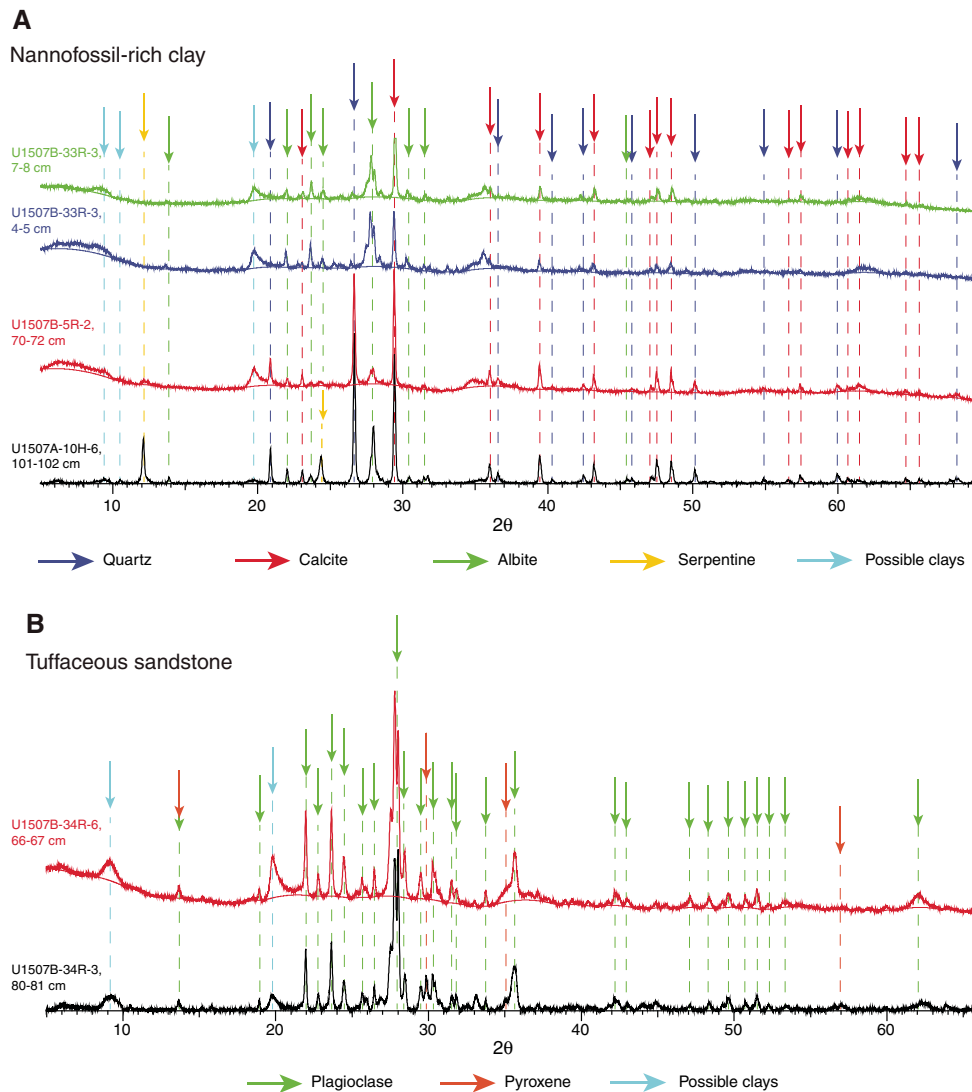
Figure F9. Common Subunit Ib sedimentary lithologies, Site U1507. A. Upper Oligocene disrupted clayey foraminiferal chalk with scattered volcanic clasts and rip-up clasts of foraminiferal chalk. This section is part of a very thick, strongly disrupted bed. B. Upper Oligocene clayey foraminiferal chalk with rare volcanic clasts displaying wispy planar laminations. C. Upper Oligocene sharp-based, normally graded clayey tuffaceous sandstone with rippled and convoluted laminations. D. Upper Oligocene sharp-based, normally graded, planar-laminated clayey tuffaceous siltstone.
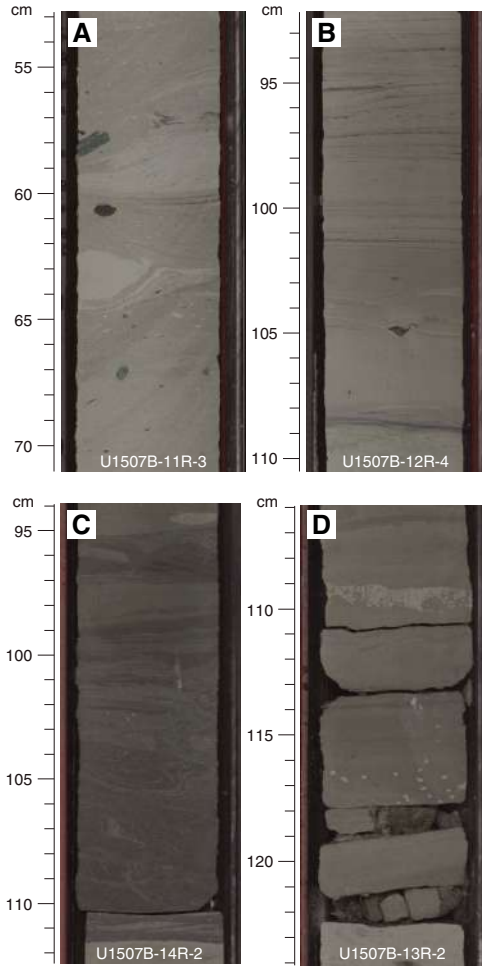
Figure F10. Common Subunit Ib sedimentary lithologies, Site U1507. A, B. Upper Oligocene clayey tuffaceous sandstone. Note the common glass (gls) fragments and rare quartz (qtz) grains. frm = foraminifer. C, D. Upper Oligocene clayey tuffaceous sandstone. Note the sponge spicule (sp) fragments. E. Lower Miocene disrupted clayey foraminiferal chalk. F. Upper Oligocene clayey foraminiferal chalk with silt-sized volcanic material.
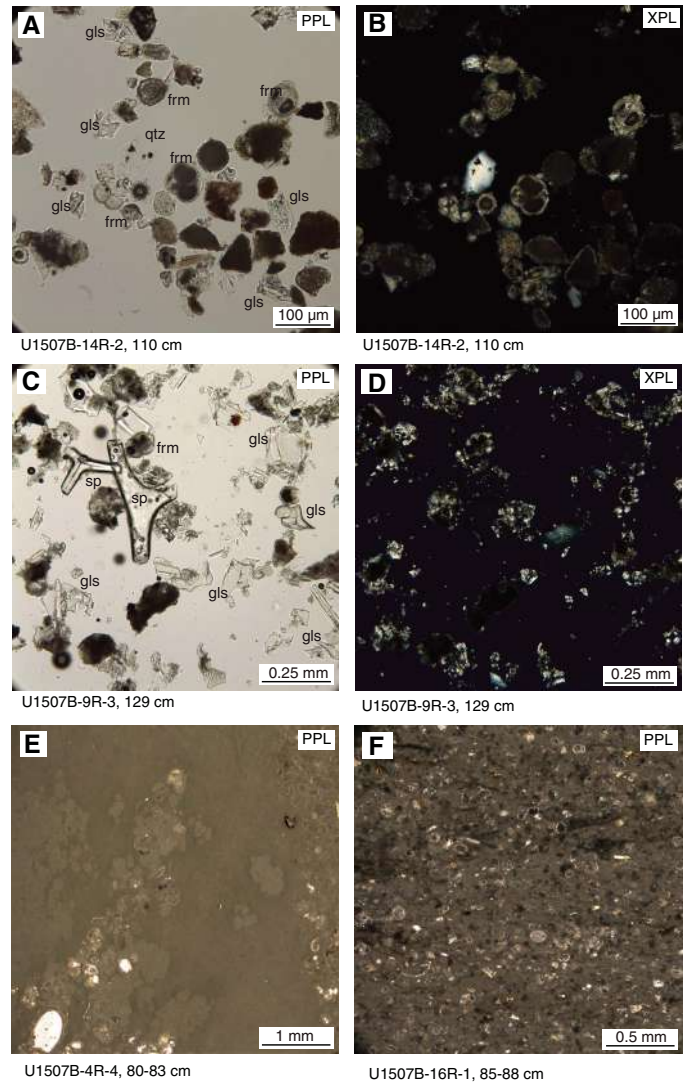
Figure F11. Distribution and thickness of calcareous turbidites (foraminiferal ooze/chalk/limestone) and volcaniclastic turbidites (volcanic breccia, tuffaceous sandstone, and tuff), Site U1507. Open symbols = beds interrupted by core gaps or whole-round samples (which thus represent minimum bed thickness), solid symbols = beds where both top and bottom were observed.
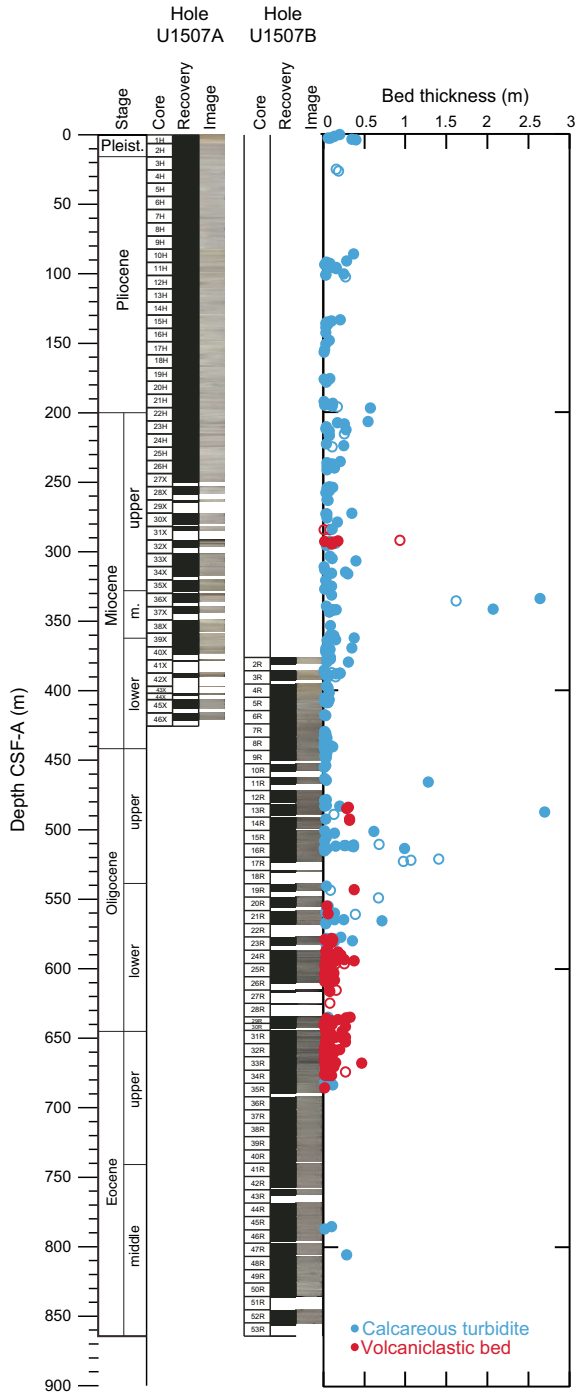

Figure F12. Common Subunit Ic sedimentary lithologies, Site U1507. A. Lower Oligocene tuffaceous conglomerate with vesicular basalt clasts and common nannofossil chalk rip-up clasts. B. Lower Oligocene massive to faintly planar-laminated tuffaceous sandstone. C. Lower Oligocene planar-laminated tuff sharply overlain by bioturbated clayey nannofossil chalk. D. Lower Oligocene planar- to ripple-laminated tuffaceous sandstone.
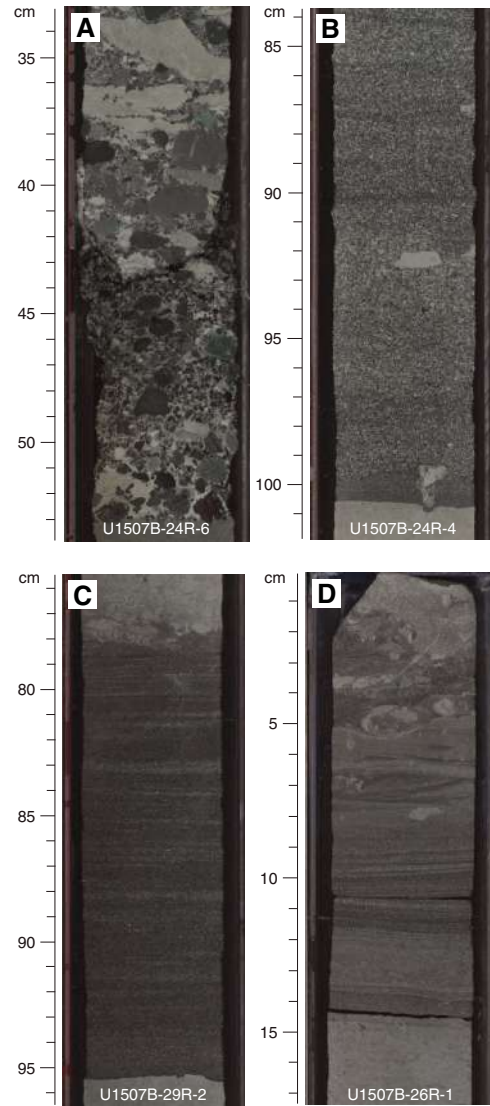
Figure F13. Common Subunit Ic sedimentary lithologies, Site U1507. A. Lower Oligocene clayey foraminiferal (frm) chalk with volcanic clasts. mct = micrite, prx = pyroxene, plag = plagioclase. B. Lower Oligocene tuffaceous sandstone. C, D. Upper Oligocene tuff. Note the isolated pyroxene grains, microcrystalline basalt clasts with plagioclase, and an altered (reddish brown) vesicular clast. ox = oxide. E. Lower Oligocene clayey foraminiferal chalk with volcanic clasts and a bioclast of possible shallow-water origin (gastropod?). F. Upper Oligocene tuff with a shallow-water coral or bryozoan.
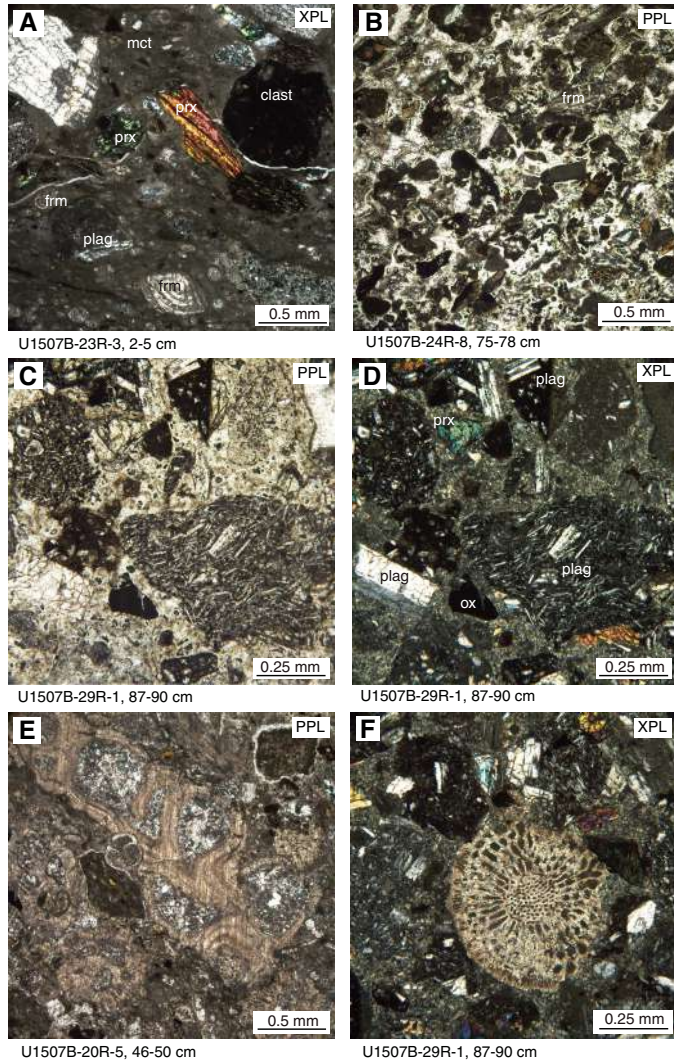

Figure F14. Common Unit II sedimentary lithologies, Site U1507. A. Upper Eocene bioturbated clayey nannofossil chalk with *Zoophycos* and *Planolites* burrows. Note the light green laminations and heavily bioturbated foraminiferal limestone between 42 and 43 cm. B. Middle Eocene green nannofossil clay with relatively low bioturbation. Stratigraphic datums suggest this represents the upper part of the MECO (see Biostratigraphy and paleoenvironment). C. Middle Eocene ripple- to planar-laminated foraminiferal limestone bed.
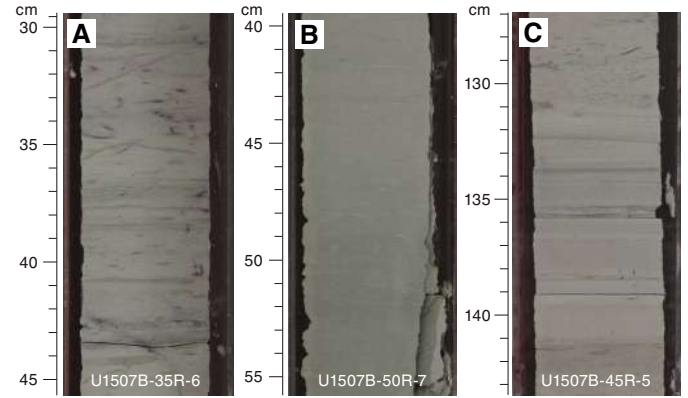

Figure F15. Common Unit II sedimentary lithologies, Site U1507. A. Middle Eocene nannofossil chalk with foraminifers (frm). mct = micrite. B. Middle Eocene foraminiferal limestone with recrystallized foraminifers.
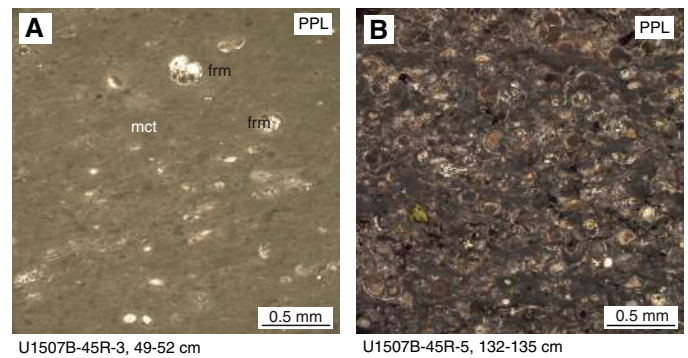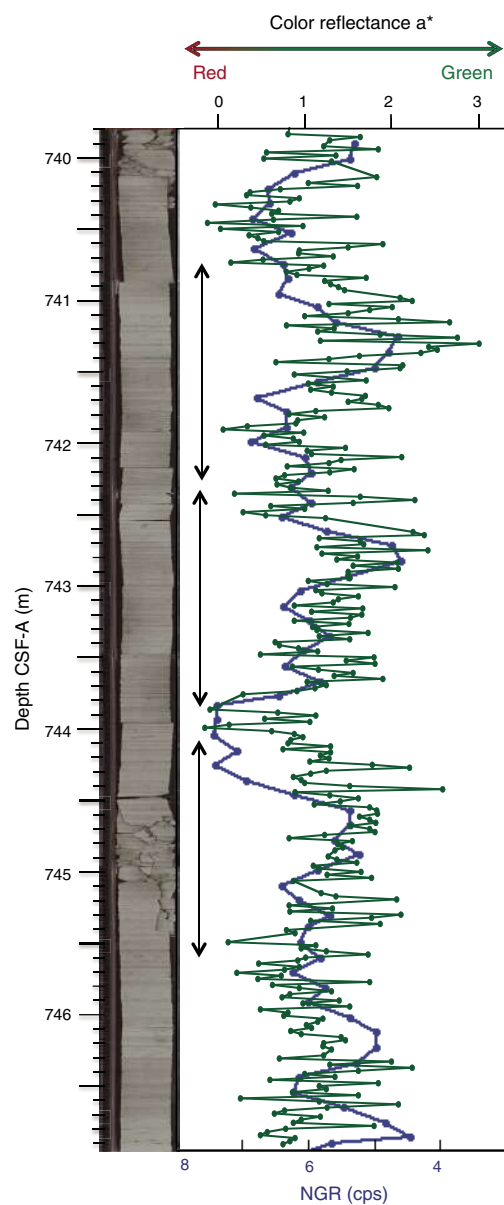
Figure F16. Apparent decimeter-scale cyclicity in Unit II middle Eocene clayey nannofossil chalk, displayed in NGR and color reflectance a* records (371-U1507B-41R).

Biostratigraphy and paleoenvironment

Calcareous nannofossil, planktic foraminifer, and radiolarian biostratigraphic data at Site U1507 (Table **T3**) indicate a mostly continuous Pleistocene to early Miocene age for Hole U1507A and an expanded continuous early Miocene to middle Eocene age for Hole U1507B (Figures **F17**, **F18**).

Paleodepth estimates based on benthic foraminifers are abyssal from the Pleistocene to the uppermost Oligocene and lower bathyal to possibly middle bathyal from the Oligocene to the Eocene. Microfossil assemblages recovered at this site generally show preservation ranging from very good to moderate in Hole U1507A but moderate to poor in Hole U1507B. Microfossil abundance largely varies among all groups. Calcareous microfossils are almost always present, whereas radiolarians are only recorded in the upper part of

Hole U1507A and in the upper and lower parts of Hole U1507B (Figure **F19**).

Calcareous nannofossils

Calcareous nannofossil biozones were assigned to sediments from Holes U1507A (Cores 1H through 46X) and U1507B (Cores 2R through 53R). Analyses are based primarily on core catcher samples (paleontology; PAL), with additional samples from working-half sections to refine ages of selected intervals, particularly key boundaries or hiatuses. Calcareous nannofossil distribution data (Table **T4**) are based on shipboard observations that focus on species that are age diagnostic. The distribution data may not represent the full nannofossil assemblage.

In both Holes U1507A and U1507B, calcareous nannofossils are generally common to abundant except in Samples 371-U1507A-42X-CC, 371-U1507B-9R-CC, and 10R-CC, where they are rare to few. Preservation varies from good to moderately good in the upper sections at the site to moderate and eventually poor in the lower part of the sequence (Figure **F19**). Hole U1507A drilled Pleistocene (nannofossil Zones NN20/NN21 through NN17), Pliocene (nannofossil Zone NN13), and Miocene (nannofossil Zones NN11 through NN4) sections. The sequence recovered in Hole U1507B is early Miocene (Zones NN4 through NN1), Oligocene (Zones NP25 through NP21), and late to middle Eocene (nannofossil Zones NP19/NP20 through NP16).

The uppermost section of Hole U1507A (Samples 1H-1, 25 cm, to 1H-1, 75 cm; 0.25–0.75 m) can be identified as Pleistocene age, with assemblages containing *Gephyrocapsa* spp., *Calcidiscus leptoporus*, *Helicosphaera carteri*, and ceratoliths. The following late Pleistocene interval (Samples 1H-3, 75 cm, to 2H-CC; 3.75–15.98 m) is identified by the presence of *Gephyrocapsa* spp. (>4 μm) and *Helicosphaera sellii*. (Zone NN19). Cores 3H through 31X (19.45–284.37 m) represent an expanded early Pliocene to late Miocene interval. Samples 3H-3, 75 cm, to 19H-CC (19.45–177.75 m) represent Zone NN13, with the top of this interval approximated by the top of *Amaurolithus primus* and the base defined by the base of *Ceratolithus rugosus*. Samples 11H-CC to 19H-CC (101.48–177.75 m) in Zone NN13 record a high number of reworked Eocene and Paleocene nannofossils (e.g., *Chiasmolithus* spp., *Dictyococcites bisectus*, and *Toweius* spp.). Samples 20H-3, 75 cm, to 31X-CC (180.83–284.34 m) are ascribed to Zone NN11 due to the presence of *A. primus* in Sample 29X-CC (263.61 m) and the presence of *Discoaster berggrenii* in Sample 31X-CC (284.34 m). A continuous late to middle Miocene interval from Zones NN10 to NN5 is recorded in Hole U1507A (310.21–335.93 m). The top of *Discoaster hamatus*, recognized between Samples 33X-CC and 34X-3, 74 cm (312.28 ± 2.07 m), is used to define the base of Zone NN10. The base of Zone NN9 correlates with the base of *D. hamatus* (325.58 ± 1.00 m). Between Samples 35X-5, 38 cm, and 35X-CC (327.08 ± 0.50 m), the base of *Catinaster coalitus* marks the base of Zone NN8, whereas the top of *Cyclicargolithus floridanus*, used to approximate the base of Zone NN7, is between Samples 35X-CC and 36X-3, 75 cm (330.61 ± 2.94 m). The base of Zone NN6 is identified by the top of *Sphenolithus heteromorphus*, which is between Samples 36X-3, 75 cm, and 36X-CC (334.74 ± 1.19 m).

The early Miocene is recorded in Holes U1507A and U1507B at 362.40–420.66 and 380.55–442.24 m, respectively. *Helicosphaera ampliaperta* was not found in the assemblages, so the top common occurrence of *Discoaster deflandrei* is used as a secondary marker to approximate the base of Zone NN5 (Backman et al., 2012) at 362.45 m (±5.33 m) in Hole U1507A. Standard biohorizons based

Table T3. Microfossil datums and chrons used to construct Site U1507 age model. T = top, B = bottom, Tc = top common occurrence, Bc = bottom common occurrence. (Continued on next page.) **Download table in CSV format.**

Marker event	Zone	Top core section, interval (cm)	Bottom core, section, interval (cm)	Age (Ma)	Top depth CSF-A (m)	Bottom depth CSF-A (m)	Midpoint depth CSF-A (m)	± (m)
Calcareous nannofossils		371-U1507A-	371-U1507A-					
T *Helicosphaera sellii*		1H-1, 75	1H-3, 75	0.44	0.75	3.75	2.25	1.50
T *Amaurolithus primus*		2H-CC, 16–26	3H-3, 75	4.50	16.08	19.45	17.77	1.69
B *Ceratolithus rugosus*	NN13	19H-CC, 28–38	20H-3,75	5.12	177.75	180.83	179.29	1.54
B *Amaurolithus primus*		29X-CC, 22–32	30X-3,75	7.42	263.71	275.95	269.83	6.12
B *Discoaster berggrenii*	NN11	31X-CC, 24–27	32X-3, 41	8.29	284.37	294.75	289.56	5.19
T *Discoaster hamatus*	NN10	34X-CC, 12–22	34X-3, 74	9.53	310.21	314.34	312.28	2.07
B *Discoaster hamatus*	NN9	35X-3, 138	35X-5, 38	10.55	324.58	326.58	325.58	1.00
B *Catinaster coalitus*	NN8	35X-5, 38	35X-CC, 29–39	10.89	326.58	327.57	327.08	0.50
T *Cyclicargolithus floridanus*		35X-CC, 29–39	36X-3, 75	12.38	327.67	333.55	330.61	2.94
T *Sphenolithus heteromorphus*	NN6	36X-3, 75	36X-CC, 0–10	13.53	333.55	335.93	334.74	1.19
Tc *Discoaster deflandrei*		38X-CC, 0–10	39X-CC, 37–47	15.80	357.11	367.78	362.45	5.33
T *Sphenolithus belemnos*	NN4	41X-CC, 61–71	42X-2, 45	17.95	378.23	389.10	383.67	5.44
B *Sphenolithus belemnos*		43X-CC, 0–10	44X-1, 35	19.03	397.27	402.15	399.71	2.44
B *Sphenolithus disbelemnos*	NN2	45X-CC, 12–22	46X-1, 77	22.76	412.46	416.67	414.57	2.11
		371-U1507B-	371-U1507B-					
T *Sphenolithus belemnos*	NN4	3R-CC, 0–10	4R-CC, 9–19	17.95	392.25	404.67	398.46	6.21
B *Sphenolithus belemnos*		6R-CC, 16–26	7R-3, 70	19.03	424.22	427.40	425.81	1.59
B *Sphenolithus disbelemnos*	NN2	8R-4, 106	8R-5, 34	22.76	438.30	439.09	438.70	0.39
T *Sphenolithus delphix*		8R-7, 50	8R-CC, 22–32	23.11	442.00	442.47	442.24	0.24
T *Sphenolithus ciperoensis*	NN1	10R-CC, 8–18	11R-CC, 5–15	24.43	457.28	466.65	461.97	4.69
T *Sphenolithus predistentus*		16R-CC, 25–35	17R-2, 73	26.93	520.04	521.74	520.89	0.85
B *Sphenolithus ciperoensis*	NP24	19R-CC, 9–19	20R-3, 75	29.62	552.13	555.03	553.58	1.45
B *Sphenolithus distentus*		21R-CC, 36–46	22R-CC, 0–11	30.00	568.15	567.50	567.83	−0.32
T *Reticulofenestra umbilicus*	NP23	25R-CC, 18–28	26R-3, 59	32.02	606.16	608.78	607.47	1.31
T *Isthmolithus recurvus*		26R-CC, 0–10	27R-CC, 0–8	32.49	610.26	616.07	613.17	2.91
T *Coccolithus formosus*	NP22	28R-CC	29R-3, 73	32.92	625.54	637.64	631.59	6.05
Bc *Clausicoccus subdistichus*		30R-3, 45	30R-CC, 0–10	33.87	641.96	642.33	642.15	0.19
T *Discoaster saipanensis*	NP21	31R-3, 65	31R-5, 665	34.44	647.54	650.35	648.95	1.41
B *Reticulofenestra isabellae*	CNE19	33R-CC, 0–10	34R-CC, 14–24	36.49	672.58	682.79	677.69	5.10
Bc *Isthmolithus recurvus*	NP19/NP20	37R-CC, 11–21	38R-CC, 0–10	36.97	711.09	720.45	715.77	4.68
Common *Reticulofenestra erbae*	CNE17	40R-CC, 13–23	40R-CC, 13–23	37.88	739.08	744.47	741.78	2.69
T *Chiasmolithus grandis*		40R-CC, 13–23	41R-CC, 61–71	37.98	739.08	749.96	744.52	5.44
T *Sphenolithus obtusus*		45R-CC, 12–22	46R-CC, 4–14	38.63	788.24	795.69	791.97	3.73
B *Dictyococcites bisectus* (>10 µm)	NP17	51R-CC, 28–38	52R-1, 75	40.36	836.08	846.05	841.07	4.98
T *Sphenolithus furcatolithoides*		52R-2, 75	52R-3, 80	40.48	847.50	849.00	848.25	0.75
Planktic foraminifers		371-U1507A-	371-U1507A-					
T *Globorotalia tosaensis*	PT1a/PT1b	1H-CC, 11–16	2H-CC, 16–26	0.61	6.27	15.98	11.13	4.86
T *Globoquadrina altispira*	PL4/PL5	2H-CC, 16–26	3H-CC, 7–17	3.47	16.08	25.10	20.59	4.51
B *Globorotalia tumida*	M14/PL1	20H-CC, 23–33	21H-CC, 12–22	5.57	187.13	196.28	191.71	4.58
B *Globorotalia plesiotumida*	M13a/M13b	30X-CC, 11–21	31X-CC, 24–27	8.58	279.69	284.34	282.02	2.32
T *Paragloborotalia siakensis*	M12/M13a	34X-CC, 12–22	35X-CC, 29–39	10.46	317.11	327.57	322.34	5.23
T *Fohsella fohsi*	M9b/M10	35X-CC, 29–39	36X-CC, 27–37	11.79	327.67	335.93	331.80	4.13
B *Fohsella fohsi fohsi*	M8/M9a	37X-CC, 24–34	38X-CC, 36–46	13.41	343.91	357.01	350.46	6.55
T *Catapsydrax dissimilis*	M3/M4a	40X-CC, 33–43	41X-CC, 0–10	17.54	373.50	378.13	375.82	2.32
		371-U1507B-	371-U1507B-					
T *Paragloborotalia pseudokugleri*	M1b	6R-CC, 16–26	7R-CC, 9–19	21.31	424.22	432.52	428.37	4.15
T *Globigerina euapertura*	O7	7R-CC, 9–19	8R-CC, 22–32	22.96	432.62	442.47	437.55	4.93
B *Paragloborotalia pseudokugleri*	O6/O7	8R-CC, 22–32	9R-CC, 0–10	25.40	442.57	449.87	446.22	3.65
T *Paragloborotalia opima*	O5/O6	14R-CC, 0–10	15R-CC, 0–10	26.93	499.00	509.37	504.19	5.19
T *Turborotalia ampliapertura*	O2/O3	20R-CC, 0–10	21R-CC, 36–46	30.28	555.13	568.05	561.59	6.46
B *Paragloborotalia opima*	O2	21R-CC, 36–46	22R-CC, 0–11	30.72	568.15	567.50	567.83	−0.33
T *Pseudohastigerina naguewichiensis*	O1/O2	27R-CC, 0–8	28R-CC, 0–10	32.00	616.15	625.44	620.80	4.64
T *Globigerinatheka index*	E15/E16	30R-CC, 0–10	31R-CC, 12–22	34.61	642.33	654.12	648.23	5.89
T *Orbulinoides beckmanni*	E12/E13	49R-CC, 0–10	50R-CC, 0–10	40.03	825.64	835.51	830.58	4.93
B *Orbulinoides beckmanni*	E11/E12	51R-CC, 28–38	52R-CC, 15–25	40.49	836.08	855.23	845.66	9.58
Benthic foraminifers		371-U1507B-	371-U1507B-					
T *Nuttallides truempyi*		29R-CC, 0–10	30R-CC, 0–10	33.89	625.44	642.33	633.89	8.45
Radiolarians		371-U1507B-	371-U1507B-					
B *Calocycletta serrata*	RN02/RN01–RP21b	6R-CC, 16–26	7R-CC, 9–19	21.30	424.22	432.62	428.42	4.20
T *Theocyrtis annosa*	RN02/RN01–RP21b	7R-CC, 9–19	8R-CC, 22–32	21.30	432.62	442.47	437.55	4.93
B *Calocycletta robusta*	RN01–RP21b	12R-CC, 18–28	13R-CC, 0–10	26.10	480.13	488.94	484.54	4.41
T *Dictyoprora mongolfieri*	RP19	30R-CC, 0–10	31R-CC, 12–22	33.91	642.43	654.12	648.28	5.85
T *Thyrsocyrtis tetracantha*	RP19/RP18	33R-CC, 0–10	34R-CC, 14–24	35.70	672.58	682.79	677.69	5.11
B *Calocyclas turris*	RP17	42R-CC, 0–10	43R-CC, 0–10	37.96	757.27	762.59	759.93	2.66

Table T3 (continued).

Marker event	Zone	Top core section, interval (cm)	Bottom core, section, interval (cm)	Age (Ma)	Top depth CSF-A (m)	Bottom depth CSF-A (m)	Midpoint depth CSF-A (m)	± (m)
B *Cryptocarpium azyx*	RP17–RP18	43R-CC, 0–10	44R-CC, 0–10	38.26	762.69	777.61	770.15	7.46
T *Calocycloma ampulla*	RP16/RP17	43R-CC, 0–10	44R-CC, 0–10	38.36	762.69	777.61	770.15	7.46
T *Anthocyrtoma* sp.	RP16	43R-CC, 0–10	44R-CC, 0–10	38.47	762.69	777.61	770.15	7.46
B *Zealithapium mitra*	zRP13	49R-CC, 0–10	50R-CC, 0–10	39.30	825.64	835.51	830.58	4.93
T *Artobotrys biaurita*				39.30	386.08	855.23	845.66	9.58
T *Sethochytris triconiscus*	RP15/RP16	51R-CC, 28–38	52R-CC, 15–25	40.18	836.08	855.23	845.66	9.58
T *Lophocyrtis biaurita*	RP15/RP16	51R-CC, 28–38	52R-CC, 15–25	40.70	836.08	855.23	845.66	9.58
T *Podocyrtis mitra*	RP15	50R-CC, 0–10	51R-CC, 28–38	41.22	835.61	835.98	835.80	0.18

on sphenolith markers are used to define Zones NN3 through NN1 in both holes. The top of *Sphenolithus belemnos*, which marks the base of Zone NN4, is found in Samples 371-U1507A-43X-CC and 371-U1507B-6R-CC. The base of *Sphenolithus disbelemnos*, which approximates the base of Zone NN2, is recognized between Samples 371-U1507A-45X-CC and 46X-1, 77 cm (414.57 ± 2.11 m), and between Samples 371-U1507B-8R-4, 106 cm, and 8R-5, 34 cm (438.70 ± 0.39 m).

The Oligocene is recorded in Hole U1507B in Samples 8R-7, 50 cm, to 30R-3, 45 cm (442.00–641.96 m). The Oligocene/Miocene boundary occurs just above the top of *Sphenolithus delphix* at 442.24 m (±0.24 m) between Samples 8R-7, 50 cm, and 8R-CC (Figure **F20**). This location agrees with the paleomagnetic data, which indicates the base of Chron C6Cn.2n is at 441.73 m (±0.025 m). The top and base of *Sphenolithus ciperoensis* are used to constrain the base of Zone NN1 (461.97 ± 4.69 m) and the base of Zone NP24 (553.58 ± 1.45 m), respectively. The tops of *Sphenolithus distentus* and *Sphenolithus predistentus*, observed between Samples 16R-CC and 17R-2, 73 cm (520.89 ± 0.85 m), indicate the top of Zone NP24. The top of *Reticulofenestra umbilicus* is recognized between Samples 25R-CC and 26R-3, 59 cm (607.47 ± 1.31 m), and marks the top of Zone NP22. The top of *Coccolithus formosus*, observed between Samples 28R-CC and 29R-3, 73 cm (631.59 ± 6.05 m), marks the top of Zone NP21.

The late to middle Eocene, recorded through an expanded 213.59 m thick section, represents Zones NP19/NP20 through NP16. The Eocene/Oligocene boundary occurs close to the base acme of *Clausicoccus subdistichus*, recorded between Samples 30R-CC and 30R-3, 45 cm (642.15 ± 0.19 m), and the top of the rosette discoasters (i.e., *Discoaster barbadiensis* and *Discoaster saipanensis*), which marks the base of Zone NP21 (648.95 ± 1.41 m; Figure **F20**). This location agrees with the paleomagnetic data, which indicate the base of Chron C13n occurs at 640.76 m (±0.025 m). The base of *Isthmolithus recurvus* defines the base of Zone NP19/NP20 and is recorded between Samples 37R-CC and 38R-CC (715.77 ± 4.68 m). The base of *Reticulofenestra isabellae* at 36.49 Ma (Agnini et al., 2014) is used to further refine the biostratigraphic resolution in Zone NP19/NP20 and is found between Samples 33R-CC and 34R-CC (741.78 ± 2.69 m). The top of *Chiasmolithus grandis*, which marks the base of Subzone CP15b (Okada and Bukry, 1980), is used to approximate the base of Zone NP18. However, the short-lived (37.70–38.07 Ma; Agnini et al., 2014) acme of *Reticulofenestra erbae*, which occurs in interval 40R-CC, 13–23 cm (738.98–739.08 m), provides further age constraint and is used to approximate the base of the late Eocene (Priabonian). The top of *Chiasmolithus solitus* is not used to mark the base of Zone NP17 because of the high number of reworked specimens found throughout the section. In-

stead, the base of *D. bisectus* (>10 μm), found between Samples 51R-CC and 52R-1, 75 cm (841.07 ± 4.98 m), is used to recognize the base of Zone NP17 and to mark the initiation of the MECO; however, in Hole U1507B, this event cannot be accurately constrained due to poor recovery of Core 51R. The top of *Sphenolithus furcatolithoides*, recorded between Samples 52R-2, 75 cm, and 52R-3, 80 cm (848.25 ± 0.75 m), occurs just below the MECO. An incomplete record of *S. predistentus* and *Sphenolithus spiniger* means that the top of the MECO interval cannot be approximated, but the base of *Sphenolithus obtusus* is used to define the end of the post-MECO interval and occurs between Samples 49R-CC and 50R-2, 81 cm (826.94 ± 1.295 m; Figure **F21**).
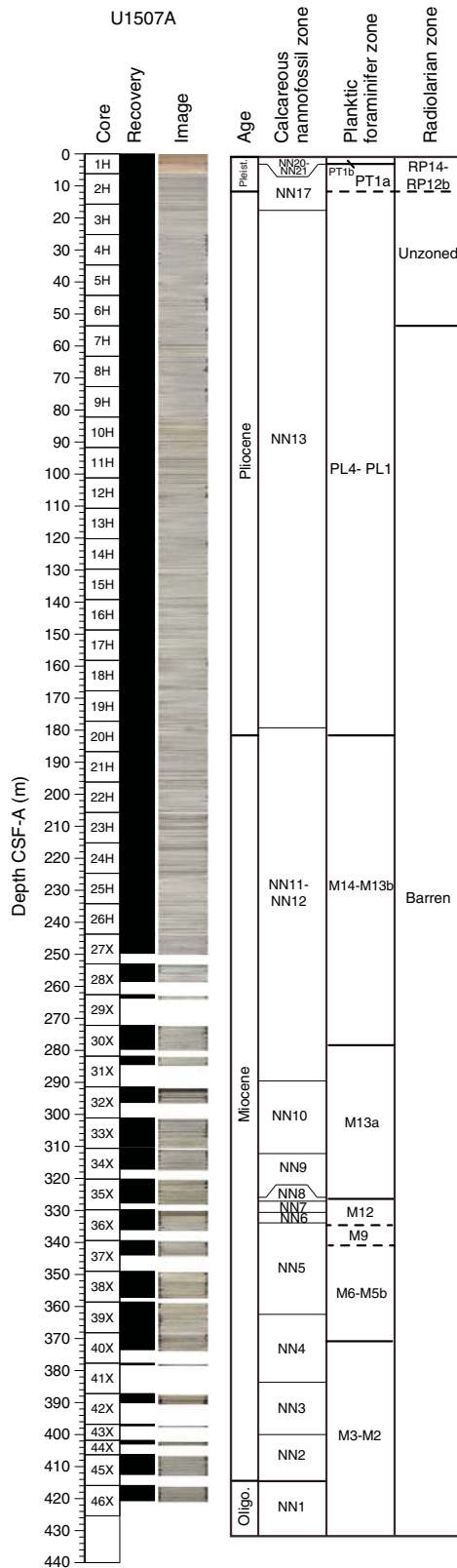
Planktic foraminifers

Core catcher samples were examined for their planktic foraminifer assemblages in Holes U1507A and U1507B. Planktic foraminifer preservation is generally moderate to good but is poor in Cores 371-U1507A-29X through 45X and 371-U1507B-10R through 14R (Table **T5**; Figures **F19**, **F22**). Depth positions and age estimates of biostratigraphic events can be derived from the presence of marker species and the stratigraphic distribution of planktic foraminifers (Tables **T3**, **T5**).

The upper 187.03 m of core from Hole U1507A contains a diverse assemblage of planktic foraminifers from the Pleistocene and Pliocene. Samples 371-U1507A-1H-CC to 2H-CC (6.27–15.98 m) contain *Globorotalia truncatulinoides* and *Globorotalia tosaensis*, indicative of a Pleistocene age. Samples 3H-CC to 20H-CC (25.10–187.13 m) consistently contain assemblages of Pliocene marker species such as *Globoquadrina altispira*, *Globorotalia tumida*, *Sphaeroidinellopsis seminulina*, *Sphaeroidinellopsis kochi*, and *Hirsutella margaritae*. Occasional specimens of *Globigerinatheka index* and *Catapsydrax unicavus* throughout this interval indicate reworking of older sediments, perhaps from outcrops at shallower water depths. Occurrences of *G. truncatulinoides* and *G. tosaensis* within this interval indicate downhole contamination. The base of *G. tumida* in Samples 20H-CC to 21H-CC (191.71 ± 4.58 m) tentatively suggests that Samples 3H-CC to 20H-CC (25.20–187.03 m) are within Zones PL4 through PL1.

The interval spanning Samples 21H-CC to 30X-CC (196.28–279.69 m) contains late Miocene planktic foraminifers from Zone M14 to Subzone M13b. The base of *Globorotalia plesiotumida* marks the Subzone M13b/M13a boundary between Samples 30X-CC and 31X-CC (282.02 ± 2.32 m). Below Sample 30X-CC, dissolution-resistant species such as *S. seminulina* and *Dentoglobigerina venezuelana* are commonly found. Samples 36X-CC to 37X-CC (336.03–343.81 m) yield the middle Miocene *Fohsella* lineage (*Fohsella fohsi fohsi*, *Fohsella peripheroacuta*, and *Fohsella robusta*),

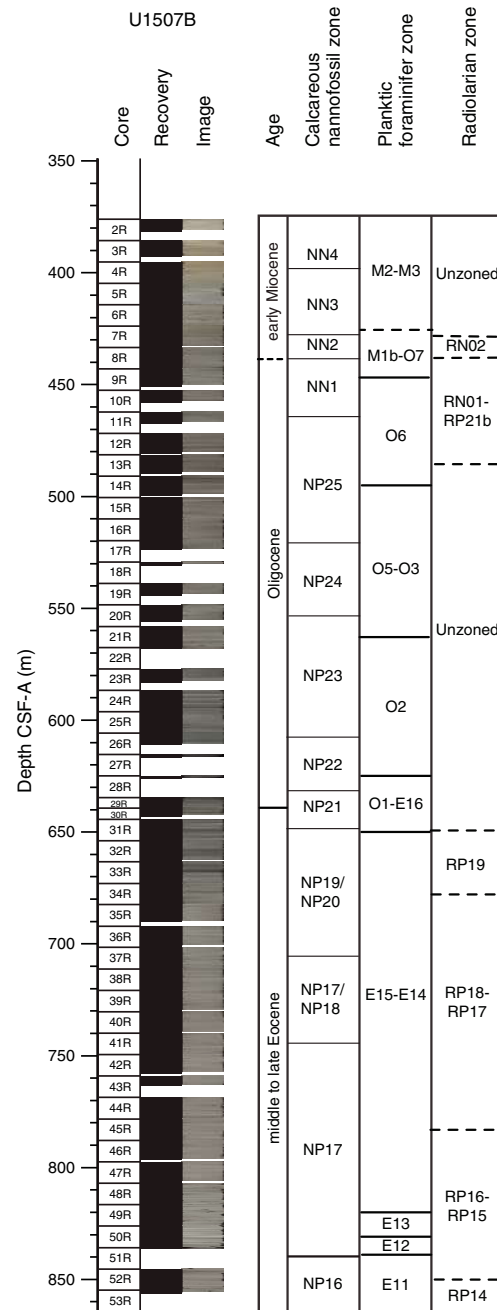Figure F17. Biozonations, Hole U1507A.

Figure F18. Biozonations, Hole U1507B.

change in this group has been reported around the Subzone M5b/M5a boundary (Abdul Aziz et al., 2008), indicating the subzone boundary may be located between these samples. The interval between Samples 38X-CC and 40X-CC (357.11–373.40 m) is assigned to Zone M6 through Subzone M5b based on the absence of *F. peripheroacuta*.

Foraminifer assemblages recovered from Hole U1507B are indicative of an early Miocene to Eocene age. The occurrence of *Catapsydrax dissimilis* and absence of *Paragloborotalia kugleri* and *Paragloborotalia pseudokugleri* in Samples 371-U1507B-41X-CC to 46X-CC (378.23–420.56 m) indicate this interval is early Miocene in age (Zones M3 through M2). The uppermost interval, including Samples 2R-CC to 6R-CC (380.55–424.22 m), contains *C. dissimilis*

indicating this interval is in Zone M9. The coiling direction of *Paragloborotalia* spp. changes from dominantly sinistral to random between Samples 40X-CC and 41X-CC (375.82 ± 2.32 m). The coiling

Figure F19. Microfossil abundance and preservation, Site U1507. Abundance: D = dominant, A = abundant, C = common, F = few, R = rare, P = present, tr = trace, B = barren. Preservation: E = excellent, VG = very good, G = good, M = moderate, P = poor.
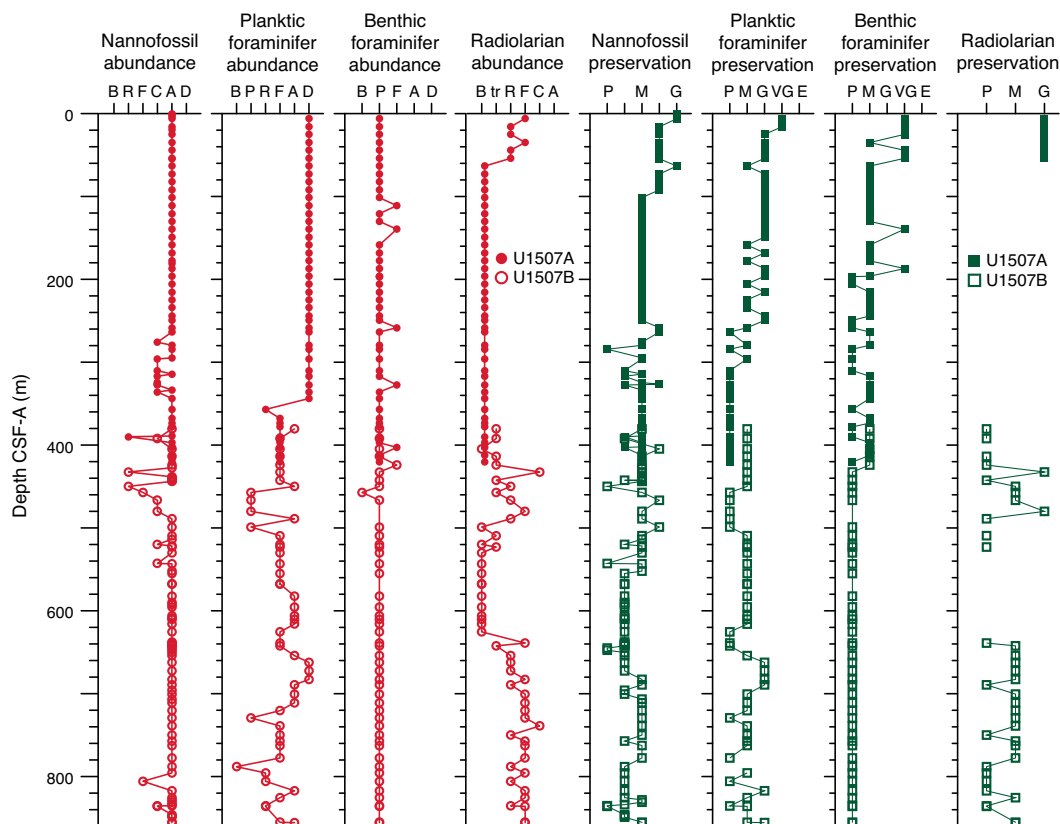
Table T4. Nannofossil distribution and occurrence data, Site U1507. **Download table in CSV format.**

in absence of *P. kugleri* and *P. pseudokugleri*, an assemblage that indicates an early Miocene age.

The top of *Globigerina euapertura*, whose first occurrence is slightly below the Miocene/Oligocene boundary in New Zealand, is used to approximate the transition into the Oligocene between Samples 371-U1507B-7R-CC and 8R-CC (437.55 ± 4.93 m). The top and base of *P. pseudokugleri*, identified between Samples 6R-CC and 7R-CC (428.37 ± 4.15 m) and between Samples 8R-CC and 9R-CC (446.22 ± 3.65 m), respectively, are additional evidence that the Miocene/Oligocene boundary lies within this interval.

Although the absence of *Hantkenina* spp. prevents determination of the Eocene/Oligocene boundary, the late Eocene Zone E16/E15 boundary is well defined by the top of *G. index* between Samples 371-U1507B-30R-CC and 31R-CC (648.23 ± 5.89 m). This species dominates the assemblages to the base of Hole U1507B (Table **T5**). Samples 50R-CC and 51R-CC contain *Orbulinoides beckmanni*, whose range defines Zone E12 and coincides with the MECO (Figure **F21**; Edgar et al., 2013).
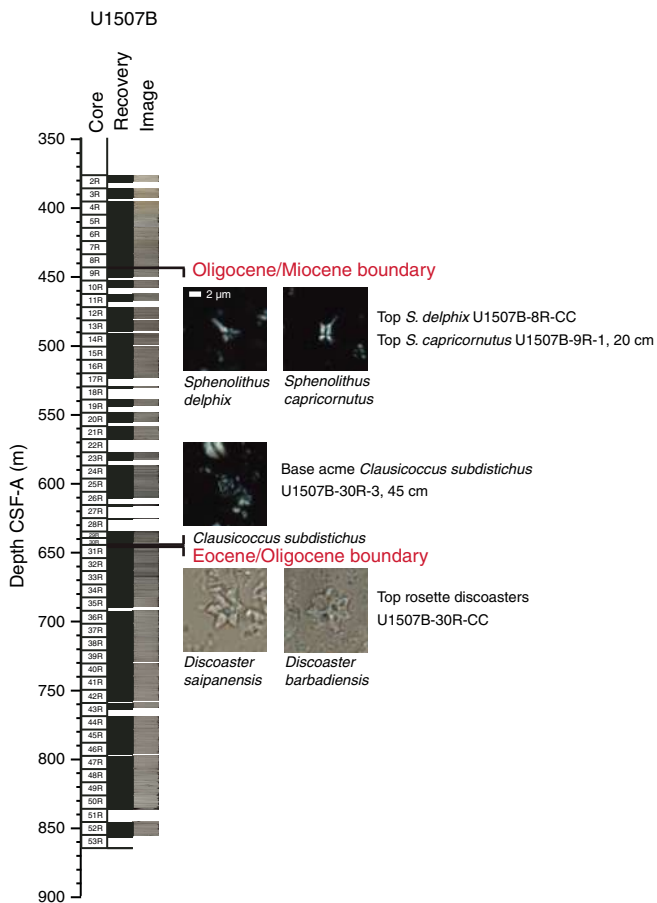
Benthic foraminifers

Benthic foraminifers were examined semiquantitatively in core catcher samples from Holes U1507A and U1507B and in additional working-half sections (intervals 371-U1507A-22H-1, 51–53 cm, and 22H-1, 95–97 cm; Section 371-U1507B-24R-7; Table **T6**). Because benthic foraminifers are rare relative to total particles in the >63 µm fraction in most of the examined samples, they are generally

classified as present. However, in five samples from Hole U1507A, benthic foraminifers can be described as few, with one sample from Hole U1507B (Sample 10R-CC) completely barren. In Hole U1507A, benthic foraminifer preservation is very good through Pleistocene and Pliocene Cores 1H through 6H but is recorded as generally moderate to poor through most of the remaining Miocene and uppermost Oligocene (Figure **F19**). Preservation in Hole U1507B is moderate through the top five early Miocene samples and poor through the rest of the hole. In Hole U1507A, 3075 specimens were picked from 47 samples and 141 taxa were identified; in Hole U1507B, 1664 specimens were picked from 48 samples and 108 were taxa identified. Most samples are strongly dominated by calcareous taxa.

Assemblages in the Pleistocene and in the top four cores (Samples 371-U1507A-3H-CC to 6H-CC; 25.10–54.09 m) of the Pliocene in Hole U1507A are dominated by mixed infaunal and epifaunal morphogroups. These indicate meso-eutrophic conditions at the seafloor (Jorissen et al., 2007). Stilostomellids, nodosariids, miliolids, pleurostomellids, *Bolivina* spp., *Fissurina* spp., *Fursenkoina* spp., *Anomalinoides globosus, Globocassidulina subglobosa*, and *Oridorsalis umbonatus* are the most representative taxa.

Miocene and Oligocene assemblages are dominated by epifaunal morphogroups and in some samples by mixed infaunal–epifaunal morphogroups. Nodosariids, stilostomellids, *O. umbonatus, G. subglobosa, Buliminella grata, Vulvulina spinosa, Pullenia bulloides, Bolivina* spp., *Pleurostomella* spp., and *Uvigerina* spp. are the most common taxa among infaunal morphogroups. *Cibicides* spp., *Cibicidoides* spp. (including *Cibicidoides mundulus* and *Cibicidoides dohmi), Gyroidinoides* spp., *Anomalinoides* spp. (including

Figure F20. Nannofossil datums constraining Miocene/Oligocene and Oligocene/Eocene boundaries, Hole U1507B. *S. delphix, S. capricornutus,* and *C. subdistichus* are in crossed nicols; *D. saipanensis* and *D. barbadiensis* are in parallel light.

The assemblages of the Pleistocene to uppermost Oligocene indicate deposition at abyssal depths. This deposition is inferred from the occurrence of typically abyssal (e.g., *Favocassidulina favus, N. umbonifera,* and *Cibicidoides havanensis;* van Morkhoven et al., 1986) and lower bathyal to abyssal taxa (e.g., *Anomalinoides globulosus, Bolivina* spp., *B. grata, C. mundulus, Laticarinina pauperata, P. wuellerstorfi, G. subglobosa,* and *V. spinosa;* Tjalsma and Lohmann, 1983; van Morkhoven et al., 1986; Hayward et al., 2010). Reworked shallower taxa were also identified in intervals 371-U1507A-22H-1, 51–53 cm, and 22H-1, 95–97 cm. These intervals contain a mixture of benthic foraminifer preservation states (from moderate to very poor and some completely pyritized tests). In addition to typically deep-water taxa, other species that resemble recent shallow-water taxa living on the shelves in New Caledonia (e.g., *Discorbinella, Planulina, Laticarinina,* and *Planularia;* Debenay, 2012) were observed.

The assemblages of the rest of the Oligocene and the Eocene, including Samples 371-U1507B-12R-CC to 49R-CC (80.13–825.64 m), indicate deposition in the lower bathyal zone. This deposition is inferred from the common occurrence of lower bathyal species (e.g., *A. semicribratus, Cibicidoides bradyi, G. subglobosa, Gyroidinoides neosoldanii, Eggerella bradyi, O. umbonatus,* and *P. bulloides*) and from the occurrence of taxa with an upper depth limit at 1000 m (*C. mundulus;* van Morkhoven et al., 1986). The Eocene sequence has a similar assemblage that includes *C. mundulus, O. umbonatus, Pleurostomella* spp., stilostomellids, *S. cubensis,* and *N. truempyi. C. dohmi* is occasionally common to abundant in the Eocene samples and, together with the lower bathyal–abyssal species *V. spinosa,* indicates a paleodepth in the lower part of the bathyal zone.

The presence of *N. truempyi, O. umbonatus, Karreriella chilostoma,* and *Vulvulina bortonica* in the lowermost samples from Hole U1507B (Samples 50R-CC to 53R-CC) may indicate shallower, deep middle bathyal paleodepth.

The top occurrence of *N. truempyi* in Sample 371-U1507B-30R-CC (642.33–642.43 m) allowed identification of the Eocene/Oligocene boundary between this sample and Sample 29R-CC (638.95–639.05 m).

Assemblages overlying the MECO are very poor, and a population of small specimens of trochamminids strongly dominates the benthic fauna through the MECO and pre-MECO intervals (Samples 371-U1507B-50R-CC to 52R-CC; 835.51–855.33 m; Figure **F21**). The agglutinated tests of trochamminid specimens are heavily recrystallized, and their strong dominance indicates a stressed environment during this time, possibly combined with CaCO$_3$ dissolution in bottom waters.

Ostracods

Ostracod preservation, abundance, assemblage composition, and paleodepth estimates were investigated using core catcher samples and additional samples from working-half sections (Figure **F23**). Ostracods are rare to common in intervals 371-U1507A-1H-CC, 11–16 cm, through 30X-CC, 11–21 cm (6.17–279.69 m). Barren intervals are found in intervals 31X-CC, 24–27 cm, through 46X-CC, 26–36 cm (284.34–420.66 m). In addition, the entirety of Hole U1507B is also barren of ostracods (Figure **F19**).

In Hole U1507A, 152 specimens were picked and 46 taxa were identified. The fossils are relatively well preserved for most nonbarren samples, and the visual preservation index (VPI) (Dwyer et al., 1995) ranges from 4 to 5 (Figure **F23**). The abundance data are standardized by presenting the number of specimens per size tray,

Anomalinoides semicribratus), *Planulina wuellerstorfi,* and *Nuttallides umbonifera* are the most common among epifaunal taxa. This assemblage suggests oligotrophic to mesotrophic conditions at the seafloor (Jorissen et al., 2007).

Most Oligocene samples are characterized by small-sized specimens (Samples 371-U1507B-10R-CC to 30R-CC; 457.18–642.43 m), with trochamminids making up half of the assemblages in Sample 11R-CC where abundant siliceous (diatoms and radiolarians) and calcareous microfossils (calcareous dinoflagellates) occur. Trochamminids behave as opportunistic taxa, and they may proliferate at the seafloor under changing trophic conditions and varying oxygenation of bottom waters (Kaminski and Gradstein, 2005). Their high abundance indicates environmental stress. A small number of shelfal warm-water taxa, including *Asterigerina* spp., *Amphistegina* spp., and *Cibicides vortex,* probably deposited by turbidites, were recovered from Samples 25R-CC, 26R-CC, and 28R-CC.

Eocene benthic foraminifers are poorly preserved throughout the lower part of Hole U1507B, including Samples 31R-CC to 53R-CC (654.12–855.74 m). Assemblages are much less diverse and abundant compared with the Oligocene and Miocene sequences and are mostly dominated by epifaunal taxa such as *C. mundulus, C. dohmi, Nuttallides truempyi,* and *Anomalinoides* spp. Nodosariids, stilostomellids, *Spiroplectammina cubensis, O. umbonatus,* and pleurostomellids were identified among the infaunal taxa.

Figure F21. Nannofossil and planktic and benthic foraminiferal datums and their respective ranges across recovered MECO event compared with the species' documented ranges in complete MECO sections, Hole U1507B. B = base, T = top. CN = calcareous nannofossil.
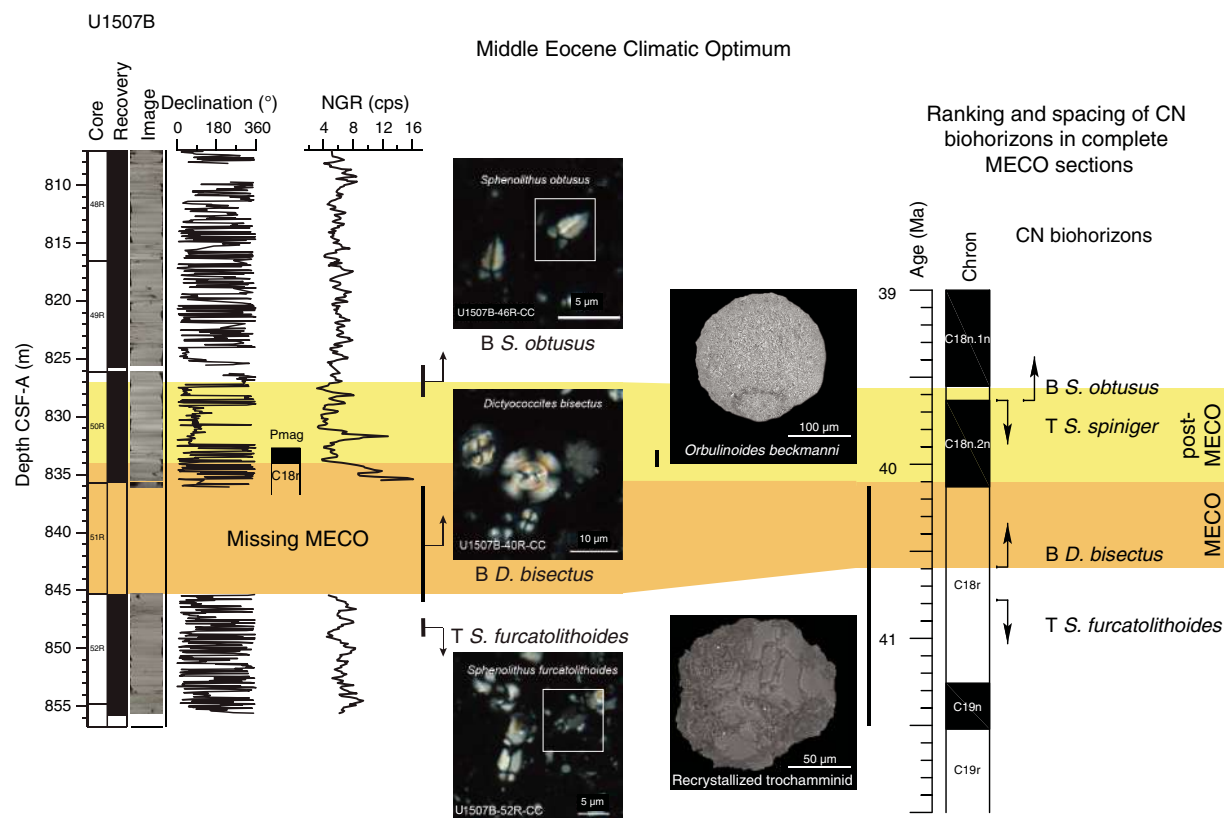

Table T5. Planktic foraminifer distribution and abundance data, Site U1507. **Download table in CSV format.**

which ranges from 1 to 7. The dominant genera are *Krithe* spp. and *Poseidonamicus* spp. Other abundant genera include *Bradleya*, *Cytheropteron*, and *Henryhowella*. In Hole U1507B, only one carapace specimen (*Philoneptunus* sp.) is found in interval 31R-4, 23–25 cm (648.440 m).

Paleoenvironmental interpretations based on ostracod assemblages are possibly biased due to numerous barren samples and repeated intervals with reworking. Nevertheless, paleodepth estimates based on ostracods suggest a continuous deep-sea setting (lower bathyal) of sediments in intervals 371-U1507A-1H-CC, 11–16 cm, through 30X-CC, 11–21 cm (6.17–279.69 m).

The disappearance of ostracods corresponds to the ooze–chalk transition in Cores 371-U1507A-30X through 32X (Figure **F23**). The barren intervals probably result from poor preservation, which is also inferred for the nannofossil and planktic and benthic foraminifer assemblages in similar samples (Figure **F19**).

Radiolarians

Core catcher samples from Holes U1507A and U1507B were analyzed for the occurrence of radiolarians (Samples 371-U1507A-1H-CC to 46X-CC [6.17–420.66 m] and 371-U1507B-2R-CC to 53R-CC [380.55–855.74 m]). Due to time constraints, shipboard observations focused on the presence of age diagnostic species. Distribution data do not fully represent the full radiolarian assemblage (Table **T7**). When observed, other siliceous microfossils were noted.

In Hole U1507A, radiolarians are rare to few in Cores 1H through 6H but with overall good preservation (Figure **F19**).

Sponge spicules occur in great abundance in all six samples. The uppermost sample (371-U1507A-1H-CC) is tentatively assigned to Subzone RN12b–Zone RN14 due to the absence of *Collosphaera tuberosa* (base of Zone RN15) and the presence of *Cycladophora davisiana*, the base of which occurs in the lower part of Subzone RN12b. Samples 2H-CC to 6H-CC (15.98–54.09 m) are dominated by Spumellaria and Collosphaeridae but are not assigned to any radiolarian zone because marker species were absent. Reworked Miocene *Cyrtocapsella* spp. was observed in Samples 3H-CC and 4H-CC. The remaining cores are barren of radiolarians.

In Hole U1507B, radiolarians are present in varying abundance in Samples 2R-CC to 13R-CC (380.55–489.04 m), although with moderate to poor preservation (Figure **F19**). The interval between Cores 14R and 28R (498.90 and 625.54 m) is basically barren of radiolarians, except for trace amounts in two samples. Radiolarians are rare to common in abundance in Samples 29R-CC to 53R-CC (638.95–855.74 m) but are poorly to moderately preserved and often infilled with clay.

The base of early Miocene Zone RN02 is at 437.55 m (±4.93 m) based on the top of *Theocyrtis annosa* (21.3 Ma) and the base of *Calocycletta serrata* in Sample 371-U1507B-7R-CC (Figure **F18**; Table **T3**). The top of the zone cannot be recognized. Samples 8R-CC to 12R-CC (442.57–480.03 m) are tentatively assigned to late Oligocene Subzone RP21b through early Miocene Zone RN01 based on the presence of *Calocycletta robusta* (Subzone RP21b through Zone RN01) and the absence of *C. serrata*. The base of *Cyrtocapsella tetrapera*, which defines the base of Zone RN01, was observed in the same sample as the base of *C. serrata* (Zone RN02).

Based on nannofossil and planktic foraminifer biostratigraphy, Cores 371-U1507B-29R through 53R are late to middle Eocene in

Figure F22. Preservation state of planktic foraminifers. Scale bars = 50 μM. A. Very good (371-U1507A-1H-CC). B. Good (371-U1507B-35R-CC). C. Moderate (25R-CC). D. Poor (13R-CC).
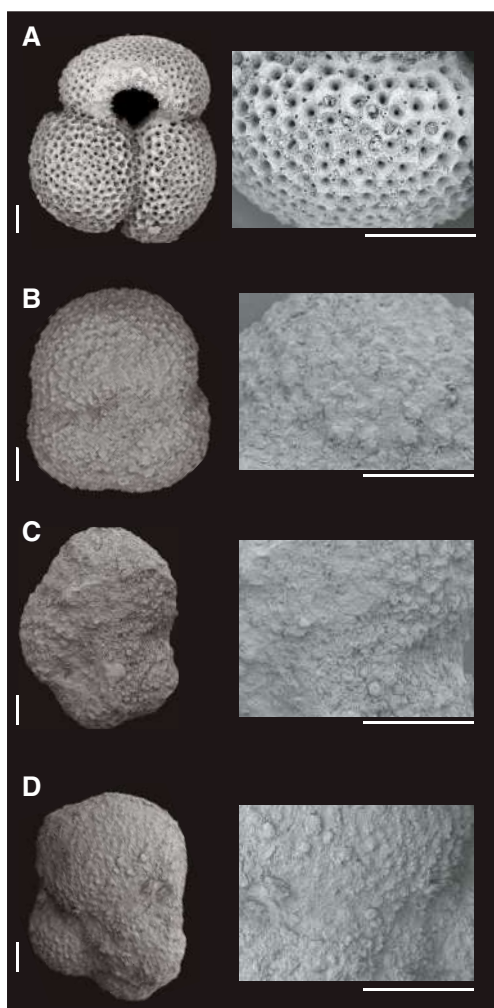
age (Figure **F18**). This interval can be correlated with low-latitude radiolarian Zones RP19 through RP14. However, many low-latitude index species are absent or rare and sporadic in occurrence. The top of Zone RP19 is determined by the top of *Dictyoprora mongolfieri* (33.9 Ma) between Samples 30R-CC and 31R-CC (648.28 ± 5.85 m). The Zone RP18/RP19 boundary is recognized between Samples 33R-CC and 34R-CC (677.69 ± 5.11 m) by the top of *Thyrsocyrtis tetracantha* (35.4 Ma). The base of Zone RP17–RP18 is determined by the base of *Cryptocarpium azyx* (38.26 Ma) between Samples 43R-CC and 44R-CC (770.15 ± 7.46 m). *C. azyx* is only found in Sample 43R-CC. The base of *Calocyclas turris* is found between Samples 42R-CC and 43R-CC (759.93 ± 2.66 m) and occurs in the lower part of Zone RP17 (37.96 Ma). The Zone RP16/RP17 boundary is recognized between Samples 43R-CC and 44R-CC (770.15 ± 7.46 m) based on the tops of *Calocycloma ampulla* (38.36 Ma) and *Anthocyrtoma* sp. (38.47 Ma). The top of Zone RP14–RP15 is recognized between Samples 51R-CC and 52R-CC (845.66 ± 9.58 m) based on the tops of *Sethochytris triconiscus* (40.18 Ma) and *Artobotrys biaurita* (40.5 Ma). The top of *Podocyrtis mitra* (41.22 Ma), which defines the base of Zone RP15, is found between Samples 50R-CC and 51R-CC (835.8 ± 0.18 m). The southwest Pacific Zealandia radiolarian zonation (zRP zones) was not applied at this site due to the absence or sporadic occurrence of marker species. Only the base of *Zealithapium mitra* (base of Zone zRP13) was observed between Samples 49R-CC and 50R-CC (830.58 ± 4.93 m).

Palynology

A low-resolution palynological study was carried out on 10 core catcher samples from Site U1507 (4 from Hole U1507A and 6 from Hole U1507B) at an average sampling resolution of 1 sample per 10 cores. Samples were effectively barren of palynomorphs, which is not unexpected in pelagic carbonate deposits that contain little organic carbon (see **Lithostratigraphy** and **Geochemistry**). Trace amounts of dinocysts were found in Sample 371-U1507A-7H-CC (63.47 m) from the upper part of Subunit Ia and in Sample 371-U1507B-52R-CC (855.33 m) from the bottom of Unit II. These are consistent with Pliocene and middle Eocene ages, respectively, as inferred from nannofossil and planktic foraminifer biostratigraphy.

Table T6. Benthic foraminifer distribution and abundance data, Site U1507. **Download table in CSV format.**

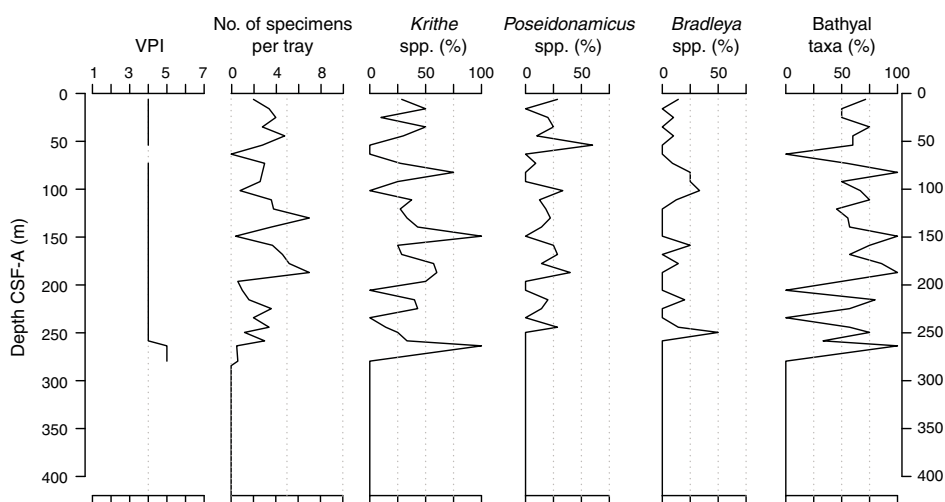Figure F23. Summary of ostracod preservation, abundance, and assemblage composition, Hole U1507A.

Table T7. Radiolarian distribution data, Site U1507. **Download table in CSV format.**

Paleomagnetism

Pass-through paleomagnetic measurements were performed on all archive-half sections from Holes U1507A and U1507B. Inclination data were used to determine magnetic polarity stratigraphy. To supplement and verify pass-through paleomagnetic data, 123 discrete samples were taken from intervals with minimal coring disturbance. For Unit I in Hole U1507B, samples were often collected on top of apparent turbidite layers. All discrete samples were subjected to stepwise alternating field (AF) demagnetization, as described in **Paleomagnetism** in the Expedition 371 methods chapter (Sutherland et al., 2019a). To investigate the magnetic fabric, all discrete samples were measured for anisotropy of magnetic susceptibility (AMS).

Paleomagnetic results

Paleomagnetic data of archive halves, including natural remanent magnetization (NRM) intensity and inclination of remanence, show variable quality for different lithostratigraphic units (Figures **F24**, **F25**). In Hole U1507A, the NRM intensity is on the order of 10^{-2} A/m, with slightly higher average values below ~237 m (Core 371-U1507A-26H). The NRM inclination before demagnetization is

mostly positive, likely reflecting a drilling-induced overprint. Inclination values after 20 mT AF cleaning were filtered using a 10-point moving average. Cores 1H through 6H (0–53.8 m) are characterized by negative remanence inclinations (i.e., normal polarity), although some swings toward positive inclination (reversed polarity) were observed. Down to Core 23H at 215 m, inclination data show a series of reversals, although without a defined bimodal clustering (Figure **F26A**). In Cores 23H through 46X (215–420.3 m), inclinations oscillate randomly around zero with no clear polarity pattern. The average inclination for Hole U1507A is about −20°. The scattered paleomagnetic inclinations likely derive from drilling-induced overprint and coring-related sediment deformation.

Reliable paleomagnetic results were obtained for most intervals in Hole U1507B. The NRM intensity of lithostratigraphic Subunits Ib and Ic ranges between 10^{-2} and 1 A/m with a gentle increasing trend downcore (Figure **F25**). A particularly well defined series of positive and negative inclination shifts was observed after 20 mT AF cleaning in this part of Unit I (Cores 2R through 34R; 376–682 m). The histogram of inclination values indicates two clear peaks clustered around ±45° (Figure **F26B**). Sediments in lithostratigraphic Unit II, from Cores 35R through 53R (682–856 m), are characterized by a marked decrease of NRM intensity to ~10^{-4} A/m (i.e., about two orders of magnitude lower than Subunits Ib and Ic). This decrease results in generally scattered inclination values with no

Figure F24. Pass-through paleomagnetic data, Hole U1507A. Black dots = NRM intensity and inclination, gray dots = inclination after 20 mT AF cleaning interpolated by 10-point moving average (black line), red dots = inclination of ChRM directions from discrete sample analysis. Magnetic polarity: black = normal, white = reversed, gray = unidentified.

Figure F25. Pass-through paleomagnetic data, Hole U1507B. Black dots = NRM intensity and inclination, gray dots = inclination after 20 mT AF cleaning interpolated by 10-point moving average (black line), red dots = inclination of ChRM directions from discrete sample analysis. Magnetic polarity: black = normal, white = reversed, gray = unidentified. Correlation with GPTS2012 is shown.
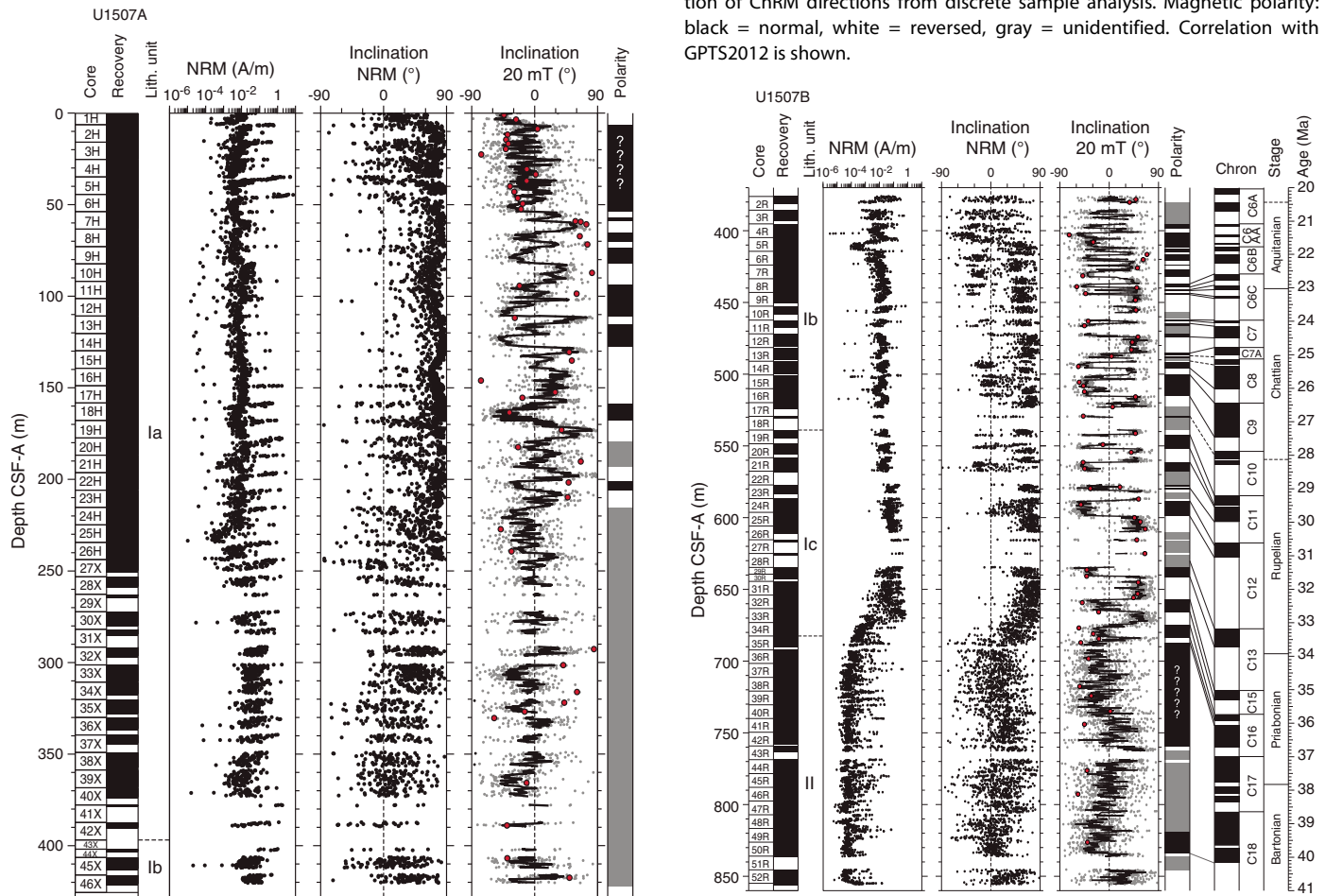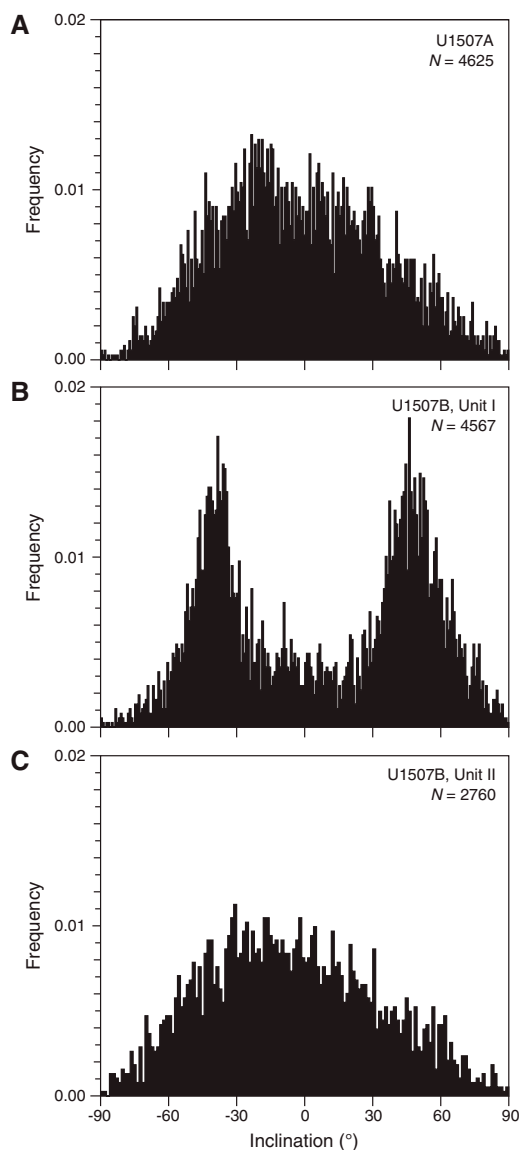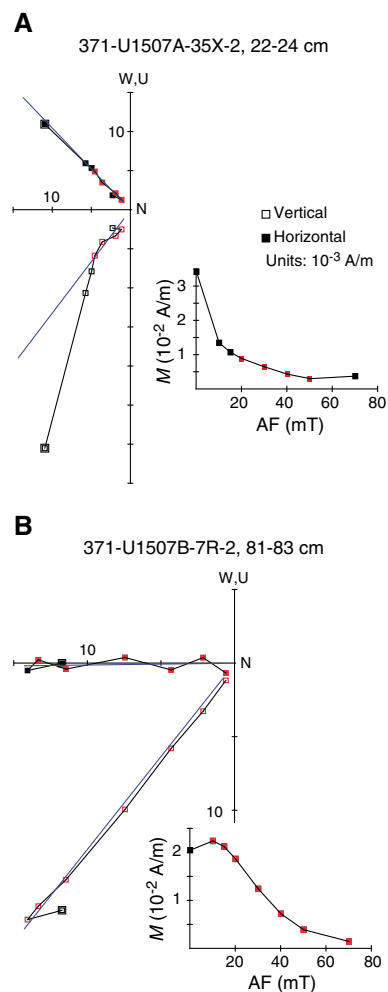
Figure F26. Inclination values after 20 mT AF demagnetization from pass-through paleomagnetic data. N = number of data points. A. Hole U1507A. B. Unit I in Hole U1507B (0–682 m). C. Unit II in Hole U1507B (682–855 m). N = number of data points.

Figure F27. Vector endpoint demagnetization diagrams (Zijderveld, 1967) and AF demagnetization behavior for two representative discrete samples, Site U1507. Open squares = projections onto vertical plane, solid squares = projections onto horizontal plane, blue lines = components fitted using selected data points (red squares) by PCA (Kirschvink, 1980).

clear bimodal clustering. However, two switches from negative to positive inclination in Cores 43R (759.3 m) and 50R (834.0 m) are tentatively used for magnetostratigraphic correlation (see below). The higher NRM intensity in Subunits Ib and Ic presumably comes from the greater abundance of ferromagnetic (sensu lato) minerals associated with ash layers and volcaniclastic turbidites (see **Lithostratigraphy**).

After principal component analysis (PCA) of the demagnetization diagrams, linear characteristic remanent magnetization (ChRM) components of the NRM were isolated from 21 out of 57 (37%) discrete samples from Hole U1507A (Figure **F27**), which is not sufficient to support a reliable magnetostratigraphic interpretation. In Hole U1507B, 59 of 72 (82%) discrete samples show excellent AF demagnetization behavior with linear ChRM directions pointing toward the origin of the demagnetization diagrams after AF demagnetization at 10–20 mT. The good paleomagnetic behav-

ior of discrete samples confirms the reliability of pass-through paleomagnetic results from Unit I in Hole U1507B.

Anisotropy of magnetic susceptibility

AMS was measured on all 123 discrete samples from Site U1507 (Figure **F28**). Samples from Hole U1507A were mostly collected with 7 cm³ plastic cubes pushed into soft-sediment cores, which resulted in a generally poorly defined orientation of the AMS tensor. However, the κ_{min} axis of the AMS ellipsoid is statistically oriented roughly perpendicular to the horizontal plane. Samples from Hole U1507B were trimmed into cubes directly from the hard sediment, allowing precise orientation. AMS results for samples from Hole U1507B show a clear oblate magnetic fabric, with the minimum axis of the AMS ellipsoids well clustered and perpendicular to the bedding, typical of undeformed sedimentary rocks.

Magnetostratigraphy

No reliable shipboard magnetostratigraphy was obtained for Hole U1507A, but for Cores 371-U1507B-8R through 34R (433–683 m), integration with biostratigraphic results (see **Biostratigraphy**

and **paleoenvironment**) allows a reliable correlation of measured polarity with known polarity chrons of the geomagnetic polarity timescale (GPTS). All chrons from Chron C6Br in the early Miocene to Chron C16n in the late Eocene were detected (Figure **F25**). Despite the high noise level in the remanence data, integration with

biostratigraphy also allows interpretation of the two switches from normal to reversed polarity observed in Cores 43R (759.3 m) and 50R (834.0 m). These reversals correlate with the bases of Chrons 17n and C18n, respectively, and reinforce the age model for the lowermost depths at Site U1507 (Table **T8**).

Figure F28. AMS data for discrete samples from (A) Hole U1507A and (B) Hole U1507B. Left: stereoscopic plots. Blue squares = κ_{max} axes, green triangles = κ_{int} axes, purple circles = κ_{min} axes. Mean directions of κ_{max} (open square), κ_{int} (open triangle), and κ_{min} (open circle) axes, shown along with their 95% confidence ellipses. N = number of samples. Right: corresponding lineation ($\kappa_{max}/\kappa_{int}$) vs. foliation ($\kappa_{int}/\kappa_{min}$) data from each hole.
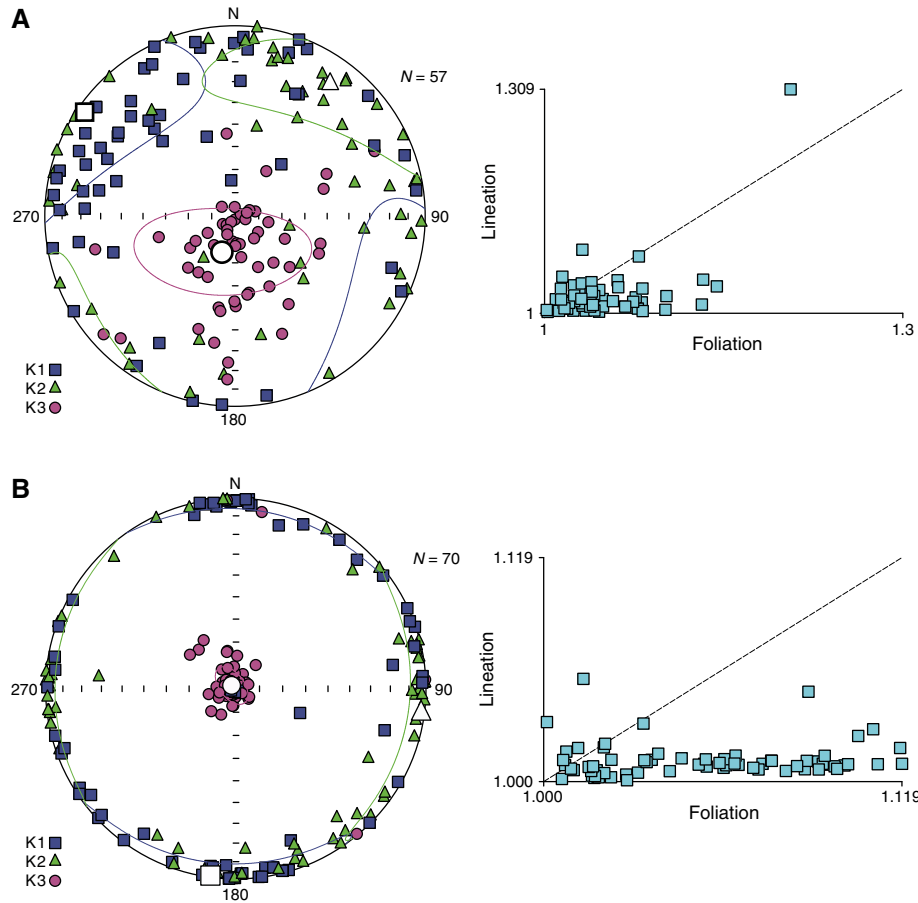
Table T8. Magnetostratigraphic tie points, Site U1507. **Download table in CSV format.**

Chron boundary	Top core, section, interval (cm)	Bottom core, section, interval (cm)	Age (Ma)	Top depth CSF-A (m)	Bottom depth CSF-A (m)	Midpoint depth CSF-A (m)
	371-U1507B-	371-U1507B-				
C6Br/C6Cn.1n	8R-3, 115	8R-3, 125	22.564	437.05	437.15	437.100
C6Cn.1n/C6Cn.1r	8R-5, 55	8R-5, 65	22.754	439.30	439.40	439.350
C6Cn.1r/C6Cn.2n	8R-6, 100	8R-6, 125	22.902	441.00	441.25	441.125
C6Cn.2n/C6Cn.2r	8R-7, 20	8R-7, 25	23.030	441.70	441.75	441.725
C6Cn.2r/C6Cn.3n	9R-1, 70	9R-1, 75	23.233	443.60	443.65	443.625
C6Cn.3n/C6Cr	9R-2, 15	9R-2, 20	23.295	444.55	444.60	444.575
C6Cr/C7n.1n	11R-1, 0	11R-1, 10	23.962	462.10	462.20	462.150
C7n.1n/C7n.1r	11R-1, 70	11R-1, 80	24.000	462.80	462.90	462.850
C7n.1r/C7n.2n	11R-2, 105	11R-3, 0	24.109	464.62	464.78	464.700
C7n.2n/C7r	12R-2, 75	12R-2, 80	24.474	473.85	473.90	473.875
C7r/C7An	13R-3, 125	13R-4, 20	24.761	485.34	485.71	485.525
C8n.2n/C8r	14R-4, 65	14R-4, 80	25.987	495.66	495.81	495.735
C8r/C9n	15R-1, 20	15R-1, 45	26.420	500.60	500.85	500.725
C9n/C9r	16R-4, 105	16R-4, 110	27.439	515.43	515.48	515.455
C10r/C11n.1n	19R-3, 25	19R-3, 30	29.183	542.05	542.10	542.075
C11n.1n/C11n.1r	20R-3, 35	20R-3, 40	29.477	551.73	551.78	551.755
C11n.1r/C11n.2n	21R-3, 55	21R-3, 65	29.527	561.34	561.44	561.390
C11n.2n/C11n	23R-1, 5	21R-4, 10	29.970	577.05	581.03	579.040
C11r/C12n	24R-2, 35	24R-2, 50	30.591	588.24	588.39	588.315
C12n/C12r	25R-2, 120	25R-3, 10	31.034	598.74	598.88	598.810
C12r/C13n	28R-1, 17–19	29R-2, 68–70	33.157	625.05	636.36	630.705
C13n/C13r	30R-2, 30	30R-2, 35	33.705	640.83	640.88	640.855
C13r/C15n	32R-3, 60	32R-3, 65	34.999	657.08	657.13	657.105
C15n/C15r	33R-2, 10	33R-2, 15	35.294	664.77	664.82	664.795
C15r/C16n.1n	34R-2, 35	34R-3, 55	35.706	674.72	676.40	675.560
C16n.1n/C16n.1r	35R-1, 40	35R-1, 85	35.892	682.80	683.25	683.025
C16n.1r/C16n.2n	35R-2, 45	35R-3, 140	36.051	684.37	686.32	685.345
C18n.2n/C18r	50R-6, 110	50R-7, 30	40.145	833.95	834.47	834.210

Petrophysics

The full suite of physical properties measurements were made on cores recovered from Holes U1507A and U1507B (see **Petrophysics** in the Expedition 371 methods chapter [Sutherland et al., 2019a]). Downhole temperature measurements were made in Hole U1507A during drilling, and wireline logging was completed using a modified triple combo tool in Hole U1507B (see **Operations**). Measurable variations in physical properties arise from increasing lithification and from variations in sediment composition, including clay, volcaniclastics, foraminiferal ooze, and limestone.

Although rather uniform in their properties, data from lithostratigraphic Subunit Ia show small variations in magnetic susceptibility, NGR, P-wave velocity, and density (Figures **F29**, **F30**, **F31**). High magnetic susceptibility and NGR values correlate with tuffaceous and volcaniclastic layers. The overall higher P-wave velocity, greater density, and color change in the lower part of the subunit (300–400 m) are attributed to the diagenetic change of ooze to chalk and to an increase in clay content. Significant variations in physical properties were also observed in Subunits Ib and Ic, except in color, which remains approximately constant. High magnetic susceptibility and NGR values correlate with increased volcaniclastic content, and NGR peaks also occur where higher clay content is identified. In these subunits, P-wave velocity and bulk density correlate, reflecting changes in clay, chalk, and volcaniclastic content. Physical properties change little with depth in the homogeneous chalk and limestone of Unit II.

Density and porosity

Bulk density was estimated using the gamma ray attenuation (GRA) method on whole-round sections, the moisture and density (MAD) method on discrete samples from section halves, and the Hostile Environment Litho-Density Sonde (HLDS) wireline logging tool, which also uses the GRA method and is referred to as RHOM (Figures **F29**, **F30**).

Bulk density values show significant variations throughout the sedimentary column that correlate with porosity and grain density variations (Figure **F29**). Bulk density increases with depth in Subunit Ia (0–401 m; Cores 371-U1507A-1H through 46X and 371-U1507B-2R through 4R) from 1.5 to 2.1 g/cm^3, presumably in response to a decrease in porosity, given that the material has similar grain density. GRA bulk density values are ~6% higher in the upper half of Subunit Ia (to about 250 m) than MAD and RHOM values, a difference attributed to the GRA calibration method that is biased toward siliciclastic material. In the upper part of Subunit Ib (~401–490 m), bulk density decreases from ~2.1 to ~1.7 g/cm^3 and porosity values show a significant increase to 70%. This pronounced change measured on cores is also clearly evident in the in situ RHOM bulk density and resistivity (a proxy for porosity). Bulk density increases from ~1.7 to 2.2 g/cm^3 and porosity decreases from 70% to 30% in the lower part of Subunit Ib between 490 and 543 m. In Subunit Ic (~543–685 m) and Unit II (685–856 m), the bulk density downhole trend is approximately constant with local variations between ~2.0 and 2.3 g/cm^3. Throughout Unit I, bulk density values decrease by ~0.1 g/cm^3 in layers of foraminiferal ooze (e.g., Section 371-U1507A-16H-3).

In Unit II below 685 m, bulk density is approximately constant at ~2.2–2.3 g/cm^3 (RHOM) and ~2.0–2.2 g/cm^3 (MAD).

Grain density values (Figure **F29**) are approximately constant in Subunit Ia, with an average value of 2.71 ± 0.03 g/cm^3 typical of carbonates. Higher variance in grain density values was observed between 300 and 400 m. In Subunit Ib, grain density decreases from

Figure F29. Bulk density, grain density, porosity, and *P*-wave velocity. Large dots = MAD and PWC results, black lines = wireline logging bulk density and *P*-wave velocity, small dots = whole-round section GRA density and *P*-wave velocity (PWL) (pink = Hole U1507A, orange = Hole U1507B). Red horizontal line = change from APC to XCB drilling in Hole U1507A. Black horizontal line = lithostratigraphic unit boundary, dashed horizontal lines = subunit boundaries. For porosity, best-fitting exponential decay curve (line) is shown (see text for details). WMSF scale is for logging results; CSF-A scale is for core results.
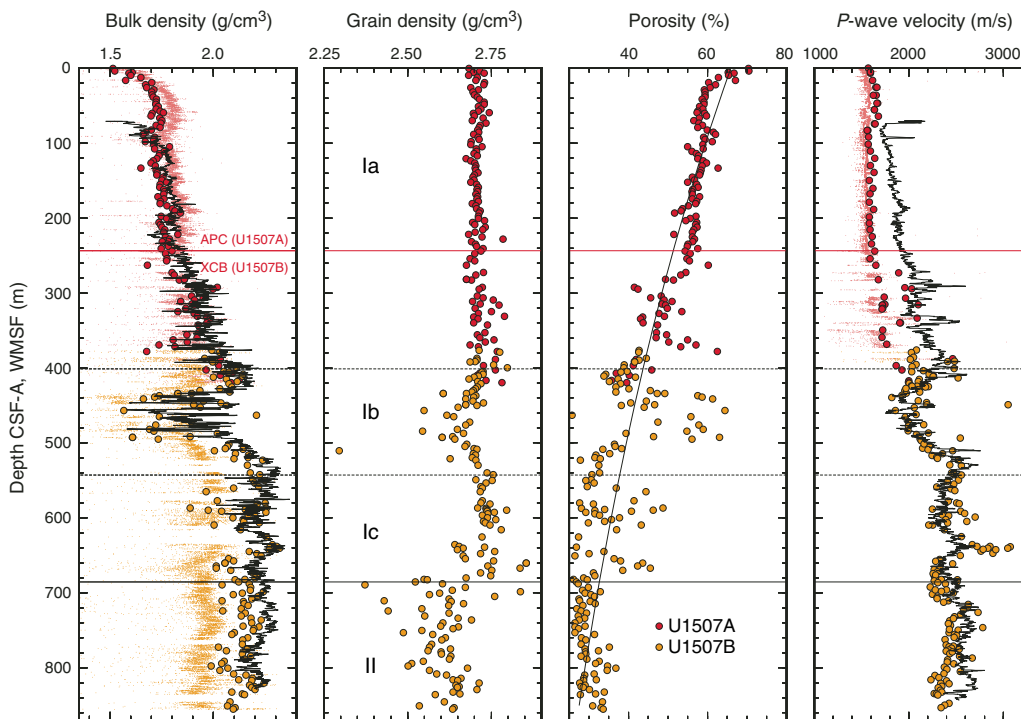
~2.7 to ~2.6 g/cm³ in clayey nannofossil chalk with ash. In Subunit Ic, which has abundant volcaniclastic deposits, grain density averages ~2.75 g/cm³. Grain density in Unit II (clayey nannofossil chalk) varies between ~2.5 and 2.7 g/cm³.

MAD-derived porosity values decrease with depth from about 70% in nannofossil ooze at the top of Hole U1507A to about 25% at the base of Hole U1507B in Eocene nannofossil chalk (Figure **F29**). Porosity decreases by 10% in the top 30 m of pelagic ooze and then another 10% by 280 m in Hole U1507A through the gravity flows (see **Lithostratigraphy**). The rate of porosity decrease with depth is higher below 280 m than it is above, a change associated with lithification of the calcareous sediments to chalk. In Subunits Ib and Ic, porosity spikes of ~50%–70% and ~40%–50%, respectively, are well above the baselines of ~40% and 35%, respectively. Porosity remains approximately constant with depth at ~35% in Unit II (686–856 m).

A best-fitting curve of porosity (ϕ) decrease with depth (z) (i.e., $\phi = \phi_o e^{-z/c}$) has $\phi_o = 66\% \pm 1\%$ and $c = 975 \pm 32$ m (Figure **F29**). In the upper portion of Subunit Ia, from the seafloor to about 30 m, the decrease is much faster than predicted by the best fit. A more important deviation between the single model and the data is evident near the Unit I/II boundary: both the downhole trend and the variance in porosity differs significantly in the two units, and applying separate model coefficients may be appropriate.

P-wave velocity

P-wave velocity was measured on whole-round sections (*P*-wave logger [PWL]), on working-half sections (*P*-wave caliper [PWC] and *P*-wave bayonet [PWB]), and with the Dipole Sonic Imager (DSI-2) wireline logging tool (Figures **F29**, **F30**). In Hole U1507B, PWL measurements were made on Cores 371-U1507B-2R and 3R (376–392 m) only because gaps between RCB cores and core liner

made results unreliable elsewhere. From ~390 m downhole, the frequency of discrete PWC measurements was increased to a minimum of three per core because this method provided good results.

P-wave velocity in Subunit Ia of Hole U1507A gradually increases with depth from ~1600 m/s at the seafloor to 1670 m/s at 280 m, an interval where sediments are predominantly nannofossil ooze. PWC velocity values over this depth range lie on the maximum of the PWL values. DSI-2 in situ velocity values are consistently higher than PWC and PWL values obtained from the cores, with the discrepancy increasing with depth from ~200 m/s at 80 m to ~400 m/s at 280 m. The laboratory-measured values are lower than the downhole values, which is attributed to porosity rebound (see **Petrophysics** in the Expedition 371 methods chapter [Sutherland et al., 2019a]) that affects the largely unconsolidated ooze after recovery (Figure **F29**).

A gradual change in the physical properties is associated with the diagenetic change from ooze to chalk between 284 and 293 m (see **Lithostratigraphy**). *P*-wave velocity (PWC and PWL) in the chalk of Core 371-U1507A-32X ranges between 1720 and 2100 m/s, an increase of ~100–400 m/s compared with the ooze in overlying Core 31X. DSI-2 velocity values are also higher in this depth range. From this ooze–chalk transition to ~400 m (base of Subunit Ia), *P*-wave velocity values are ~2000 m/s. The misfit between DSI-2 and PWL/PWC correlates with a reduction in porosity at the base of the subunit, indicating diminishing porosity rebound in the lower, more lithified sediments (Figure **F29**).

From the top of Subunit Ib (401 m) to ~800 m, PWC and DSI-2 velocity values agree well and are high and show gradients. A velocity increase from 2000 to 2500 m/s between 440 and 530 m occurs in the clayey nannofossil chalk (see **Lithostratigraphy**). In Subunit Ic and Unit II (543–856 m), the velocity trend and local variations

Figure F30. Wireline logging data for hole size, gamma ray, density, resistivity, *P*-wave velocity, and *S*-wave velocity, Hole U1507B. HSGR = total spectral gamma ray, HNGS = Hostile Environment Natural Gamma Ray Sonde. mbsf = meters below seafloor.
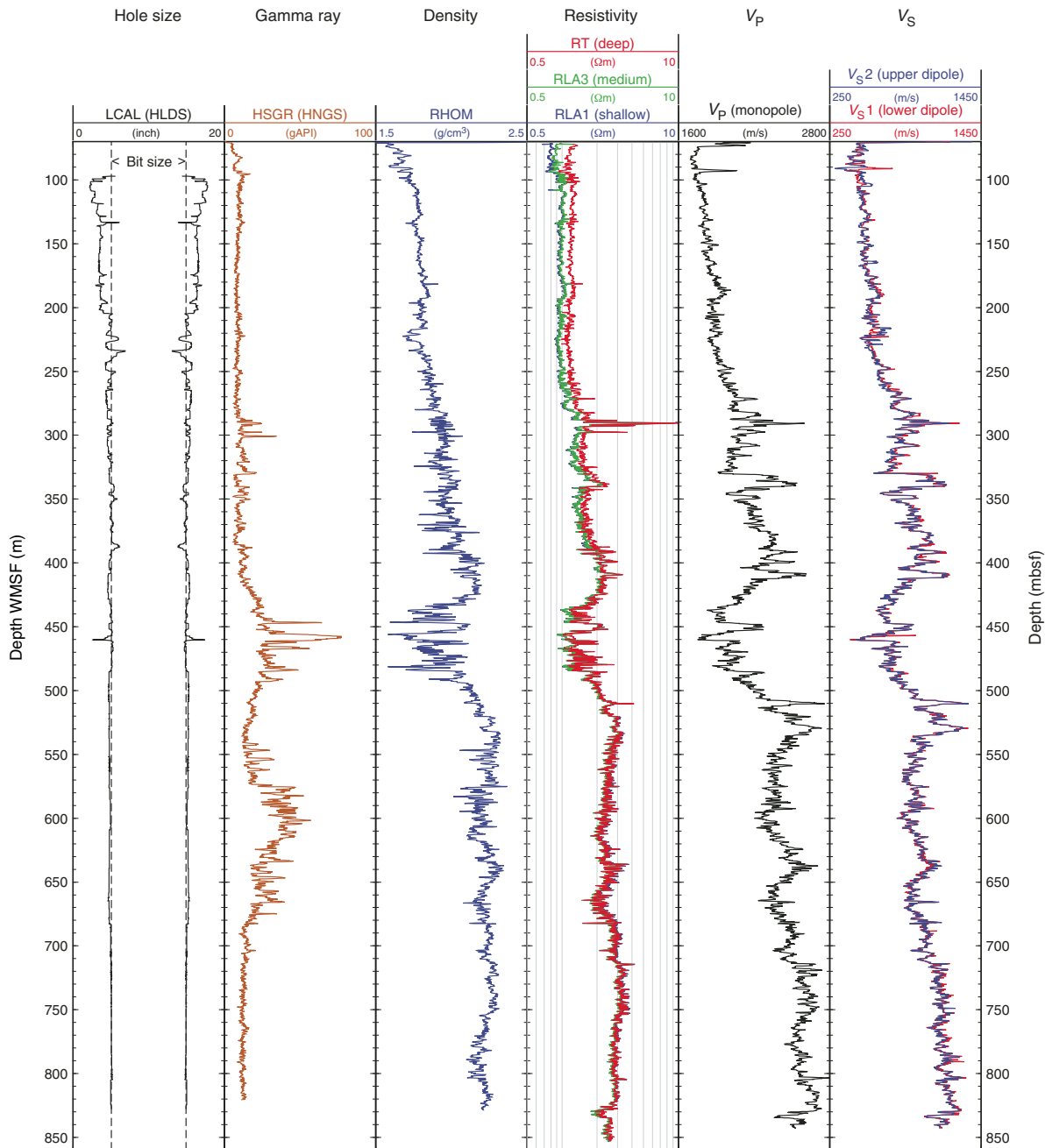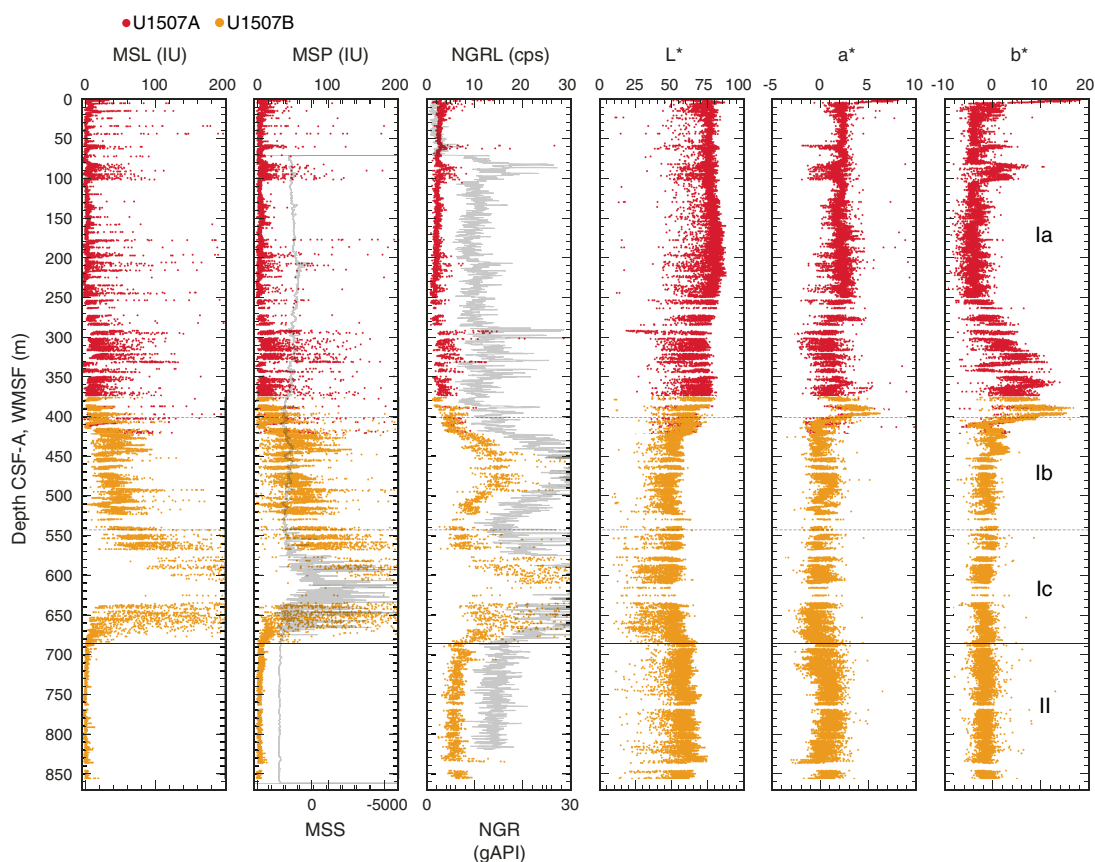

mimic those of bulk density. Velocity averages ~2400 m/s throughout the interval, with local variations from 2200 to 3000 m/s. The highest values of ~3000 m/s are measured in Cores 371-U1507B-29R through 31R (639–649 m) in layers of clayey nannofossil chalk with volcanic ash that are interbedded with tuffaceous conglomerate up to 50 cm thick (e.g., Sample 29R-1, 15 cm; 634.9–635.4 m). A smaller increase to 2600 m/s is indicated by the DSI-2 velocity values at this depth.

DSI-2 *P*-wave velocity values are ~100–300 m/s higher than PWC values in the lowermost ~120 m of the hole. A negative excursion to ~2400 m/s at ~835 m wireline log matched depth below seafloor (WMSF) is associated with the MECO (see **Biostratigraphy and paleoenvironment**).

Magnetic susceptibility

Magnetic susceptibility was measured with the pass-through system (loop magnetic susceptibility [MSL]) on all whole-round sections, the point measurement system (point magnetic susceptibility [MSP]) on all section halves, and the magnetic susceptibility sonde (MSS) wireline logging tool (dual-coil sensor) (Figure **F31**). MSL and MSP values generally agree and are in accord with MSS variations. Magnetic susceptibility is low (~0–5 instrument units [IU]) in Subunit Ia, with many local spikes (up to 100 IU) correlated with volcanic ash layers (e.g., Section 371-U1507A-23H-3). Values in Subunit Ib range between ~5 and ~80 IU. Magnetic susceptibility values are higher (~100 to ~2000 IU) in Subunit Ic, where abundant

Figure F31. Magnetic susceptibility (MSL and MSP), NGR, and L*, a*, b*, Site U1507. Black lines = wireline logging measurements of magnetic susceptibility and NGR (scales at bottom). Horizontal line = lithostratigraphic unit boundary, dashed horizontal lines = subunit boundaries. WMSF scale is for logging results; CSF-A scale is for core results.

Natural gamma radiation

NGR was measured on all whole-round sections using the Natural Gamma Radiation Logger (NGRL) and in situ through most of Hole U1507B using the wireline logging Hostile Environment Natural Gamma Ray Sonde (HNGS) (Figures F31, F32). Variations observed in core measurements closely match those in the wireline log (see Stratigraphic correlation). NGRL values are between ~2 and ~5 counts/s (10–15 gAPI in the hole) throughout Subunit Ia, except in four thin zones (10–30 cm thick) that have values of 10–20 counts/s (60, 100, 300, and 340 m). These zones correspond to nannofossil-rich clay layers (see Lithostratigraphy). NGRL values increase with depth from ~2 to ~20 counts/s in the upper 50 m of Subunit Ib (Cores 371-U1507B-4R through 16R; 400–550 m). Values decrease again to ~8 counts/s at the base of Subunit Ib (~550 m). In Subunit Ic, values increase to ~40 counts/s at ~600 m and then decrease again to ~8 counts/s at the base of Unit I. The source of the hundreds of NGR peaks, which make up two conspicuous rises in NGR in Subunits Ib and Ic over intervals of ~100 m, are the many volcaniclastic layers interbedded in clayey nannofossil chalk in these units (see Lithostratigraphy). In Unit II, composed mostly of homogeneous clayey nannofossil chalk and limestone, NGR values remain low (~7 counts/s) and approximately constant with depth.

volcaniclastic layers occur in clayey nannofossil chalk (see Lithostratigraphy). Values are consistently very low (~0–5 IU) throughout the clayey nannofossil chalk in Unit II.

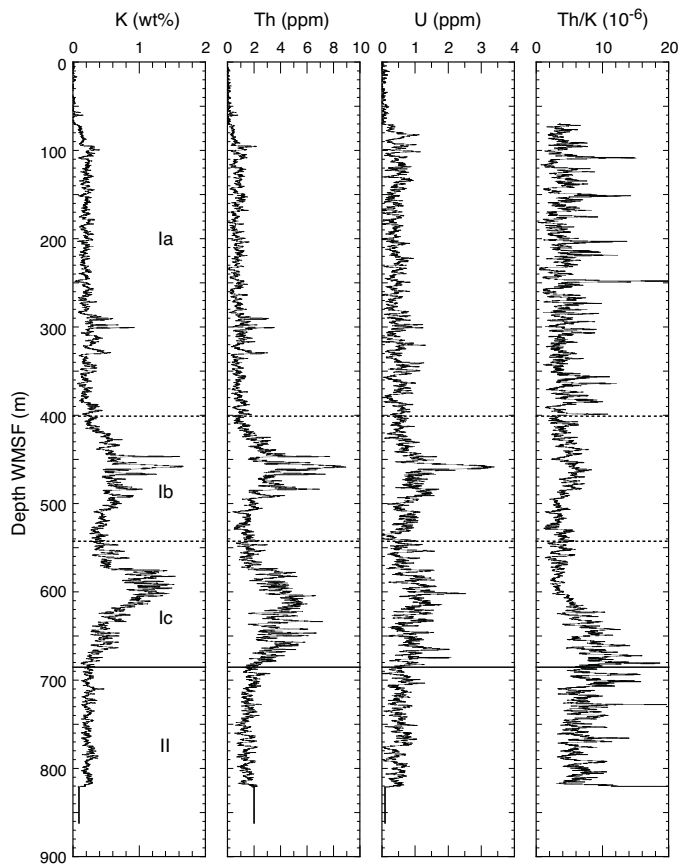Potassium, thorium, and uranium contents were computed from the wireline logging data (HNGS; Figure F32). In Subunit Ia and Unit II, potassium, thorium, and uranium are at the detection limit. In Subunit Ib, potassium contents are higher (0.6 wt%), with spikes of 1.85 wt%. Thorium and uranium contents increase to 3 and 1 ppm, respectively, in Subunit Ib, with spikes of 9 and 3 ppm, respectively. Potassium and thorium contents are higher in Subunit Ic, up to 1.5 wt% and 6 ppm, respectively. The thorium to potassium ratio shows a higher baseline in the lower half of Subunit Ic and in Unit II because the abundance of potassium decreases.

Thermal conductivity and temperature

Conductivity measurements were made in each core on the dominant lithology. Thermal conductivity increases with depth from 1.1 to 1.8 W/(m·K) over the upper ~420 m. In Subunit Ib and at the top of Subunit Ic, conductivity is variable. Values decrease to ~1.4 W/(m·K) at 460 m, increase to ~2.0 W/(m·K) at 550 m, and decrease to 1.3 W/(m·K) at 620 m. Below 620 m, thermal conductivity is approximately constant or decreases slightly in the lower part of Subunit Ic and in Unit II. The general trends in the conductivity data bear a close resemblance to the porosity profile (Figure F29), indicating that porosity is likely the main control on thermal conductivity variations.

In Hole U1507A, in situ temperature was measured with the advanced piston corer temperature tool (APCT-3) at six depths just after cutting Cores 4H, 7H, 10H, 13H, 16H, and 19H (30–190 m). The time-temperature records from Cores 4H, 16H, and 19H are

Figure F32. K, Th, and U contents and Th to K ratio computed from HNGS tool data, Hole U1507B. Horizontal line = lithostratigraphic unit boundary, dashed horizontal lines = subunit boundaries.

Sediment strength

Sediment strength was measured with both the automated vane shear and penetrometer and generally increases with depth (Figure **F34**). Vane shear strength linearly increases from ~18 kPa near the seafloor to ~50 kPa at ~250 m. Compressive strength increases from 0 kPa near the seafloor to ~80 kPa at ~75 m. Strength increases but becomes more variable, ranging between ~50 and ~300 kPa, to ~250 m, where sediments are too hard to penetrate with the tool.

Color spectrophotometry

In the upper part of Subunit Ia (0–280 m), reflectance L*, a*, and b* values are constant around ~75, ~2, and approximately −2, respectively (Figure **F31**), except for some peaks and troughs at ~60 and 80–100 m. The lithology in this depth range is gray/white nannofossil ooze. At ~280–400 m, the dominant lithology changes to nannofossil chalk and L* (~55) and a* (~1) values are lower, whereas b* values increase with depth in this interval to ~10. These changes indicate an increase in green (vs. red) and yellow (vs. blue). In Subunits Ib and Ic and Unit II, a* and b* values are constant at ~1 and approximately −1, respectively. L* values are constant at ~40 in Subunits Ib and Ic and increase to 60 in Unit II. The increase in L* is attributed to the downhole disappearance of ash in clayey nannofossil chalk in Unit II.

Two-way traveltime to depth conversion

Using a combination of *P*-wave velocity and bulk density data obtained from core and in situ measurements, acoustic impedance and a synthetic trace were computed. Corrections for the change in velocity and density arising from porosity rebound (Urmos and Wilkens, 1993) under atmospheric conditions are applied to core data values (Figure **F35A, F35C**; also see **Petrophysics** in the Expedition 371 methods chapter [Sutherland et al., 2019a]). The synthetic trace was compared with a trace extracted from multichannel seismic (MCS) data (Line TAN1409-NCTN-11, common depth point [CDP] 4020, black line) recorded at Site U1507. Where prominent reflections on the seismic trace and the synthetic trace are well correlated, two-way traveltime (TWT) depth points were selected (Figure **F35B**; Table **T9**). Reflectors A–F are well fit by the synthetic seismogram, with some variability in the fit to the amplitude of these reflections. The fit is poorer for the two deepest reflectors (G and H); the synthetic solution is of higher frequency than the seismic data, and the synthetic arrival times are ~0.005 s early, or ~1/4 wavelength ahead. Higher attenuation of the MCS data, compared with the synthetic model, or an overestimation of velocity values may account for the discrepancy below 700 m WMSF.

good quality with little deviation from a single heat impulse. All other values are fair quality and yield ambient temperatures with errors <1°C. Temperature increases below the seafloor with a gradient of 49.2 ± 2.0°C/km (Figure **F33A**). Thermal conductivity was measured on cores from the same depth interval and increases linearly with depth (Figure **F33B**). Because thermal conductivity is not constant with depth, the Bullard method was used to estimate heat flux (see **Petrophysics** in the Expedition 371 methods chapter [Sutherland et al., 2019a]; Figure **F33C**). The constant slope between thermal resistance with temperature is consistent with a thermal regime that is close to a conductive state. From the plot of temperature with thermal resistance, we estimate the heat flux to be 66.6 ± 2.7 mW/m² from the slope and the temperature at the seafloor to be 2.5 ± 0.3°C from the intercept. The heat flux is in line with the tectonics of the region (Pollack et al., 1993).

Figure F33. Heat flow. Note the vertical scale unit changes. A. APCT-3 temperature with depth profile, Hole U1507A. B. Thermal conductivity with 95% confidence interval estimate with three repeat measurements shown as error bars, Hole U1507A cores. C. Bullard plot (see Petrophysics in the Expedition 371 methods chapter [Sutherland et al., 2019a]) showing thermal resistance (Ω) vs. measured temperature. D. Thermal conductivity with error bars as in B, Hole U1507A (red) and U1507B (orange) cores.
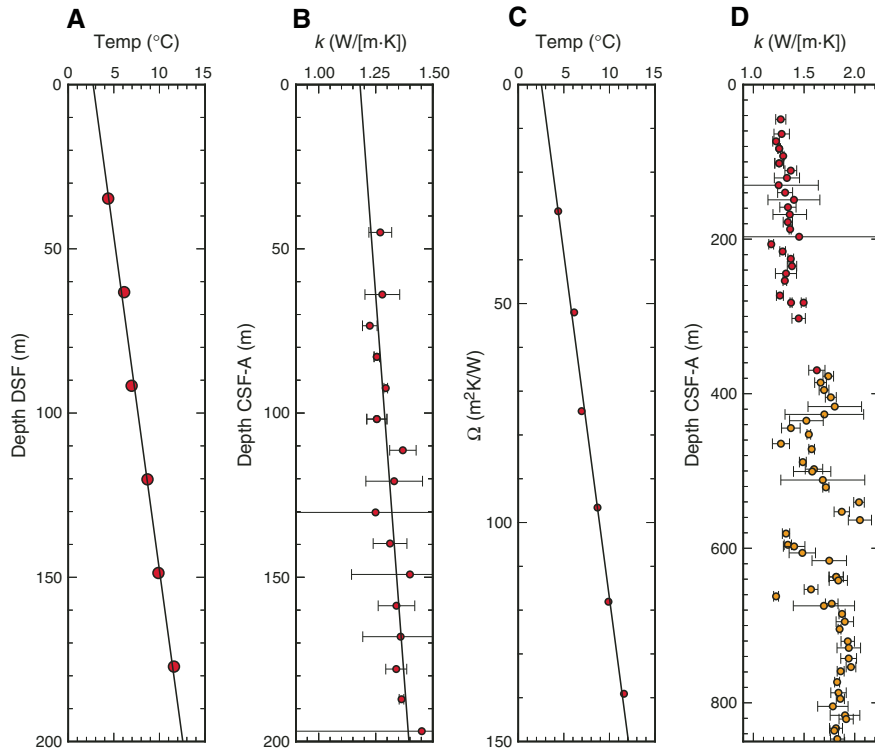
Figure F34. Strength, Site U1507. A. Shear strength measured by automated vane shear. B. Compressive strength measured using pocket and needle penetrometers.
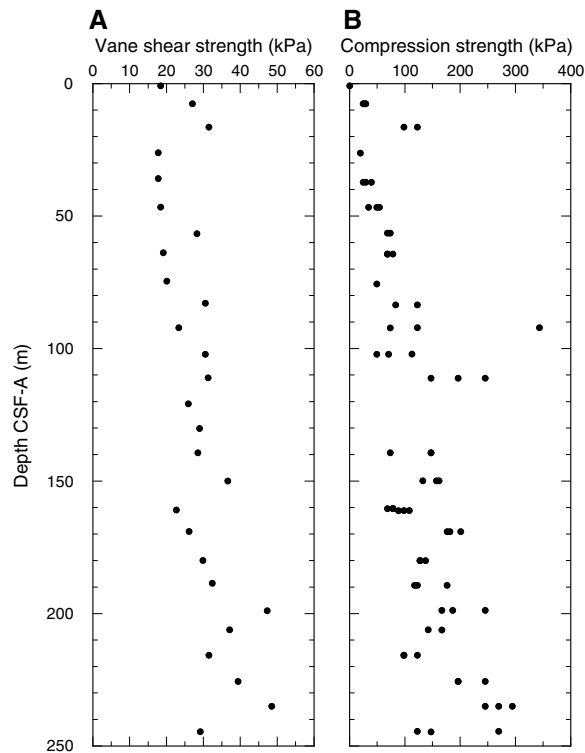
Figure F35. Borehole data to MCS data tie, Site U1507. A. Impedance calculated from combined rebound-corrected velocity data from cores and wireline log *P*-wave velocity and density data vs. TWT. Horizontal line = lithostratigraphic unit boundary, dashed horizontal lines = subunit boundaries. B. TWT calculated from depths below seafloor, rebound-corrected PWC *P*-wave velocity data (0–70 m), and in situ wireline log *P*-wave velocity (70–860 m WMSF). Numerical solution for TWT (*t*) with depth (*z*) is given by $z = 306.57t^2 - 823.43t$. Circles = positions of strong reflectors shown in C and D (red = strongly correlated, open = not correlated), dashed lines = fit between seismic survey data in D and synthetic trace in C. C. Synthetic trace (red) and MCS trace data at Line TAN1409-NCTN-11, CDP 4020 (black). Seismic Reflectors A–H and seafloor (SF) are labeled. D. MCS data.
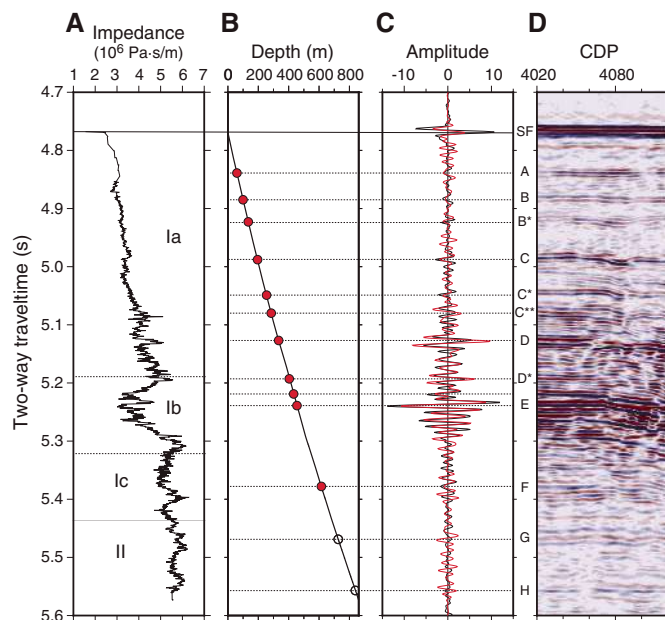

Table T9. Seismic reflectors, two-way traveltimes (TWT), and depths for reflectors identified on multichannel seismic data, Site U1507. Major seismic reflector depths are estimated from synthetic modeling of borehole physical properties (see text and Expedition 371 methods chapter [Sutherland et al., 2019a]). Reflectors are shown on Figure F35. **Download table in CSV format.**

Seismic reflector	TWT (s)	TWT below seafloor (s)	Total depth (m)	Depth below seafloor (m)
SF	4.769	0	3584	0
A	4.839	0.07	3643	59
B	4.885	0.116	3684	100
B*	4.923	0.154	3718	134
C	4.988	0.219	3779	195
C*	5.049	0.28	3839	255
C**	5.08	0.311	3870	286
D	5.127	0.358	3918	334
D*	5.193	0.424	3988	404
D**	5.219	0.45	4017	433
E	5.239	0.47	4039	455
F	5.378	0.609	4199	615
G	5.469	0.7	4311	727
H	5.557	0.788	4423	839

Geochemistry

The geochemistry program at Site U1507 was designed to characterize the composition of pore water and solid sediment and to assess the potential presence of volatile hydrocarbons. Site U1507 was expected to have a relatively thick sediment column adjacent to the submerged Norfolk Ridge in relatively deep water. Low primary productivity in overlying surface water and limited terrigenous input might lead to a carbonate-rich lithology lean in organic components (see **Background and objectives**). Furthermore, reactions with the volcanic sedimentary components might influence pore water chemistry.

Headspace hydrocarbon gases

A total of 97 headspace gas samples were taken for routine safety monitoring, typically one from the top of the last section of every core. Hydrocarbon gases were consistently below the detection limit.

Interstitial water analyses

A total of 56 interstitial water (IW) samples were collected and analyzed, 51 from Hole U1507A and 5 from Hole U1507B. One mudline sample was taken from the top of Core 371-U1507A-1R. The deepest IW samples were at 411 m in Hole U1507A and 497 m in Hole U1507B. The bottom ~370 m of the sequence was not sampled because the sediment was too hard to squeeze. Below 243 m, XCB cores were retrieved instead of APC cores, which may explain some of the chemistry results at depth, in particular significantly different concentrations for dissolved species in adjacent samples. Results from both holes are displayed together but distinguished for discussion. The general elemental and ion concentration profiles show some similarity to those of Site U1506.

Salinity, pH, and alkalinity

Salinity is 35.5 in the mudline sample and increases to 37.0 at 15 m (Table **T10**; Figure **F36**). Below this depth, salinity decreases to 34.5 at 167 m and then increases downhole to as high as 36.0 with fluctuations. Salinity at this site displays more variation than at Site U1506, where it is constant at 35.5. Alkalinity at Site U1507 increases from 2.6 mM in the mudline sample to 3.5 mM at 36 m and then decreases gradually to 0.4 mM at 411 m. Alkalinity at this site has a wider concentration range than at Site U1506. The upper part of the pH profile at this site is similar to that at Site U1506, decreasing from 7.74 in the mudline sample to 7.47 at 233 m. Unlike Site U1506, pH increases below 233 m to as high as 8.14 at 295 m. The high pH value at this depth signals a change in lithology from nannofossil ooze to chalk with volcanic ash (see Figure **F4**).

Sulfate and ammonium

Sulfate (SO_4^{2-}) and ammonium (NH_4^+) profiles generally change in the opposite direction of each other (Table **T10**; Figure **F36**). Sulfate decreases from 28.4 mM in the mudline sample to 17.3 mM at

Table T10. Interstitial water chemistry, Site U1507. **Download table in CSV format.**

Figure F36. Salinity, alkalinity, pH, and major, minor, and trace element concentrations in IW samples in uppermost 497 m, Site U1507.
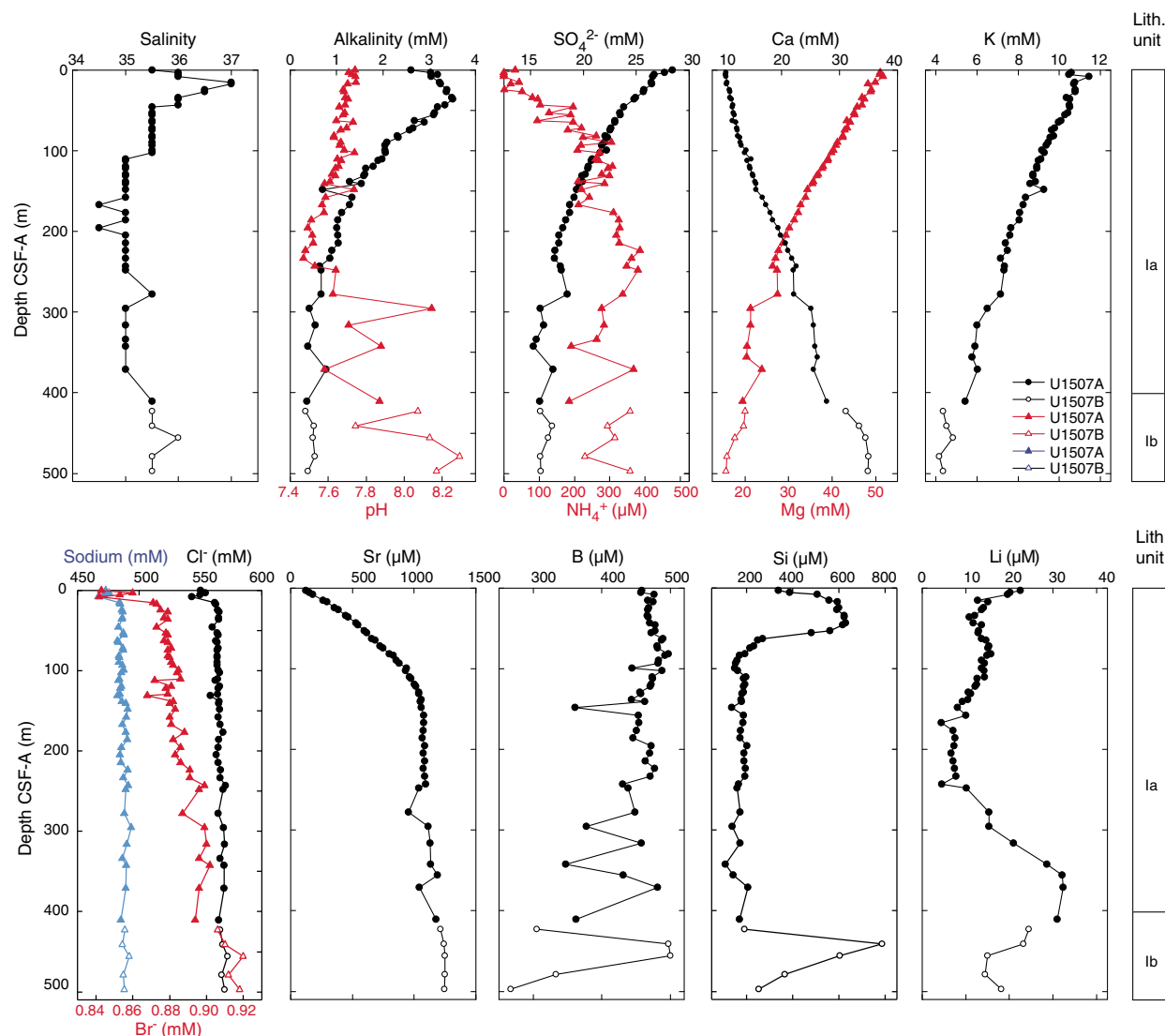
233 m and then decreases downhole gradually with fluctuations to a minimum value of 15.3 mM at 342 m. The concave-down SO_4^{2-} profile mimics that at Site U1506 but has a lower minimum value.

The dissolved NH_4^+ profile shows more detail and a broader range than at Site U1506 (Table **T10**; Figure **F36**). NH_4^+ concentration is 32.4 µM in the mudline sample but is otherwise below the detection limit in the uppermost 5 m. Below this depth, it increases slightly to values <50 µM from 5 to 24 m. Such low values of NH_4^+ in the uppermost sediment suggest consumption below the seafloor by microbial oxidation (e.g., Bolliger et al., 1991). NH_4^+ concentration increases downhole to a maximum value of 385.9 µM at 224 m, more than twice as high as at Site U1506. This maximum value supports the interpretation of greater organic matter oxidation at Site U1507.

Calcium, magnesium, and potassium

The dissolved calcium (Ca) and magnesium (Mg) concentration profiles generally mirror each other downhole with smooth trends in the upper 243 m (Table **T10**; Figure **F36**). Ca concentration increases from 10.4 mM at 3 m to 34.9 mM at 497 m, whereas Mg concentration decreases from 51.1 to 15.7 mM in the same interval.

The coupled change in Ca and Mg may reflect reactions of the pore water with volcanic ash dispersed in the sediment column, which is abundant in Subunits Ib and Ic (see **Lithostratigraphy**). Potassium (K) concentration shows a decreasing trend from 10.5 mM at 3 m to 4.6 mM at 497 m with small fluctuations below 243 m (Table **T10**; Figure **F36**). The continuous decrease in K with depth may result from ion exchange with clay minerals in the sediment, which are abundant below 295 m (see **Lithostratigraphy**).

Chloride, bromide, and sodium

The Cl^-, Br^-, and Na concentration profiles are similar downhole. All three show slight fluctuations in the uppermost 8 m, a sharp increase at 15 m, and a gradual increase from 15 m to the bottom of the sediment column (Table **T10**; Figure **F36**). This pattern is similar to the profiles at Site U1506 but has small variations that could be possibly revealed by higher resolution sampling.

Strontium, boron, silica, and lithium

Dissolved Sr, B, and Si change with depth differently at Site U1507 than at Site U1506 (Table **T10**; Figure **F36**). Sr concentration increases smoothly from 124 µM at 3 m to 1106 µM at 177 m but

remains almost constant between 177 and 248 m. Below that depth, Sr concentration generally increases downhole with fluctuations to a maximum value of 1287 µM, ~15 times as high as the concentration in seawater.

The B concentration profile displays a gradual decrease with depth with fluctuations (Table **T10**; Figure **F36**). Fluctuations in B concentration become larger in amplitude with depth, which also happens in the pH profile.

Silica concentration exhibits an unusual profile. H_4SiO_4 concentration in most samples is between 150 and 180 µM. However, in two intervals, one in the upper 100 m and the other one between 400 and 500 m, H_4SiO_4 concentration reaches as high as 787 µM.

The Li concentration profile at Site U1507 fluctuates smoothly downhole at the 100 m scale, ranging between 4.4 and 32.4 µM. Li decreases from 22.6 µM in the mudline sample to a minimum of 4.4 µM at 167 m, then increases to 7.1 µM at 177 m, and remains almost the same to 233 m. Below, Li concentration decreases to 4.5 µM at 243 m and increases almost linearly to 32.1 µM at 356 m. Li remains at a similar value for the next 50 m and decreases to a low of 14.5 µM between 400 and 500 m. The high Li concentrations at about 400 m may relate to clay-rich sediment, compared with carbonate ooze above.

Bulk sediment geochemistry

A total of 118 freeze-dried bulk sediment samples with a maximum volume of 5 cm³ were collected from Holes U1507A (48 samples) and U1507B (70 samples) at a sampling resolution of at least one sample per core. Typically, samples were taken adjacent to MAD samples to facilitate comparison with physical properties.

In general, changes in total carbon (TC) and total inorganic carbon (TIC) contents correspond well to the defined lithostratigraphic units (see **Lithostratigraphy**). Throughout the sediment column, TC and TIC contents range between 1.8 and 11.8 wt% and between 1.6 and 11.4 wt%, respectively (Table **T11**; Figure **F37**). Such values reflect carbonate ($CaCO_3$) contents between 14 and 95 wt%, assuming that calcium carbonate hosts all inorganic carbon. Because most carbon exists as $CaCO_3$, downhole profiles of TC and $CaCO_3$ closely mimic each other.

The highest $CaCO_3$ contents are recorded in Subunit Ia (86 ± 13 wt%). In this subunit, relative lows were observed around 100, 230, 300, and 390 m. Subunits Ib and Ic are represented by relatively large fluctuations in carbonate contents (14–85 wt%), with the lowest values attained in the middle part of both subunits. These trends in carbonate content correlate well with changes in other measured properties such as reflectance L*, magnetic susceptibility, and NGR (see **Petrophysics**). In these units, some (typically darker) layers with subdominant lithologies were measured and are represented by lower TC (3.4 ± 2.1 wt%) and carbonate (27 ± 17 wt%) contents. Carbonate contents in Unit II are high, varying between 50 and 80

Table T11. Bulk sediment geochemistry, Site U1507. **Download table in CSV format.**

Figure F37. Bulk sediment profiles of $CaCO_3$, TC, TIC, TOC, and total nitrogen (TN), Site U1507.
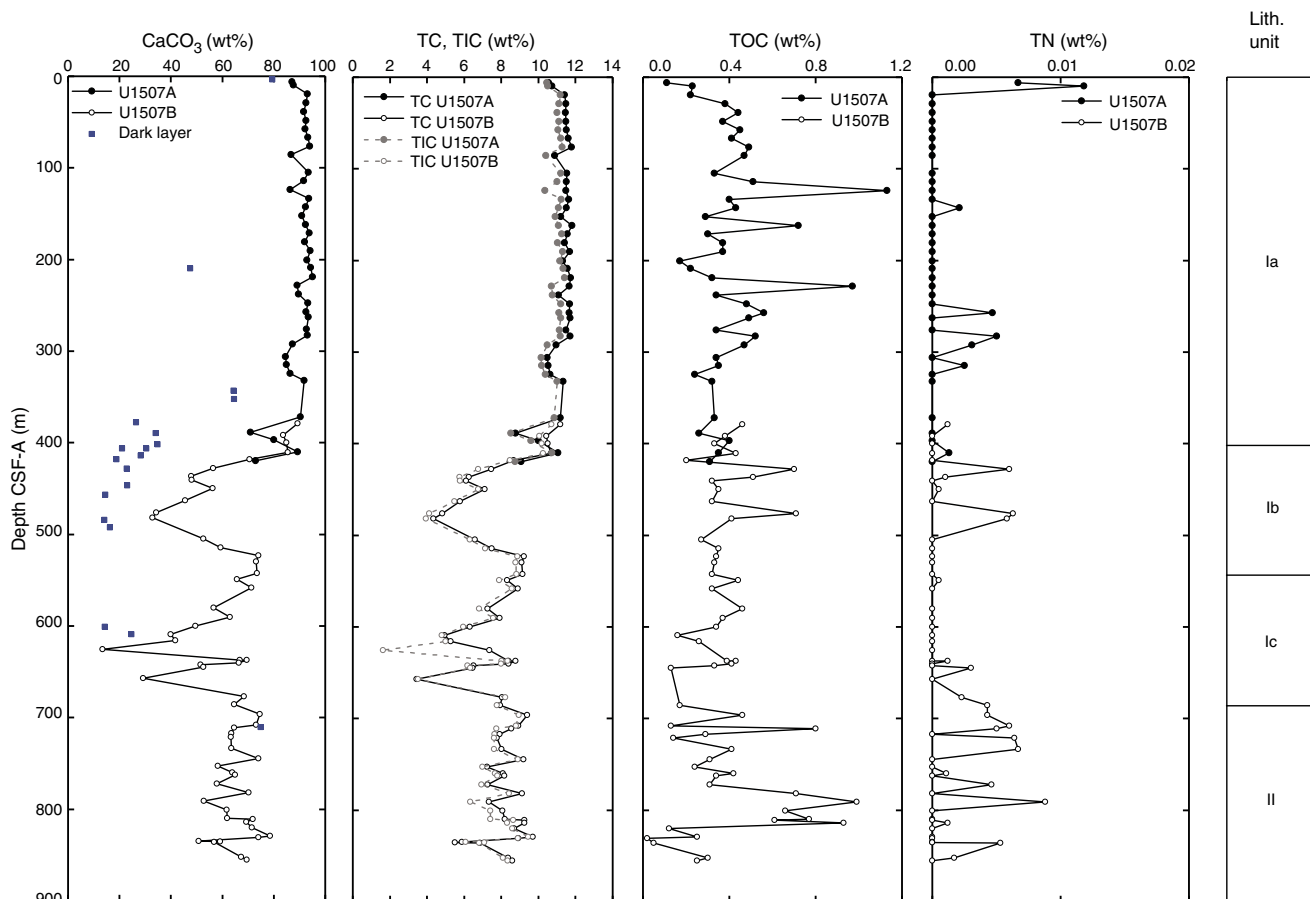
wt%. Total organic carbon (TOC) contents are low (averaging 0.4 wt%) throughout the sediment column and do not differ significantly between units.

Nitrogen contents throughout the sediment column are consistently low, mostly <0.01 wt% (Table **T11**; Figure **F37**).

Discussion

The downhole profiles of SO_4^{2-}, NH_4^+, and pH likely relate to modest organoclastic sulfate reduction (OSR) in the upper ~250 m of sediment. This process is mentioned in **Geochemistry** in the Site U1506 chapter (Sutherland et al., 2019b).

The dissolved Ca, Mg, and K concentration profiles at Site U1507 share similarities with those at Site U1506 (see **Geochemistry** in the Site U1506 chapter [Sutherland et al., 2019b]) and with carbonate-rich sediment sequences from many open-ocean settings (e.g., Gieskes and Lawrence, 1976; Baker, 1986; Delaney et al., 1991; Sun et al., 2016). The coupled change in Ca and Mg has been documented since early DSDP legs and has been explained by reactions of the pore water with volcanic materials in the sediment, dissolution of carbonate, formation of clay minerals such as smectite, or ion exchange (e.g., above references and Gieskes, 1981; Kastner and Gieskes, 1976). Formation of clay minerals may also consume K (e.g., Gieskes and Lawrence, 1981; Sun et al., 2016). The abundant clay in Subunit Ib and volcanic ash in Subunit Ic may be a sink of K, in accordance with the two peaks in the K profile from wireline logging data (Figure **F32**).

Starting at 243 m, several profiles of dissolved species show differences compared with the overlying sequence. Although the switch from APC to XCB coring can explain the less smooth trends of major elements below this depth, the change in coring operations cannot explain the reversal in trends for pH, NH_4^+, and especially Li. Volcanic ash is found at 243 m, but no major change in lithology occurs at this depth.

At DSDP and Ocean Drilling Program sites where data are available, it is commonly reported that pore water Sr concentration increases to a plateau at depth and silica becomes enriched across specific horizons (e.g., Gieskes and Lawrence, 1976; Baker, 1986; Delaney et al., 1991). Carbonate dissolution and recrystallization definitely occur at Site U1507 because the lithology changes from nannofossil ooze to chalk at approximately 295 m (see **Lithostratigraphy**). Because biogenic carbonate typically contains Sr and recrystallized calcite excludes Sr, the downhole increase in dissolved Sr may come from the dissolution of biogenic calcite (e.g., Gieskes, 1981; Baker et al., 1982). Dissolved silica could result from the dissolution of biogenic silica (opal-A) or volcanic ash (e.g., Gieskes, 1981). Radiolarians are found in the upper 50 m and between 420 and 500 m at this site (see **Biostratigraphy and paleoenvironment**). Volcanic ash is also abundant in Subunits Ib and Ic. Therefore, biogenic silica and/or volcanic ash could be sources of dissolved silica at this site. Lower silica concentrations in the middle part of the sequence may reflect uptake by clay minerals (e.g., Gieskes, 1981).

Similar to Site U1506, high carbonate percentages in the major lithologies reflect a large contribution of calcareous nannofossil and, secondarily, foraminiferal components to the sediment. This situation is similar to that of the present day, in which New Caledonia Trough surface sediment is dominantly nannofossil ooze (see **Background and objectives**). Low organic carbon contents of <1 wt% (and absence of nitrogen) conform to an oligotrophic open-ocean setting (Hedges and Keil, 1995). The slightly higher TOC% at Site U1507 (0.4% for the upper 240 m) compared with that at Site

U1506 (0.3% for the upper 210 m) may drive stronger OSR at Site U1507 and explain the lower dissolved SO_4^{2-} and higher dissolved NH_4^+ concentrations.

Changes in carbonate content correspond to lithostratigraphic units. Decreasing carbonate contents and reflectance L* toward the middle of Subunits Ib and Ic, together with increasing NGR, likely indicate increased amounts of terrigenous or volcanic aluminosilicate. The varying carbonate contents in Unit II could reflect cyclical processes. For example, the MECO interval (three samples) may have low-range carbonate contents of 50–59 wt% (centered at ~835 m), corresponding to an increase in NGR. Deep-sea carbonate dissolution during the MECO is well recorded at a global suite of sites (Bohaty et al., 2009) and could be assessed at Site U1507 through a higher resolution study, although recovery of the MECO interval is not optimal.

Stratigraphic correlation

Paleomagnetic inclination, magnetic susceptibility, NGR, and GRA data were loaded into the Correlator software (version 2.1) to establish a depth correlation between the overlapping depths in Holes U1507A and U1507B. A single tie was established based on a prominent feature in the NGR records that occurs in the interval between Samples 371-U1507A-46X-2, 100 cm, and 371-U1507B-6R-2, 140 cm (Figure **F38**). This tie is further supported by robust

Figure F38. Depth correlation between overlapping intervals of Holes U1507A and U1507B based on NGR (blue) records and confirmed with magnetic inclination (black) and core images. The overlapping interval was XCB cored in Hole U1507A and RCB cored in Hole U1507B.
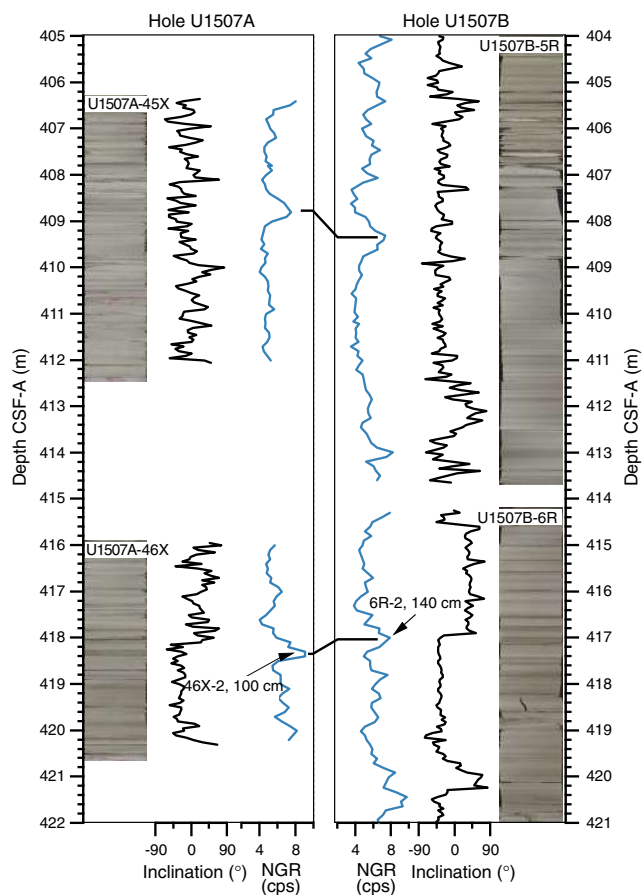
correlation of variations in paleomagnetic inclination, light reflectance data (L*, a*, and b*), and core images. Given the limited overlap of cores between the holes, no core composite depth scale was established. It should be noted that according to core descriptions, this interval is affected by slumping, which may explain the observed discrepancies in calcareous nannofossil datums between Holes U1507A and U1507B. Interestingly, the overlapping interval cored with the XCB system (Hole U1507A) is significantly less complete than the one cored with the RCB system (Hole U1507B).

All cores from Holes U1507A and U1507B were tied to downhole logging data by matching NGR measured on cores and in the borehole. This permitted the translation of core depth scales from core depth below seafloor (CSF-A) to WMSF (Table **T12**) so that lithologic boundaries could be mapped to logging data (Figure **F39**). Alignment of magnetic susceptibility measured on cores and determined by logging (Figure **F40**) supports the established correlation between core depth and logging depth. The amount of offset required to map core data to logging data was minimal (0.0 to −2.7 m for all cores), which indicates a close match between the CSF-A and WMSF depth scales.

Table T12. Offsets applied to cores based on correlation to wireline logs using NGR data, Site U1507. **Download table in CSV format.**

Figure F39. Depth correlation between Hole U1507B core data and wireline data based on NGR records. A. Subunit Ia/Ib boundary. B. Subunit Ib/Ic boundary. C. Subunit Ic/Unit II boundary. Green = whole-round core NGR data on CSF-A scale, blue = shifted NGR core data on WMSF scale, red = wireline logging NGR data.
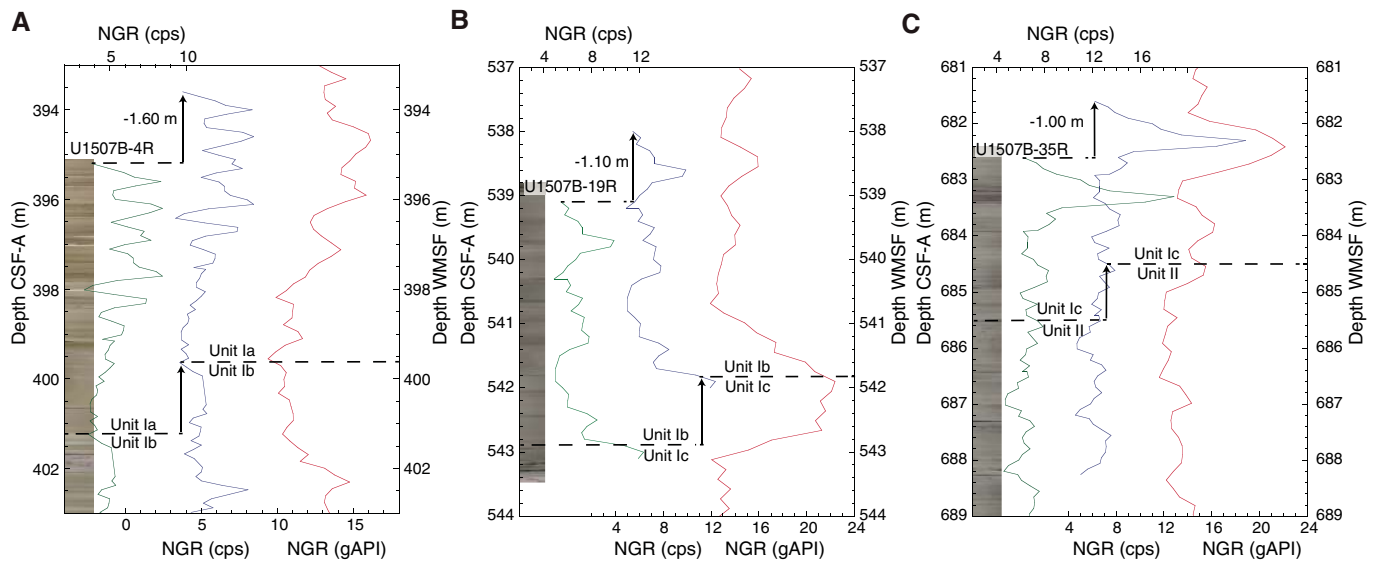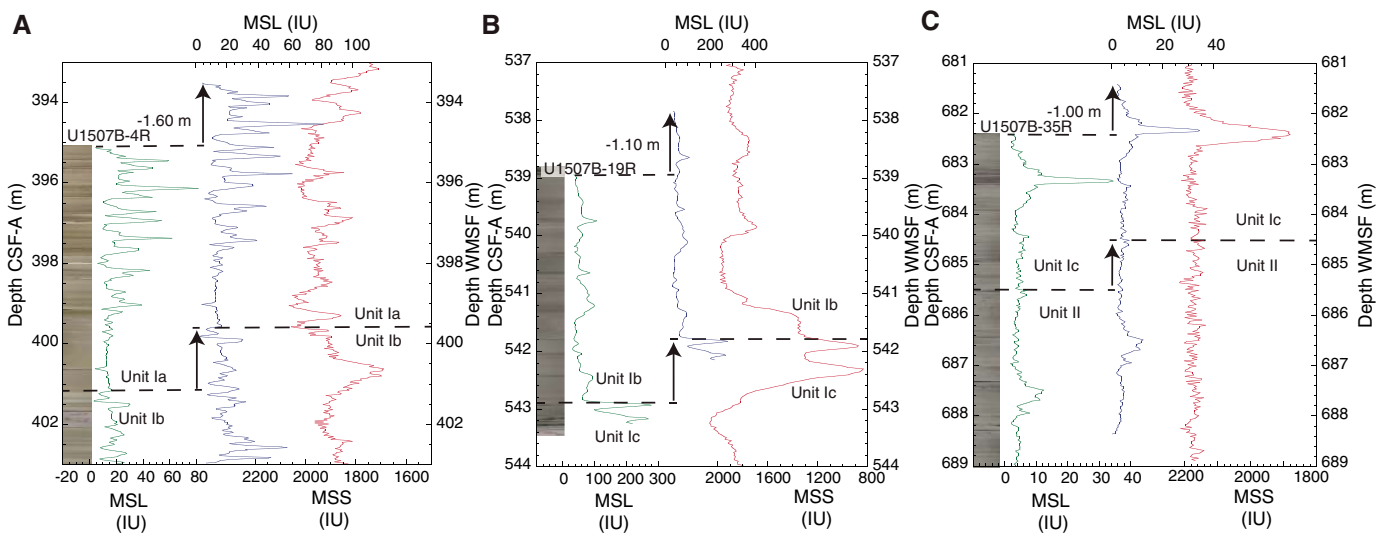

Figure F40. Depth correlation between Hole U1507B core data and wireline data based on MS records. A. Subunit Ia/Ib boundary. B. Subunit Ib/Ic boundary. C. Subunit Ic/Unit II boundary. Green = MSL core data on CSF-A scale, blue = shifted MSL core data on WMSF scale, red = wireline logging MSS data.

Age model and sedimentation rates

At Site U1507, a 855 m thick sequence of Pleistocene to middle Eocene biogenic ooze and chalk interbedded with calcareous and volcaniclastic turbidites and clayey nannofossil chalk was recovered. Calcareous nannofossils are present throughout lithostratigraphic Units I and II, and polarity chron boundaries were identified for intervals of Subunits Ib and Ic and Unit II. Using paleomagnetic and biostratigraphic datums, linear sedimentation rates (LSRs) and mass accumulation rates (MARs) were calculated for Site U1507 on the CSF-A depth scale (Table **T3**; Figure **F41**; see **Biostratigraphy and paleoenvironment** and **Paleomagnetism**). LSRs have not been corrected for increasing compaction of sediment with depth, elastic rebound at atmospheric pressure levels, or coring disturbance. Sedimentation rates for the 0–41 Ma interval were calculated preferentially using magnetostratigraphic datums,

when present; otherwise, calcareous nannofossil events were utilized.

The sedimentary record recovered at Site U1507 is remarkably continuous despite the numerous turbidite deposits and seismic observations showing prominent reflectors. The entirety of the Oligocene is present, albeit with low-recovery intervals, which is surprising given previous work in the area. LSRs from the mid- to late Eocene to the latest Eocene vary between ~30 and 60 m/My and decrease at the Eocene–Oligocene transition to ~15–20 m/My. Through the entire Oligocene, LSRs average 15 m/My, interrupted by two intervals with more enhanced LSR. These intervals span from 30 to 29 Ma with LSRs between 40 and 60 m/My and from 25 to 23 Ma with LSRs between 20 and 40 m/My. At the Oligocene/Miocene boundary, LSR drops from 26 to 12 m/My, and it stays relatively constant until 13.8 Ma. At 13.8 Ma, LSR drops to 4 m/My, remaining at lower values until 10.6 Ma, when LSR increases

Figure F41. Sedimentation accumulation over time, Site U1507. A. Core recovery. B. Shipboard biostratigraphic and magnetostratigraphic datums and interpreted age-depth model. C. LSR and total MAR. Horizontal line = lithostratigraphic unit boundary, dashed horizontal lines = subunit boundaries.
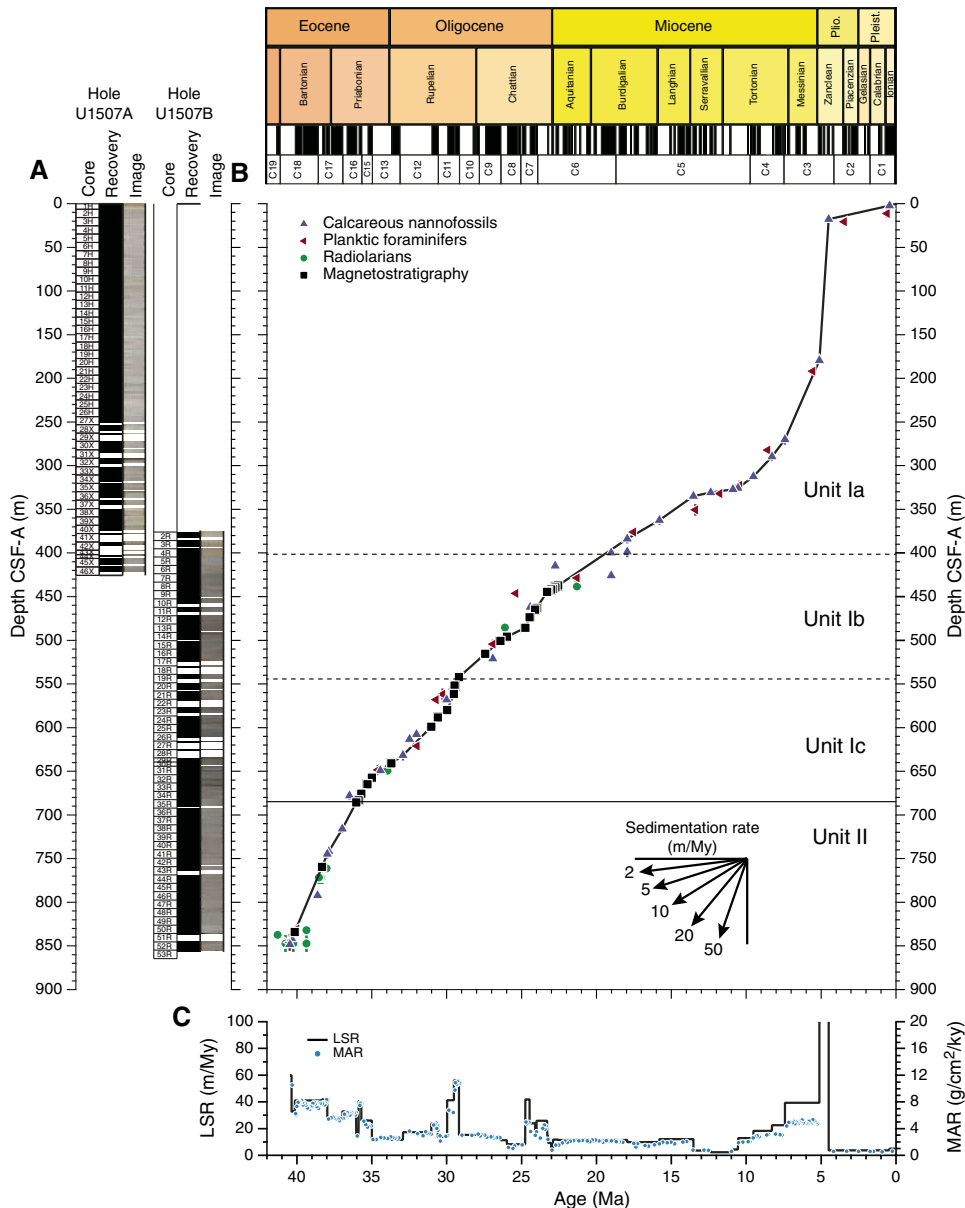
to 13 m/My. During the late Miocene, LSR increases stepwise to 18 m/My at 9.5 Ma, to 23 m/My at 8.3 Ma, and to almost 40 m/My at 7.4 Ma. MARs closely mimic those observed for LSRs.

Interestingly, LSR appears to be lowest across intervals in which numerous turbidite deposits were observed, implying that the turbidites removed significant amounts of sediment originally deposited. Elevated LSRs for the latest Miocene to early Pliocene interval were also observed at Site U1506 and at DSDP Leg 90 sites (Kennett and von der Borch, 1986), and they correspond to the "biogenic bloom" event (Dickens and Owen, 1999). Exceptionally high LSRs (>120 m/My) from 5.1 to 4.5 Ma in the early Pliocene correspond to thick debris flows, a prominent feature observed in seismic data. The uppermost interval of Site U1507 is condensed (LSR < 4 m/My).

References

Abdul Aziz, H., Di Stefano, A., Foresi, L.M., Hilgen, F.J., Iaccarino, S.M., Kuiper, K.F., Lirer, F., Salvatorini, G., and Turco, E., 2008. Integrated stratigraphy and ⁴⁰Ar/³⁹Ar chronology of early Middle Miocene sediments from DSDP Leg 42A, Site 372 (Western Mediterranean). *Palaeogeography, Palaeoclimatology, Palaeoecology,* 257(1–2):123–138. **https://doi.org/10.1016/j.palaeo.2007.09.013**

Agnini, C., Fornaciari, E., Raffi, I., Catanzariti., R., Pälike, H., Backman, J., and Rio, D., 2014. Biozonation and biochronology of Paleogene calcareous nannofossils from low and middle latitudes. *Newsletters on Stratigraphy,* 47(2):131–181. **https://doi.org/10.1127/0078-0421/2014/0042**

Backman, J., Raffi, I., Rio, D., Fornaciari, E., and Pälike, H., 2012. Biozonation and biochronology of Miocene through Pleistocene calcareous nannofossils from low and middle latitudes. *Newsletters on Stratigraphy,* 45(3):221–244. **https://doi.org/10.1127/0078-0421/2012/0022**

Baker, P.A., 1986. Pore-water chemistry of carbonate-rich sediments, Lord Howe Rise, Southwest Pacific Ocean. *In* Kennett, J.P., von der Borch, C.C., et al., *Initial Reports of the Deep Sea Drilling Project,* 90: Washington, DC (U.S. Government Printing Office), 1249–1256. **https://doi.org/10.2973/dsdp.proc.90.132.1986**

Baker, P.A., Gieskes, J.M., and Elderfield, H., 1982. Diagenesis of carbonates in deep-sea sediments: evidence from Sr/Ca ratios and interstitial dissolved Sr²⁺ data. *Journal of Sedimentary Research,* 52(1):71–82. **https://doi.org/10.1306/212F7EE1-2B24-11D7-8648000102C1865D**

Baur, J., Sutherland, R., and Stern, T., 2014. Anomalous passive subsidence of deep-water sedimentary basins: a prearc basin example, southern New Caledonia Trough and Taranaki Basin, New Zealand. *Basin Research,* 26(2):242–268. **https://doi.org/10.1111/bre.12030**

Bohaty, S.M., Zachos, J.C., Florindo, F., and Delaney, M.L., 2009. Coupled greenhouse warming and deep-sea acidification in the middle Eocene. *Paleoceanography,* 24(2):PA2207. **https://doi.org/10.1029/2008PA001676**

Bolliger, R., Hanselmann, K.W., and Bachofen, R., 1991. Microbial potential in deep-sea sediments. *Experientia,* 47(6):517–523. **https://doi.org/10.1007/BF01949870**

Burns, R.E., and Andrews, J.E., 1973. Regional aspects of deep sea drilling in the southwest Pacific. *In* Burns, R.E., Andrews, J.E., et al., *Initial Reports of the Deep Sea Drilling Project,* 21: Washington, DC (U.S. Govt. Printing Office), 897–906. **https://doi.org/10.2973/dsdp.proc.21.128.1973**

Collot, J., Geli, L., Lafoy, Y., Vially, R., Cluzel, D., Klingelhoefer, F., and Nouzé, H., 2008. Tectonic history of northern New Caledonia Basin from deep offshore seismic reflection: relation to late Eocene obduction in New Caledonia, southwest Pacific. *Tectonics,* 27(6):TC6006. **https://doi.org/10.1029/2008TC002263**

Collot, J., Herzer, R., Lafoy, Y., and Géli, L., 2009. Mesozoic history of the Fairway-Aotea Basin: implications for the early stages of Gondwana fragmentation. *Geochemistry, Geophysics, Geosystems,* 10(12):Q12019. **https://doi.org/10.1029/2009GC002612**

Crook, K.A.W., and Belbin, L., 1978. The southwest Pacific area during the last 90 million years. *Journal of the Geological Society of Australia,* 25(1–2)23–40. **https://doi.org/10.1080/00167617808729012**

Debenay, J.-P., 2012. *A Guide to 1,000 Foraminifera from Southwestern Pacific, New Caledonia:* Paris (Publications Scientifiques du Muséum national d'Histoire naturelle). **http://horizon.documentation.ird.fr/exl-doc/pleins_textes/divers14-01/010058351.pdf**

Delaney, M.L., and Shipboard Scientific Party, 1991. Inorganic geochemistry summary. *In* Kroenke, L.W., Berger, W.H., Janecek, T.R., et al., *Proceedings of the Ocean Drilling Program, Initial Reports,* 130: College Station, TX (Ocean Drilling Program), 549–551. **https://doi.org/10.2973/odp.proc.ir.130.112.1991**

Dickens, G.R., and Owen, R.M., 1999. The latest Miocene–early Pliocene biogenic bloom: a revised Indian Ocean perspective. *Marine Geology,* 161(1):75–91. **https://doi.org/10.1016/S0025-3227(99)00057-2**

Dwyer, G.S., Cronin, T.M., Baker, P.A., Raymo, M.E., Buzas, J.S., and Corrège, T., 1995. North Atlantic deepwater temperature change during late Pliocene and late Quaternary climatic cycles. *Science,* 270(5240):1347–1351. **https://doi.org/10.1126/science.270.5240.1347**

Eade, J.V., 1988. The Norfolk Ridge system and its margins. *In* Nairn, A.E.M., Stehli, F.G., and Uyeda, S. (Eds.), *The Ocean Basins and Margins* (Volume 7B): *The Pacific Ocean:* New York (Plenum Press), 803–824. **https://doi.org/10.1007/978-1-4615-8041-6_7**

Edgar, K.M., Bohaty, S.M., Gibbs, S.J., Sexton, P.F., Norris, R.D., and Wilson, P.A., 2013. Symbiont "bleaching" in planktic foraminifera during the Middle Eocene Climatic Optimum. *Geology,* 41(1):15–18. **http://dx.doi.org/10.1130/G33388.1**

Gieskes, J.M., 1981. Deep-sea drilling interstitial water studies: implications for chemical alteration of the oceanic crust, Layers I and II. *In* Warme, J.E., Douglas, R.G., and Winterer, E.L. (Eds.), *The Deep Sea Drilling Project: A Decade of Progress.* Special Publication - Society of Economic Paleontologists and Mineralogists, 32:149–167. **http://archives.datapages.com/data/sepm_sp/SP32/Deep_Sea_-Drilling_Interstitial_Water_Studies.html**

Gieskes, J.M., and Lawrence, J.R., 1976. Interstitial water studies, Leg 35. *In* Hollister, C.D., Craddock, C., et al., *Initial Reports of the Deep Sea Drilling Project,* 35, Washington, DC (U.S. Government Printing Office), 407–423. **https://doi.org/10.2973/dsdp.proc.35.121.1976**

Gieskes, J.M., and Lawrence, J.R., 1981. Alteration of volcanic matter in deep-sea sediments: evidence from the chemical composition of interstitial waters from deep sea drilling cores. *Geochimica Cosmochimica Acta,* 45(10):1687–1703. **https://doi.org/10.1016/0016-7037(81)90004-1**

Hayward, B.W., Grenfell, H.R., Sabaa, A.T., Neil, H.L., and Buzas, M.A., 2010. Recent New Zealand deep-water benthic foraminifera: taxonomy, ecologic distribution, biogeography, and use in paleoenvironmental assessment. *GNS Sciences Monograph,* 26:1–363.

Hedges, J.I., and Keil, R.G., 1995. Sedimentary organic matter preservation: an assessment and speculative synthesis. *Marine Chemistry,* 49(2–3):81–115. **https://doi.org/10.1016/0304-4203(95)00008-F**

Herzer, R.H., Barker, D.H.N., Roest, W.R., and Mortimer, N., 2011. Oligocene–Miocene spreading history of the northern South Fiji Basin and implications for the evolution of the New Zealand plate boundary. *Geochemistry, Geophysics, Geosystems,* 12(2):Q02004. **https://doi.org/10.1029/2010GC003291**

Jorissen, F.J., Fontanier, C., and Thomas, E., 2007. Paleoceanographical proxies based on deep-sea benthic foraminiferal assemblage characteristics. *In* Hillaire-Marcel, C., and De Vernal, A. (Eds.), *Developments in Marine Geology* (Volume 1): *Proxies in Late Cenozoic Paleoceanography:* Amsterdam (Elsevier), 263–325. **http://dx.doi.org/10.1016/S1572-5480(07)01012-3**

Kaminski, M.A., and Gradstein, F.M., 2005. Atlas of Paleogene cosmopolitan deep-water agglutinated foraminifera. *Grzybowski Foundation Special Publication,* 10. **http://www.foraminifera.eu/atlas.html**

Kastner, M., and Gieskes, J.M., 1976. Interstitial water profiles and sites of diagenetic reactions, Leg 35, DSDP, Bellingshausen Abyssal Plain. *Earth and Planetary Science Letters,* 33(1):11–20. **https://doi.org/10.1016/0012-821X(76)90152-7**

Kennett, J.P., and von der Borch, C.C., 1986. Southwest Pacific Cenozoic pale-oceanography. *In* Kennett, J.P., von der Borch, C.C., et al., *Initial Reports of the Deep Sea Drilling Project*, 90: Washington, DC (U.S. Government Printing Office), 1493–1517. **https://doi.org/10.2973/dsdp.proc.90.148.1986**

King, P.R., and Thrasher, G.P., 1996. Cretaceous–Cenozoic geology and petroleum systems of the Taranaki Basin, New Zealand. *Institute of Geological & Nuclear Sciences Monograph*, 2.

Kirschvink, J.L., 1980. The least-squares line and plane and the analysis of palaeomagnetic data. *Geophysical Journal of the Royal Astronomical Society*, 62(3):699–718. **https://doi.org/10.1111/j.1365-246X.1980.tb02601.x**

Lafoy, Y., Brodien, I., Vially, R., and Exon, N.F., 2005. Structure of the basin and ridge system west of New Caledonia (southwest Pacific): a synthesis. *Marine Geophysical Research*, 26(1):37–50. **https://doi.org/10.1007/s11001-005-5184-5**

Matthews, K.J., Williams, S.E., Whittaker, J.M., Müller, R.D., Seton, M., and Clarke, G.L., 2015. Geologic and kinematic constraints on Late Cretaceous to mid Eocene plate boundaries in the southwest Pacific. *Earth-Science Reviews*, 140:72–107. **https://doi.org/10.1016/j.earscirev.2014.10.008**

Mortimer, N., Gans, P.B., Meffre, S., Martin, C.E., Seton, M., Williams, S., Turnbull, R.E., et al., 2018. Regional volcanism of northern Zealandia: post-Gondwana break-up magmatism on an extended, submerged continent. *In* Sensarma, S., and Storey, B.C. (Eds.), *Large Igneous Provinces from Gondwana and Adjacent Regions*. Geological Society Special Publication, 463(1):199–226. **https://doi.org/10.1144/SP463.9**

Okada, H., and Bukry, D., 1980. Supplementary modification and introduction of code numbers to the low-latitude coccolith biostratigraphic zonation (Bukry, 1973; 1975). *Marine Micropaleontology*, 5:321–325. **https://doi.org/10.1016/0377-8398(80)90016-X**

Pollack, H.N., Hurter, S.J., and Johnson, J.R., 1993. Heat flow from the Earth's interior: analysis of the global data set. *Reviews of Geophysics*, 31(3):267–280. **http://dx.doi.org/10.1029/93RG01249**

Schellart, W.P., Lister, G.S., and Toy, V.G., 2006. A Late Cretaceous and Cenozoic reconstruction of the Southwest Pacific region: tectonics controlled by subduction and slab rollback processes. *Earth-Science Reviews*, 76(3–4):191–233. **https://doi.org/10.1016/j.earscirev.2006.01.002**

Shipboard Scientific Party, 1973. Site 206. With contributions by D. Burns and P.N. Webb. *In* Burns, R.E., Andrews, J.E., et al., *Initial Reports of the Deep Sea Drilling Project*, 21: Washington, DC (U.S. Government Printing Office), 103–195. **https://doi.org/10.2973/dsdp.proc.21.106.1973**

Sun, X., Higgins, J., and Turchyn, A.V., 2016. Diffusive cation fluxes in deep-sea sediments and insight into the global geochemical cycles of calcium, magnesium, sodium and potassium. *Marine Geology*, 373:64–77. **https://doi.org/10.1016/j.margeo.2015.12.011**

Sutherland, R., Collot, J., Lafoy, Y., Logan, G.A., Hackney, R., Stagpoole, V., Uruski, C., et al., 2010. Lithosphere delamination with foundering of lower crust and mantle caused permanent subsidence of New Caledonia Trough and transient uplift of Lord Howe Rise during Eocene and Oligocene initiation of Tonga-Kermadec subduction, western Pacific. *Tectonics*, 29(2). **https://doi.org/10.1029/2009TC002476**

Sutherland, R., Dickens, G.R., Blum, P., Agnini, C., Alegret, L., Asatryan, G., Bhattacharya, J., Bordenave, A., Chang, L., Collot, J., Cramwinckel, M.J., Dallanave, E., Drake, M.K., Etienne, S.J.G., Giorgioni, M., Gurnis, M., Harper, D.T., Huang, H.-H.M., Keller, A.L., Lam, A.R., Li, H., Matsui, H., Morgans, H.E.G., Newsam, C., Park, Y.-H., Pascher, K.M., Pekar, S.F., Penman, D.E., Saito, S., Stratford, W.R., Westerhold, T., and Zhou, X., 2019a. Expedition 371 methods. *In* Sutherland, R., Dickens, G.R., Blum, P., and the Expedition 371 Scientists, *Tasman Frontier Subduction Initiation and Paleogene Climate*. Proceedings of the International Ocean Discovery Program, 371: College Station, TX (International Ocean Discovery Program). **https://doi.org/10.14379/iodp.proc.371.102.2019**

Sutherland, R., Dickens, G.R., Blum, P., Agnini, C., Alegret, L., Asatryan, G., Bhattacharya, J., Bordenave, A., Chang, L., Collot, J., Cramwinckel, M.J., Dallanave, E., Drake, M.K., Etienne, S.J.G., Giorgioni, M., Gurnis, M., Harper, D.T., Huang, H.-H.M., Keller, A.L., Lam, A.R., Li, H., Matsui, H., Morgans, H.E.G., Newsam, C., Park, Y.-H., Pascher, K.M., Pekar, S.F., Penman, D.E., Saito, S., Stratford, W.R., Westerhold, T., and Zhou, X., 2019b. Site U1506. *In* Sutherland, R., Dickens, G.R., Blum, P., and the Expedition 371 Scientists, *Tasman Frontier Subduction Initiation and Paleogene Climate*. Proceedings of the International Ocean Discovery Program, 371: College Station, TX (International Ocean Discovery Program). **https://doi.org/10.14379/iodp.proc.371.103.2019**

Tjalsma, R.C., and Lohmann, G.P., 1983. Paleocene–Eocene bathyal and abyssal benthic foraminifera from the Atlantic Ocean. *Micropaleontology, Special Publication*, 4.

Urmos, J., and Wilkens, R.H., 1993. In situ velocities for pelagic carbonates: new insights from Ocean Drilling Program Leg 130, Ontong Java Plateau. *Journal of Geophysical Research: Solid Earth*, 98(B5):7903–7920. **https://doi.org/10.1029/93JB00013**

Uruski, C., Baillie, P., and Stagpoole, V., 2003. Development of the Taranaki Basin and comparisons with the Gippsland Basin: implications for deep-water exploration. *APPEA Journal*, 43(1):185–196. **https://doi.org/10.1071/AJ02009**

Uruski, C., and Wood, R., 1991. A new look at the New Caledonia Basin, an extension of the Taranaki Basin, offshore North Island, New Zealand. *Marine and Petroleum Geology*, 8(4):379–391. **https://doi.org/10.1016/0264-8172(91)90061-5**

van Morkhoven, F.P.C.M., Berggren, W.A., Edwards, A.S., and Oertli, H.J., 1986. Cenozoic cosmopolitan deep-water benthic foraminifera. *Bulletin des centres de recherches Exploration-production Elf-Aquitaine: Mémoire*, 11.

Wood, R.A., 1993. The Challenger Plateau. *In* Ballance, P.F. (Ed.), *Sedimentary Basins of the World* (Volume 2): *South Pacific Sedimentary Basins*: Amsterdam, (Elsevier), 351–364.

Zijderveld, J.D.A., 1967. AC demagnetization of rocks: analysis of results. *In* Collinson, D.W., Creer, K.M., and Runcorn, S.K. (Eds.), *Developments in Solid Earth Geophysics* (Volume 3): *Methods in Palaeomagnetism*: Amsterdam (Elsevier), 254–286. **https://doi.org/10.1016/B978-1-4832-2894-5.50049-5**